Modelling the Evaporation of an Oscillating Droplet

A dissertation submitted towards the degree
Doctor of Engineering (Dr.-Ing.)
of the Department of Engineering and Applied Sciences
of University of Bergamo
by

Hu Yueqiao

Bergamo, 2025

Acknowledgments

This thesis presents the results of my research conducted at the University of Bergamo, within the framework of the International Research Training Group (IRTG) Droplet Interaction Technologies (DROPIT) GRK 2160/2, funded by the German Research Foundation (DFG).

I sincerely thank Prof. Gianpietro Elvio Cossali, Prof. Simona Tonini, and Prof. Bernhard Weigand for this opportunity to be involved in this inspiring project. Prof. Cossali and Prof. Tonini show invaluable guidance, continuous support, and great patience throughout my research. From them, I have learned not only the scientific knowledge and research skills, but also the method and attitude to the research. The free and very pleasant work atmosphere they created is also greatly appreciated.

I am also very grateful to Prof. Weigand for introducing me to this exciting and interesting research topic, for his helpful suggestions on the paper drafts, and for the great collaboration with the Institute of Aerospace Thermodynamics (ITLR) at the University of Stuttgart.

I would also like to thank Prof. Bernhard Weigand and Prof. Grünter Brenn for being co-referees of this thesis.

Finally, I would like to thank my parents for their unwavering support and encouragement throughout my life.

"Without accumulating small steps, one cannot reach a thousand miles;
without gathering small streams, one cannot form rivers and seas."
−Xunzi

Table of Contents

Chapter 1. Introduction 1

  1.1 Objective and Motivations 1

  1.2 Outline 2

Chapter 2. Methodology and State of the Art 3

  2.1 Methodology 3

  2.2 State of the Art in Droplet Oscillation 3

  2.3 State of the Art in Droplet Evaporation 8

Chapter 3. Governing Equations and Mathematical Framework 15

  3.1 Physical Configuration 15

  3.2 Conservation Equations 16

    3.2.1 Mass and Species Conservation 17

    3.2.2 Momentum Conservation 18

    3.2.3 Energy Conservation 19

  3.3 Jump Conditions, Evaporation Flux and Evaporation Rate 19

    3.3.1 Jump Conditions 20

    3.3.2 Evaporation Flux and Evaporation Rate 22

  3.4 Non-dimensionalization and Dimensionless Groups 23

  3.5 Potential Flow and Laplace's Equation 24

  3.6 Prolate/Spherical/Oblate Coordinate System and Generalized Spheroidal Coordinate System 25

    3.6.1 Prolate Coordinate System 26

    3.6.2 Spherical Coordinate System 27

    3.6.3 Oblate Coordinate System 27

    3.6.4 Generalized Spheroidal Coordinate System 28

  3.7 Normal Mode Analysis of Droplet Oscillation 31

  3.8 Modelling Hierarchy and Scope 34

  3.9 Numerical Tools 35

Chapter 4. Droplet Oscillation 39

4.1 Analytical Model for an Oscillating Droplet under the Assumption of a potential flow . . . 39
4.1.1 Analytical Solutions of the Velocity Fields in both Phases . . . 40
4.1.2 Energy Balance and Deformation Parameter . . . 45
4.2 Direct Numerical Simulation of Droplet Oscillation using FS3D . . . 47
4.2.1 Computational Settings and Grid Resolution Convergency Study . . . 47
4.2.2 Results from FS3D Simulations and Discussions . . . 48

Chapter 5. Evaporation Characteristics of an Oscillating Droplet . . . 55
5.1 An Analytical/Numerical Model for the Evaporation of an Oscillating Spheroidal Droplet . . . 57
5.1.1 Analytical Model . . . 58
5.1.2 Implementation of the Solution . . . 62
5.1.3 Results From Analytical/Numerical Model and Discussions . . . 64
5.2 Direct Numerical Simulation of the Evaporation of an Oscillating Droplet using FS3D . . . 79
5.2.1 Code Validations . . . 79
5.2.2 Computational Settings and Grid Resolution Convergence Study . . . 82
5.2.3 Results from FS3D Simulations and Discussions . . . 83

Chapter 6. Conclusions and Outlook . . . 89

Appendices . . . 93
Appendix A. . . . 95
A.1 Harmonic Solutions of the Laplace Equation in a Spherical Coordinate System . 95
A.2 Legendre’s Equation and Associated Legendre’s Equation . . . 96
A.3 The Scale Factors of a Generalized Spheroidal Coordinate System . . . 99
A.4 The Surface Area of a Spheroid in a Generalized Spheroidal Coordinate System 101
A.5 The Normal Interface Velocity in a Generalized Spheroidal System . . . 101
A.6 Gas Velocity for an Oscillating Droplet in Potential Flows . . . 102
A.7 The Coordinate Transformation Matrix . . . 103
A.8 Evaporation Flux and Evaporation Rate under Quasi-steady Assumptions . . . 104
A.9 The Apparent Velocity . . . 105

References . . . 107

Chapter 1. Introduction

1.1 Objective and Motivations

In many engineering process [1], such as fuel atomization in aeroengines and spray-based fire suppression system, liquid droplets undergo evaporation while experiencing hydrodynamic deformation. Under such conditions, the liquid-gas interface is rarely perfectly stationary, but evolves in time. Its time scales may be comparable to those of mass transfer. The associated diffusion process in the surrounding gas therefore becomes time-dependent.

The evaporation of a single-component droplet in the gas phase is a classical problem in fluid dynamics and transport phenomena and has been studied over several decades [2–4]. Classical models focus on diffusion-controlled transport in the gas phase and often reply on quasi-steady approximations for mass fraction field in the gas phase. In many diffusion-controlled regimes for a single-component droplet, the dominant resistance to mass transfer is located in the surrounding gas, while internal liquid transport mainly affects temperature and velocity redistributions inside the droplet. Independently, droplet shape oscillations have been investigated since the pioneering work of Rayleigh [5–7]. The frequencies and viscous damping characteristics of small-amplitude oscillations are well established. These studies primarily address hydrodynamic behaviours and usually do not consider mass transfer. Although both droplet evaporation and oscillation have been studied extensively, they have largely developed as separate research topics. In evaporation models, the droplet is commenly assumed to remain a fixed shape or slowly varying. In oscillation studies, the droplet is usually considered non-evaporating. However, when droplet evaporation and oscillation occur simultaneously, the diffusion process in the gas phase becomes time-dependent due to the moving interface. Even if the overall evaporation process remains diffusion-controlled, the transient vapour concentration field in the gas phase must adapt to the evolving droplet geometry. The present thesis address this problem by direct numerical simulations (DNS) and an analytical/numerical model, which analyses transient vapour distribution in a deforming domain, where the interface motion is prescribed by an oscillation model. How does a time-dependent interface influence the instantaneous evaporation flux and its temporal evolution? It is the focus of the present thesis. In this framework, the present thesis employs two complementary approaches. First, analytical oscillation model based on potential-flow theory is used to prescribe the interface motion. The associated evaporation problem is formulated as a transient convection-diffusion equation in the surrounding gas with a deforming domain, by using a generalized spheroidal coordinate system. The interface motion is not altered by the evaporation process. In addition, direct numerical simulations using the code free surface 3D (FS3D) are performed to investigate the evaporation of oscillating droplets without reduced-order assumptions. These simulations provide a reference configuration for examing the behaviour observed in analytical/numerical model.

1.2 Outline

First, Chapter 2 reviews the state of the art. Chapter 3 introduces the theoretical fundamentals, which may be relevant to the previous and present work. Next, we summarize our work in droplet oscillation in Chapter 4 and work in droplet evaporation in Chapter 5. Before introducing the evaporation model for an oscillating droplet, an analytical oscillating model is first introduced in Chapter 4. Then, combined with the droplet evaporation, the effect of a moving interface on the droplet evaporation characteristics is summarized and discussed. Finally, we conclude our work in Chapter 6.

Chapter 2. Methodology and State of the Art

2.1 Methodology

Researchers have investigated droplet oscillation and evaporation using experimental, numerical and theoretical approaches. Experimental studies provide valuable information on droplet shape evolution and surrounding flow fields, and are often used to validate numerical and analytical models.

Experimental techniques such as Particle Image Velocimetry (PIV) and Particle Tracking Velocimetry (PTV) are widely used to measure velocity fields in multiphase flows. High-speed imaging is commonly employed to capture the deformation and oscillation of droplets. However, due to the small spatial and temporal scales involved, detailed measurements of internal flow structures and transient interfacial motion remain challenging.

Therefore, numerical simulations are widely used to investigate droplet dynamics. Depending on the modelling level, approaches such as Reynolds-Averaged Navier–Stokes (RANS), Large Eddy Simulation (LES), and Direct Numerical Simulation (DNS) can be applied. These numerical methods provide detailed flow information that is difficult to obtain experimentally.

Analytical modelling complements experimental and numerical approaches by providing physical insight into the dominant mechanisms governing droplet dynamics. Under appropriate assumptions, simplified models may yield analytical or reduced-order descriptions of droplet oscillation and evaporation processes.

In the present work, droplet dynamics are mainly investigated using analytical modelling, while numerical simulations are used to provide additional insight into the flow and evaporation processes.

2.2 State of the Art in Droplet Oscillation

The oscillations of liquid droplets have been studied for more than a century and represent a classical problem in fluid mechanics. Rayleigh [5] first analysed the oscillations of an inviscid liquid droplet in vacuum. By balancing surface tension and inertia, he derived the natural oscillation frequency of a spherical droplet using a normal-mode analysis. Landau and Lifschitz [8] discussed the surface phenomena of a small displacement from the undisturbed surface under gravity or surface tension. The dynamic condition (Laplace's formula), kinetic condition, and Bernoulli equation at the interface are solved. The oscillation frequency of a spherical droplet coincides with the results of Rayleigh [5].

Lamb [9] extended Rayleigh's analysis by including viscous effects. The momentum equation is transformed into the Helmholtz equation, and an analytical solution was then obtained. He showed that the presence of viscosity leads to a decay of the oscillation amplitude and derived expressions for the damping rate of small-amplitude oscillations of viscous droplets. An aperiodic oscillation appears for very high viscosity. For very small viscosity, the oscillation frequency and decay rate of a damped oscillation are derived. Chandrasekhar [10, 11] investigated the decay oscillation of the viscous globe driven by the gravitational force. A threshold value in the form of the Kelvin frequency [6], droplet radius and kinematic viscosity is derived to distinguish the droplet oscillation types. Over this threshold value (low viscosity), it is a damped oscillation; below this threshold value (high viscosity), it is an aperiodic decay. Lamb [9] and Chandrasekhar [10, 11] investigated the effect of viscosity on the small-amplitude oscillations driven by self-gravitation. Reid [12] theoretically studied the oscillation of a viscous droplet under surface tension. The effect of the viscosity on the droplet oscillation was found to be identical to the results by Lamb [9] and Chandrasekhar [10]. It was verified that oscillation dynamics are independent of the forces which drive the droplet into a spherical shape [6]. Based on earlier theoretical developments by Boussinesq and Scriven [13,14], Miller and Scriven [15] investigated the small-amplitude oscillations of a viscous droplet immersed in another viscous fluid. Under the assumption of small interface deformations, the governing equations can be linearized, which allows the oscillation problem to be analysed using normal-mode methods. Their work provides analytical expressions for the oscillation frequency and damping rate as functions of the fluid properties of both phases Based on the work of Bupara [13] and Scriven [14] on the interface, Miller and Scriven [7] investigated the small-amplitude oscillations of a viscous droplet immersed in another viscous fluid. The nonlinear term in the Navier-Stokes equation is ignored since the radial displacement of the interface is assumed to be much smaller than the wavelength along the interface [15] (general dispersion equation). After taking the curl of the momentum equation, the pressure terms disappear in the vorticity equation [11]. The boundary conditions at the interface are replaced by an equivalent set of three scalar equations [13, 14]. The oscillation frequency and damping rate are given numerically for the combination of two fluids of various properties and viscosities: inviscid fluids, a droplet of low and high viscosity in a vacuum, two fluids of low and high viscosity and a gas bubble in a viscous liquid. Prosperetti [16, 17] studied the initial value problem for small amplitude oscillations of a viscous droplet initially deformed in a host liquid. Based on the linearised perturbation theory [18, 19] and by dividing the velocity and pressure field into three parts: pure radial motion, the correction of the potential flow by the perturbation from the undisturbed shape and the correction of the potential flow by the viscosity, the Navier-Stokes equation is solved, subject to the stress conditions and kinematic conditions at the interface. With the Laplace transform, the equation of the interface motion is obtained in an integro-differential form, and the transient oscillation behaviour can be discussed. It was found that the complete transient results are valid to the initial irrotational approximation in the initial stage and asymptotically approach the results by the normal mode technique for a large time [10, 12].

For large amplitude oscillations, the linear assumption holds no longer. Foote [20] simulated viscous droplet oscillation, based on the MAC (Marker-and-Cell) method [21, 22] integrating the finite difference form of the Navier-Stokes equations. The effect of surface tension is considered in a similar way to Daly [23]. The droplet profile is expressed in a parametric formulation [24, 25] to avoid the numerical complication when calculating the infinite interface slope. For small amplitude oscillations, the symmetric oscillations by the numerical predictions are in good agreement with the theoretical predictions. For large-amplitude oscillations, the droplet motion becomes asymmetric and the droplet tends to remain longer in the prolate configuration. The fraction of time spent in the prolate shape increases approximately linearly with the oscillation amplitude, as observed experimentally by Montgomery [26]. The oscillation period increases with the droplet deformation. The evolution of kinetic energy, surface energy and total energy is also calculated. Trinh et al. [27] experimentally studied driven droplet oscillation of small amplitude in immiscible liquids, using acoustic levitation and radiation-pressure-force modulation [28]. The resonance frequency and the damping parameter of the first few modes are measured. The resonance frequency was found to be a function of radius, which is in good agreement with Lamb [6]. The configurations of the oscillation are close to the theoretical predictions. The decay parameter was found to be roughly linear with the droplet viscosity. The time spent in the various configurations depends on the acoustic drive, which is different from that of a free oscillating droplet. A simple internal fluid-particle flow field reveals no internal circulation inside the droplet due to the small amplitude oscillation and droplet size. Using the same technique, Trinh and Wang [29] experimentally studied large amplitude droplet oscillation. It was found that the free decay frequency decreases with increasing oscillation amplitude, and the decay rate is constant for a given initial condition on the oscillation amplitude. The time spent in a prolate configuration is longer as the oscillation amplitude grows larger. Circulation appears first at the droplet boundary and spreads then towards the interior. Tsamopoulos and Brown [30] studied nonlinear axisymmetric oscillations of inviscid droplets by using a Poincaré-Lindstedt expansion technique [31] and a domain perturbation technique [32]. The droplet shape, the velocity potential, and oscillation frequency are corrected by the expansions of small perturbations of different orders, and then the corrections of the droplet shape and velocity potential in each order are represented as Legendre polynomials. The droplet shape and oscillation frequency with the corrections in the first two orders are presented for oscillation motions in the modes 2, 3, and 4. The decrease in oscillation frequency was found to be proportional to the square of the amplitude, which agrees with the experimental results by Trinh and Wang [29], and numerical results by Foote [20]. The percentage of time spent in a prolate shape increases with increasing amplitude, which coincides with the numerical results by Foote [20]. Patzek et al. [33] analysed the nonlinear free oscillation of inviscid liquid droplets. The Laplace equation for the velocity potential in the liquid and the Bernoulli equation as the dynamic boundary condition at the free surface are solved numerically using the domain differential method together with a Galerkin finite-element formulation. By integration of the Navier-Stokes equations without the viscous term along the free surface, the Bernoulli equation is obtained. For irrotational flows, the mass continuity equation is transformed into the Laplace equation for the velocity potential. The predictions accord with those of Lundgren and Mansour [34], who employed the domain integral method. The results are in good agreement with the linear analysis of Rayleigh [5] for infinitesimal amplitude oscillations and the perturbation results of Tsamopoulos and Brown [30] for non-linear oscillations. Inspired by the method of Kistler and Scriven [35], and Patzek et al. [33], Basaran [36] numerically studied the nonlinear free oscillation of viscous liquid droplets in a vacuum or a gas of negligible density and viscosity by solving continuity and Navier-Stokes equations with appropriate interfacial conditions, based on the Galerkin/finite-element method. Droplet oscillations are released from an initial static deformation. Two initial droplet shapes are considered: a prolate/oblate spheroid and a droplet shape whose departure from a sphere is expanded as spherical harmonics. Different Reynolds number Re and the initial droplet deformation are taken into account. It was found that the nonlinear frequency shift and the asymmetry in the time spent in different configurations depend on the Reynolds number. Released from a two-lobed configuration, viscous droplets spend less time in the prolate shape than inviscid ones. The oscillation frequency of viscous droplets decreases with the square of the initial deformation amplitude for large Re, but the difference is smaller for small Re or a large initial deformation amplitude. The damping rate in the first period increases for a large initial droplet deformation. Wang et al. [37] experimentally studied oscillations of low-viscosity droplets in a microgravity environment during a space shuttle flight. The experiments are conducted in a triaxial acoustic chamber, in which standing sound fields can manipulate the liquid droplets and control the droplet position. Two situations are taken into account: an initially oblate droplet is suddenly released by turning off all acoustic fields; a prolate droplet is gyrostabilized through an imposed rotation. For a rotating droplet, an oblate shape can be concave at the poles. For a free oscillating droplet of small amplitude, the frequency shift agrees well with the predictions by the inviscid nonlinear theory of Tsamopoulos and Brown [30]. But for an oscillating droplet while rotating, the frequency shift is smaller and the percentage of time spent in a prolate form is much less than that predicted by the theory of Tsamopoulos and Brown [30]. As Re is much larger than 10, the frequency shift of a low-viscosity droplet can be regarded as inviscid. Zrnić and Brenn [38] analysed weakly nonlinear shape oscillations of inviscid droplets in a vacuum. The velocity, pressure, and the droplet shape are expanded as a third-order power series of a small deformation parameter. To impose the boundary conditions on the undisturbed surface, the velocity and pressure on the deformed droplet surface are expanded in a Taylor series. The method of strained time [39] is also employed. The continuity and momentum equations are decomposed into three series equations of the first to third order. The analysis of the initial droplet shape of modes 2, 3, and 4 is carried out. The solution of the series equations of the first order represents the linear part, and the solutions of the higher orders consider the nonlinear influence. The volume conservation for different initial droplet shape modes and droplet oscillation amplitudes is verified. By the Fourier frequency power spectra, the oscillation frequency is obtained. It was found that the frequency decrease with increasing deformation for mode 2 is a third-order effect, and for higher modes is in the second-order approximation. The asymmetry in time spent in various configurations is in good agreement with the results of Foote [20], Trinh and Wang [29], Tsamopoulos and Brown [30], and Wang et al. [37]. In [40], oscillating droplets were simulated by direct numerical simulation using an extended discontinuous Galerkin method [41]. Oscillation frequency, asymmetry in time spent in the various configurations, the evolution of the aspect ratio and energy by DNS and the weakly nonlinear linear theory are presented and in good agreement. Recently, Tonini and Cossali [42] investigated small and large amplitude spheroidal droplet oscillations with an analytical model using a novel method. The droplet shape is assumed to be spheroidal. A generalized spheroidal coordinate system is proposed, which involves the prolate, spherical, and oblate coordinate systems in a unified way, exclusively by an additional deformation parameter. The viscous and inertial effects in the droplet and the surrounding fluid are considered. The energy balance between the kinetic energy, surface energy, and dissipation energy is solved to derive a non-linear ordinary differential equation for the deformation parameter. For small amplitude oscillations, the oscillation frequency and amplitude decay rate for different Ohnesorge number Oh are in good agreement with the results by Prosperetti [17]. The effect of the density ratio on the oscillation frequency coincides with the results by Lamb [6]. For large amplitude oscillations, the amplitude decay rate agrees with the results by Miller and Scriven [7]. The time spent in various configurations is close to the results by Tsamopoulos and Brown [30].

Helenbook and Edwards [43] conducted numerical simulations to study a quasi-steady deformation of liquid droplets in a uniform gaseous stream, using a two-fluid spectral/hp finite element method. Several simulations with different density ratios, viscosity ratios, We and Oh numbers are performed to investigate the droplet behaviour. Three distinct droplet shapes and the conditions of their appearance are given: prolate, oblate, and dimpled. An oblate shape appears due to the aerodynamic effects in the surrounding gas flow. The appearance of a prolate shape is attributed to the liquid circulation instead of the gas flow. High-pressure regions exist at the leading and trailing edges inside the droplet due to the internal circulation. A combined effect of gas viscous stresses and aerodynamic forces leads to the formation of a dimpled shape in the case of large Oh numbers. When viscous effects are less significant, a dimpled shape will not occur. A drag model for deformed droplets is proposed, including a correlation for the effect of the internal circulation on the drag for spherical droplets and a deformation correlation. Loth [44] reviewed the deformed conditions for quasi-steady shape of droplets in a gas stream in the literature [45–50], and proposed a correlation for aspect ratio and drag coefficient in terms of We number, Re number, density ratios, and viscosity ratios. It was found that the aspect ratio is solely dependent on We number for $Re > 100$. Minimum drag (for a spherical shape) and maximum drag (for a maximum deformed shape) were given. The variation of the drag coefficient between the minimum and maximum values was also discussed.

Busse [51] investigated oscillations of a rotating droplet. The effect of rotation on droplet oscillations is accounted through the Coriolis force and the centrifugal effects. For axisymmetric oscillations, both the Coriolis force and centrifugal force work together to increase the oscillation frequency when the droplet density is larger than the ambient density. When the interior density is equal to the exterior density, the effect of the centrifugal force disappears. Patzek et al. [52] studied nonlinear oscillations of a two-dimensional rotating inviscid droplet by numerically solving an integro-differential Bernoulli equation for the droplet shape and Laplace equation for the velocity potential. Galerkin's weighted residual method with finite element basis functions is employed. Through the Fourier power spectral analysis of large amplitude oscillations, it was found that the frequency shift of a rotating droplet due to nonlinear oscillations is similar to that of a non-rotating droplet.

2.3 State of the Art in Droplet Evaporation

The study of droplet heating and evaporation has been of great interest to researchers. As a pioneer, Maxwell [53] considered only the diffusion mechanism for the evaporation of a liquid droplet in a stagnant gas environment. Fuchs [2] extended the work of Maxwell by accounting for Stefan flow by the zero net flux of the inert gas towards the droplet. Kronig and Brink [54] investigated a falling/rising droplet in another liquid. The circulation inside the droplet, caused by the viscous force between two fluids, is taken into account by Hadamard's solution [6, 55]. The diffusion equation in a new curvilinear coordinate system, which is based on the streamline of the internal circulation, is solved.

The convective term is zero, due to this new coordinate system and the assumption that the time scale of the circular transport is much smaller than that of the diffusion (large Pe number). The mass diffusion is assumed to be only normal through the streamline. The analytical solution of the extraction rate can be obtained by variable separation and polynomial approximation. It was found that the extraction rate of such a droplet is enhanced by a factor of 2.5, compared to a stagnant droplet by [56]. Prakash and Sirignano [57] studied the liquid droplet heating in a hot convective flow, by analysing the liquid-phase motion and droplet heating that considered a spherical vortex surrounded by the viscous boundary layer and internal wake. By modifying the inviscid Hill's vortex solution [58, 59] with a perturbation [60], the viscous boundary layer inside the droplet is analysed in an orthogonal boundary layer coordinate system that is between the front and rear stagnation points and between the droplet surface and the edge of the boundary layer. Based on an order-of-magnitude analysis, the momentum and energy equations retain only the convective term tangential to the droplet surface. In the spherical core, the Hill's vortex solution is adopted. The heat diffusion is assumed to be only normal through the streamline. The unsteady energy equation is numerically solved, with boundary conditions of fixed temperature or fixed heat flux. It was found that the droplet motion is still a Hill's vortex, but of different strength. The heating time of the spherical core is independent of the vortex strength since the thermal diffusion is essentially normal through the streamlines. For a fixed heat flux, a linear temperature profile is obtained. For a fixed boundary temperature, it takes about 10% of the thermal diffusion time to reach a fully heated core. Then, [61] developed a gas-phase boundary layer analysis using an integral approach and coupled it with the previous liquid-phase analysis [57], to study the droplet evaporation in a hot convective flow. An integral form of the conservation equations of the boundary layer in an orthogonal boundary layer coordinate system is applied, and the velocity, density/temperature, and vapour mass fraction are assumed to have fourth-degree polynomial profiles [62]. Gas- and liquid-phase equations are coupled through the boundary conditions at the interface. In the free stream, the flow is assumed to be potential. The velocity, temperature, and vapour mass fraction profiles are assumed to smoothly match the free stream at the edge of the boundary layer. It was found that the temperature inside the droplet is nonuniform and the unsteady evaporation rate persists for most of the droplet's lifetime. The predicted evaporation rate is lower than the results by Ranz and Marshall [63] and Spalding [64] correlations, due to ignoring the wake region. Abramzon and Sirignano [65] proposed an extended liquid heating model to study the droplet evaporation in a stream flow. In the gas phase, the convective effect caused by the droplet motion in the gas is taken into account by film theory [62, 66]. Due to the Stefan flow, the film thickness is modified by a factor that is approximated as a function of Spalding numbers. In the liquid phase, the internal circulation is considered by the Hill spherical vortex solution [67, 68]. The temperature is governed by a dimensionless energy equation, which includes three limit cases: the infinite conductivity model, vortex model, and conduction limit model. The evaporation rate, surface temperature, and instantaneous radius predicted by these models are compared. The results obtained from the extended model were found to be in good agreement with those from the effective conductivity model [69, 70], in which the influence of internal circulation is represented through an effective thermal conductivity. The effective conductivity model does not consider the physical details related to the internal circulation, but it properly reflects the global effect of the internal circulation on the heat transfer and can be applied in the spray to effectively obtain a reliable surface temperature. The evolution of the temperature profile inside the droplet is reported. It verifies the vortex model at high Pe number, in which the streamlines and isothermal lines coincide well, and captures the transition to the conduction limit model at lower Pe number.

In most practical applications, the assumption of spherical droplets may be questionable. The deformed droplet may have various evaporation characteristics. Tonini and Cossali [71] proposed an analytical evaporation model for a spheroidal droplet. The time scale of the heat/mass transfer is assumed to be much smaller than that of the droplet oscillation. A steady species conservation equation in the gaseous phase is analytically solved in the prolate/oblate coordinate system. The steady vapour distribution, the evaporation flux, and the evaporation rate are obtained. The energy equation, including convective and diffusive terms, is solved for the heating rate. It was found that the evaporation flux is proportional to the non-dimensional Gauss curvature to the power of 1/4. A prolate droplet has a higher evaporation rate than an oblate one with the same surface area. Compared with a spherical droplet, the heating/evaporation rate of a spheroidal droplet is enhanced by a factor that is a function of aspect ratio. In [72], the conditions of droplet size and gas and droplet temperature, when the quasi-steady assumptions may be accepted, were derived. Tonini and Cossali [73] extended the previous results for spheroids [71] and derived a general analytical solution for the quasi-steady evaporation of a triaxial ellipsoidal droplet. The steady species and energy equations are solved in a triaxial ellipsoidal coordinate system. The heat/mass fluxes are orthogonal to the droplet surface. The evaporation rate and local heat and mass transfer are expressed as a 1-D solution that is orthogonal to the coordinate surface defined by the droplet surface. The local evaporation flux was found to be the fourth root of the dimensionless Gauss curvature, as in [71] for a spheroidal droplet. The evaporation rate of deformed droplets with the same volume and surface area has a maximum for a prolate shape, but a minimum for an oblate one. A triaxial ellipsoidal droplet has an evaporation rate between them. Schlottke and Weigand [74] conducted direct numerical simulations to study the evaporation of deformed droplets in a gas stream with the in-house code FS3D (Free Surface 3D). The evaporation rate is evaluated by the vapour mass fraction and the reconstructed surface through the PLIC method. The results are validated with the correlations by [63,75,76]. Two vortex pairs are generated in the wake region of the droplet. They cause a strong mixing and homogeneous temperature distribution inside the droplet. Al Zaitone [77] investigated the evaporation of an oblate droplet at constant aspect ratio by continuously adjusting the acoustic force during the evaporation process. A 2D heat diffusion equation inside the droplet in an oblate coordinate system is numerically solved by a numerical scheme named Alternating Direction Implicit (ADI) [78]. The heat and mass transfer coefficient are correlated due to the acoustic boundary layer. Both experimental and numerical results agree well, and with the results by Yarin et al. [79]. As the droplet deformation increases, the evaporation rate also increases. It was found that the evaporation of spheroidal droplets follows the D^2 law. Setiya and Palmore [80] investigated the effect of a quasi-steady deformed droplet in a convective flow on the evaporation rate by direct numerical simulation at varying Re and We numbers. The validation is done by comparison with the result of Abramzon and Sirignano [65]. It was found that the increase in the surface area due to the deformation is dominant for the enhancement of the evaporation, but the averaged evaporation flux seems to be close. At a low Re number, the evaporation rate weakly depends on the We number. While at a large Re number, a dependence can be observed.

Experimental [81] and numerical [74, 82] studies show that the surface temperature distribution is generally non-uniform. Tonini and Cossali [83] investigated the effect of non-uniform surface temperature on the evaporation and heating of spherical and spheroidal droplets in a still gaseous environment by solving the species conservation and energy equations in the gaseous phase. Based on [71], an analytical solution of the evaporation rate is given. The vapour mass fraction at the droplet surface is calculated by the droplet temperature. The energy equation is solved numerically, with a non-uniform surface temperature. The droplet surface temperature is approximated by a polynomial of four orders, as well as the vapour mass fraction at the surface. Various surface temperature profiles are considered. The local heat transfer coefficient depends on both local temperature and curvature. For a non-uniform surface temperature distribution, it was found that the heat flux at the droplet surface is not orthogonal to the droplet surface, nor is the evaporation flux. The total heat rate is less affected by the non-uniform surface temperature. Compared with a droplet of uniform surface temperature, the evaporation rate increases as the temperature difference grows. The scaling of the evaporation rate on the droplet deformation is independent of the temperature distribution. Based on the work of Tonini and Cossali [83], Antonov et al. [84] proposed a heating and evaporating model of a spheroidal droplet with non-uniform surface temperature. The gas model is coupled with the liquid model through the jump conditions at the interface. In the gas phase, the species conservation equation is again analytically solved [83], but the heat flux is described by a modified heat transfer coefficient due to non-uniform surface temperature, which is correlated from the results in [83]. In the liquid phase, the transient heat equation without convective terms is solved. The simulation results for a droplet of uniform temperature and various aspect ratios in a hot environment are discussed. Droplet oscillation is not considered. It was found that the maximum temperature appears in the regions of maximum curvature. The surface temperature non-uniformity increases in the initial heating period due to the non-uniform heat flux at the droplet surface. Then it decreases through the heat transfer inside the droplet. The evaporation flux in the regions of higher curvature also has a higher value [71]. The D^2 law is observed after the initial heating period for spherical and spheroidal droplets. The evaporation process drives the droplet more spherical, but very slowly.

Fuel droplets, medical aerosols, and so on, consist of various components that have different physical properties. Different components may evaporate at different rates. Thus, a gradient of the component concentration inside the droplet develops. Therefore, the mass and heat diffusion of each component inside the droplet need to be taken into account. The Discrete Component Model is suitable in the case when the number of components is small. Tong and Sirignano [85] proposed an evaporation model for a single-component or bi-component droplet in a hot convective gas stream. For a single-component droplet, the gas- and liquid-phase analyses are coupled through the evaporation. The liquid heat equation is solved in a streamline coordinate, considering the internal circulation and droplet evaporation. The momentum and continuity equations in the gas boundary layer are transformed into the Blasius equations. The surface temperature is obtained from a Volterra-type integral equation derived from the energy balance [86]. For a bi-component droplet, the Spalding mass transfer number in the gas phase is modified, and the species equation in the liquid phase is additionally solved. Similar to the solution of a single-component droplet, the equations are first transformed into several first-order ordinary differential equations, and numerically solved by a second-order Runge-Kutta scheme. Maqua et al. [87] investigated the evaporation of a bi-component droplet in a hot gas. The temperature was measured, based on the three-colour laser-induced fluorescence technique, by adding a fluorescent organic dye to the droplet. The numerical model considers the droplet heating with the internal circulation and liquid composition by a Discrete Component Model. The experimental and numerical results for droplet evaporation in a hot air plume are in good agreement. More studies on a droplet of a small number of components can be found in [88–90]. For droplets of a large number of components, the Discrete Component Model becomes less effective, and the Continuous Thermodynamics approach [91, 92] or the Distillation Curve model [93] are typically suitable.

Although extensive studies on droplet evaporation exist, the effect of a moving interface on droplet evaporation has received relatively limited attention. The evaporation of deformed droplets has been discussed. However, in many models the droplet shape is assumed to remain stable and the quasi-steady assumption is typically adopted. Therefore, relaxing the quasi-steady assumption, and investigating the effect of a moving interface on the evaporation characteristics are the main focus of the present work. Other factors, such as temperature variation and temperature dependence of thermophysical properties, are neglected in the present study.

Chapter 3. Governing Equations and Mathematical Framework

This section presents the formulation adopted in the present study. The governing equations describing the two-phase flow and interfacial mass transfer are first presented. The equations are subsequently non-dimensionalized, and the relevant physical parameters are identified.

To describe the deformation of the droplet surface, a generalized spheroidal coordinate system is employed. Under the assumption that the droplet maintains a spheroidal shape, the moving-boundary problem is reformulated as a problem with a fixed boundary in a time-dependent coordinate system. The interface motion is then characterized by a deformation parameter that varies in time. This geometric treatment enables the separation of variables of the Laplace equation and provides a convenient basis for the subsequent oscillation and evaporation analyses.

The classical normal mode representation of droplet oscillation based on spherical harmonics is first revisited as a reference formulation. The spheroidal geometric description adopted in the present study is then compared with the classical spherical harmonic representation truncated at the mode $l = 2$. The modelling hierarchy employed in this study is established. The underlying assumptions, such as potential flow behaviour and geometric constraints, are clearly stated in order to define the scope of applicability of the analytical framework.

Numerical tools are briefly introduced at the end of this section. They serve as a complementary approach to the analytical model and allow the investigation of physical effects that are not captured under the simplifying assumptions. The detailed analyses are presented in Chapters 4 and 5.

3.1 Physical Configuration

We consider a deforming droplet undergoing axisymmetric oscillations while evaporating into a surrounding gaseous environment. The system is treated within the framework of continuum mechanics. At any time t, the moving interface $\Xi(t)$ separates the time-dependent domains $\Omega^+(t)$ and $\Omega^-(t)$. Their surfaces are denoted by $\partial\Omega^+(t)$ and $\partial\Omega^-(t)$, respectively, as illustrated in Fig 1. The interface $\Xi(t)$ constitutes the common boundary between the two domains. n^+ and n^- are normal vectors of the dividing surface. On the interface $\Xi(t)$, they satisfy $n^+ = -n^-$.

In the present thesis, $\Omega^-(t)$ corresponds to the liquid droplet, whereas $\Omega^+(t)$ denotes the surrounding gas phase composed of vapour of the droplet liquid and the inert air.

The instantaneous volume of the droplet is defined as

$$Vol(t) = \int_{\Omega^-(t)} \mathrm{d}V, \tag{3.1}$$

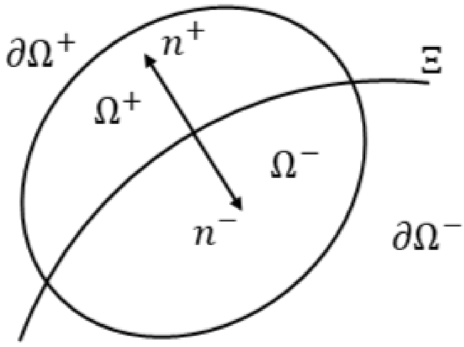

Figure 1: Schematic representation of the domains Ω^+ and Ω^- separated by the interface Ξ.

and the corresponding volume-equivalent radius $R(t)$ is introduced through

$$R(t) = \left(\frac{3Vol(t)}{4\pi}\right)^{1/3} \tag{3.2}$$

This radius provides a natural reference length scale and allows a consistent description of both oscillation deformation and evaporation-induced volume decrease. In the absence of evaporation, $R(t)$ remains constant and coincides with the initial droplet radius.

Both phases are assumed incompressible and Newtonian. Surface tension acts at the interface and contributes to the normal stress balance through the local curvature. Mass transfer across the interface is driven by vapour diffusion in the gas phase. Gravitational effects are neglected, consistent with droplets sufficiently small for capillary forces to dominate.

The governing equations and interfacial conditions corresponding to this configuration are introduced in the following sections.

3.2 Conservation Equations

The governing equations are formulated within the framework of continuum mechanics. The physical configuration introduced in Section 3.1 consists of two domains, separated by a dividing interface. Although the problem involves two phases, the local conservation equations are first introduced within each phase. We consider a material volume $\Omega(t)$ that moves with the local fluid velocity, bounded by a closed surface $\partial\Omega(t)$.

To relate the time change rate of a mass-specific quantity Ψ inside $\Omega(t)$ to local variables, the Reynolds transport theorem is employed [94–96]:

$$\frac{d}{dt}\int_{\Omega(t)} \rho\Psi dV = \int_{\Omega(t)} \frac{\partial(\rho\Psi)}{\partial t} dV + \int_{\partial\Omega(t)} \rho\Psi u \cdot n dS \tag{3.3}$$

n denotes the outward unit normal vector on $\partial\Omega(t)$. Using the divergence theorem to convert the surface integral into a volume integral yields:

$$\frac{d}{dt}\int_{\Omega(t)} \rho\Psi dV = \int_{\Omega(t)} \left(\frac{\partial(\rho\Psi)}{\partial t} + \nabla\cdot(\rho\Psi u)\right) dV \tag{3.4}$$

This identity establishes the connection between the integral formulation of the conservation laws and their local differential form. In the following subsections, each conservation law is first written in integral form and subsequently localized.

3.2.1 Mass and Species Conservation

The conservation of total mass over the material volume $\Omega(t)$ requires:

$$\frac{d}{dt}\int_{\Omega(t)} \rho dV = 0 \tag{3.5}$$

Using the Reynolds transport theorem introduced above and applying the divergence theorem by setting $\Psi = 1$, the integral balance can be written as:

$$\int_{\Omega(t)} \left(\frac{\partial\rho}{\partial t} + \nabla\cdot(\rho u)\right) dV = 0 \tag{3.6}$$

Since $\Omega(t)$ is arbitrary, the integrand must be zero:

$$\frac{\partial\rho}{\partial t} + \nabla\cdot(\rho u) = 0 \tag{3.7}$$

For incompressible flow within each phase, where the density is constant, the continuity equation reduces to

$$\nabla\cdot u = 0 \tag{3.8}$$

In many low-Mach-number flows ($Ma < 0.3$), compressibility effects are small. In this thesis, both phases are treated as incompressible. In the presence of droplet evaporation, the gas phase is a mixture of vapour and air, not a single-component fluid. Evaporation is described by a convection-diffusion process of the vapour. Taking into account a fluid consisting of n species, the mass rate of the i^{th} species is equal to the mass diffusion of this species $j^{(i)}$ through the volume surface:

$$\frac{d}{dt}\int_{\Omega(t)} \rho^{(i)} dV = -\int_{\partial\Omega(t)} j^{(i)}\cdot n dS \tag{3.9}$$

Taking $\Psi = \chi^{(i)}$, where $\chi^{(i)} = \frac{\rho^i}{\rho}$ is the mass fraction of the i^{th} species, the species conservation equation read:

$$\int_{\Omega(t)} \left(\frac{\partial\rho\chi^{(i)}}{\partial t} + \nabla\cdot(\rho\chi^{(i)}u) + \nabla\cdot j^{(i)}\right) dV = 0 \tag{3.10}$$

then the differential form is:

$$\frac{\partial(\rho\chi^{(i)})}{\partial t} + \nabla\cdot(\rho\chi^{(i)}u) + \nabla\cdot j^{(i)} = 0,\ or\ \frac{\partial(\rho\chi^{(i)})}{\partial t} + \nabla\cdot n^{(i)} = 0 \tag{3.11}$$

where $n^{(i)}$ is the mass flux of i^{th} species, consisting of the convective part $\rho\chi^{(i)}u$ and the diffusive part $j^{(i)}$:

$$n^{(i)} = \rho^{(i)}u^{(i)} = \rho^{(i)}u + \rho^{(i)}(u^{(i)} - u) = \rho\chi^{(i)}u + j^{(i)} \tag{3.12}$$

$u^{(i)}$ is the velocity of i^{th} species, which is distinguished from the material velocity u. $j^{(i)}$ is the diffusive flux. In the present bi-component mixture, the diffusive flux is described by Fick's Law [97,98], $j^{(i)} = -\rho D^{(i)}\nabla\chi^{(i)}$, with the mass diffusive coefficient $D^{(i)}$ of i^{th} species. Suppose that a material element at rest has two components of reverse fraction gradient. Due to the species diffusion, the velocity of the species is not zero, but the average velocity of the two components is the velocity of the material element (vanishes). This difference, due to the movement of molecules against the gradient of species fraction, is named diffusive flux. For a multicomponent mixture, the diffusive flux $j^{(i)}$ should be evaluated by Maxwell-Stefan equations [99].

By summation of all species conservation Eqn. 3.11, the mass conservation Eqn. 3.7 is recovered, since the total diffusive fluxes of all species must be zero $\sum_{i=1}^{n} j^{(i)} = 0$.

In our present work on droplet evaporation, a single-component droplet is considered and the gas phase is assumed to consist of two components, vapour and air. Under assumptions of quasi-steadiness of mass and heat transport through the interface, the species conservation equations are simplified as $\nabla\cdot n^{(i)} = 0$. Its analytical solutions can be found in [71,72].

3.2.2 Momentum Conservation

Newton's second law states that the momentum change rate of an object is equal to the forces acting on it [100]. Setting $\Psi = u$, we derive:

$$\begin{aligned}\int_{\Omega(t)}\left(\frac{\partial(\rho u)}{\partial t} + \nabla\cdot(\rho uu)\right)dV &= \int_{\Omega(t)}\rho f dV + \int_{\partial\Omega(t)}\tau\cdot ndS\\ &= \int_{\Omega(t)}(\rho f - \nabla p + \nabla\cdot S)dV \end{aligned}\tag{3.13}$$

where f denotes the volume force and $\tau = -pI + S$ represents the Cauthy stress tensor acting on the surface, with the thermodynamic pressure p, unit tensor I and the deviatoric stress tensor $S = \mu\left(\nabla u + (\nabla u)^T\right)$ (μ dynamic viscosity)) [101,102].

The differential form reads:

$$\frac{\partial(\rho u)}{\partial t} + \nabla\cdot(\rho uu) = \rho f - \nabla p + \nabla\cdot S \tag{3.14}$$

3.2.3 Energy Conservation

For a material volume $\Omega(t)$, the energy balance is expressed in terms of the specific enthalpy h [103]:

$$\frac{d}{dt}\int_{\Omega(t)} \rho h dV = -\int_{\partial\Omega(t)} q \cdot n dS + \int_{\Omega(t)} \frac{d_{(m)}p}{dt} dV + \int_{\Omega(t)} S : \nabla u dV \tag{3.15}$$

where the diffusive heat flux q is generally evaluated by Fourier's Law $q = -\lambda\nabla T$ (λ thermal conductivity) [104, 105] and $\frac{d_{(m)}}{dt} = \frac{\partial}{\partial t} + u \cdot \nabla$ is the material derivative. The local differential form becomes:

$$\frac{\partial(\rho h)}{\partial t} + \nabla \cdot (\rho u h) = -\nabla \cdot q + \frac{d_{(m)}p}{dt} + S : \nabla u \tag{3.16}$$

For small Eckert numbers, the viscous heating term $S : \nabla u$ is negligible. In most practical applications, the pressure work term can be neglected unless the fluid undergoes a significant pressure change or the Mach number is large. In the analytical evaporation model introduced later, the energy equation is not solved. However, it is included here for completeness and for the consistency with DNS simulations, where the temperature field is computed.

3.3 Jump Conditions, Evaporation Flux and Evaporation Rate

To obtain the interfacial jump conditions, we now consider an arbitrary control volume that may intersect a moving interface Ξ, as illustrated in Fig 1. In the present work the liquid-gas interface that distinguishes the continuous (gaseous) from the discontinuous (liquid) phase [106, 107], is simplified as a dividing surface, rather than a region of the thickness of several molecular diameters. Across which, field variables (e.g. density and velocity) may be discontinuous. The control volume is split into two domains Ω^+ and Ω^-, separated by Ξ. Their outer boundaries are denoted by $\partial\Omega^+$ and $\partial\Omega^-$, respectively. The normals n^+ and n^- correspond to the unit normal vectors of Ω^+ and Ω^- on Ξ. In the followings, the gaseous (subscript G) and liquid (subscript L) phases correspond to domain Ω^+ and Ω^-. The unit normal vector of the interface n is set as $n = n^+ = -n^-$. V refers the interface velocity. For a specific quantity Ψ, we have:

$$\frac{d}{dt}\int_{\Omega^+} \rho\Psi dV = \int_{\Omega^+} \frac{\partial\rho\Psi}{\partial t} dV + \int_{\partial\Omega^+} \rho\Psi u \cdot n dS + \int_{\Xi} (\rho\Psi)^+ V \cdot (-n^+) dS \tag{3.17}$$

and

$$\frac{d}{dt}\int_{\Omega^-} \rho\Psi dV = \int_{\Omega^-} \frac{\partial\rho\Psi}{\partial t} dV + \int_{\partial\Omega^-} \rho\Psi u \cdot n dS + \int_{\Xi} (\rho\Psi)^- V \cdot (-n^-) dS \tag{3.18}$$

where the minus sign in the last integrand is due to the chosen normal. $(\rho\Psi)^+$, $(\rho\Psi u)^+$ and $(\rho\Psi)^-$, $(\rho\Psi u)^-$ are the values approaching the dividing surface from the two regions. Summing the last two equations, we have:

$$
\begin{aligned}
&\frac{d}{dt}\int_\Omega \rho\Psi dV = \int_\Omega \frac{\partial\rho\Psi}{\partial t}dV + \int_{\partial\Omega+\Xi}\rho\Psi u\cdot ndS + \int_\Xi (\rho\Psi u)^+\cdot n^+dS\\
&+\int_\Xi (\rho\Psi u)^-\cdot n^-dS + \int_\Xi -(\rho\Psi)^+V\cdot n^+dS + \int_\Xi -(\rho\Psi)^-V\cdot n^-dS\\
&=\int_\Omega \frac{\partial\rho\Psi}{\partial t}dV + \int_{\partial\Omega+\Xi}\rho\Psi u\cdot ndS + \int_\Xi \left[(\rho\Psi)^+(u^+-V)-(\rho\Psi)^-(u^--V)\right]\cdot ndS\\
&=\int_\Omega\left(\frac{\partial\rho\Psi}{\partial t}+\nabla\cdot(\rho\Psi u)\right)dV + \int_\Xi \left[(\rho\Psi)^+(u^+-V)-(\rho\Psi)^-(u^--V)\right]\cdot ndS
\end{aligned}
\tag{3.19}
$$

3.3.1 Jump Conditions

Now the conservation equations containing a dividing surface between gaseous and liquid phases are discussed, from which the jump conditions are derived.

By setting $\Psi = 1$ in Eqn. 3.19, we have the integral mass balance for a control volume intersected by the interface:

$$
\int_\Omega\left(\frac{\partial\rho}{\partial t}+\nabla\cdot(\rho u)\right)dV + \int_\Xi[\rho_G(u_G-V)-\rho_L(u_L-V)]\cdot ndS = 0 \tag{3.20}
$$

Since the local mass conservation equation holds within each bulk phase, the volume integral vanishes. Therefore, we have the mass jump condition:

$$
\rho_G(u_{G,n}-V_n) = \rho_L(u_{L,n}-V_n) \tag{3.21}
$$

Setting $\Psi = \chi^{(i)}$ in Eqn. 3.19, for the i^{th} species, we obtain the species conservation equation containing a dividing surface:

$$
\begin{aligned}
&\int_\Omega\left(\frac{\partial\rho\chi^{(i)}}{\partial t}+\nabla\cdot(\rho\chi^{(i)}u)\right)dV + \int_\Xi\left[\rho_G\chi_G^{(i)}(u_G-V)-\rho_L\chi_L^{(i)}(u_L-V)\right]\cdot ndS\\
&=-\int_{\partial\Omega} j^{(i)}\cdot ndS = -\int_\Omega\nabla\cdot j^{(i)}dV + \int_\Xi(-j_G^{(i)}+j_L^{(i)})\cdot ndS\\
&=-\int_\Omega\nabla\cdot j^{(i)}dV + \int_\Xi\left[-\rho_G\chi_G^{(i)}(u_G^{(i)}-u_G)+\rho_L\chi_L^{(i)}(u_L^{(i)}-u_L)\right]\cdot ndS
\end{aligned}
\tag{3.22}
$$

or

$$
\int_\Omega\left(\frac{\partial\rho\chi^{(i)}}{\partial t}+\nabla\cdot(n^{(i)})\right)dV + \int_\Xi\left[\rho_G\chi_G^{(i)}(u_G^{(i)}-V)-\rho_L\chi_L^{(i)}(u_L^{(i)}-V)\right]\cdot ndS = 0 \tag{3.23}
$$

Recalling Eqn. 3.11, the first integration is zero within each phase. Thus we have the species jump condition for any port of fluid:

$$
\rho_G\chi_G^{(i)}(u_{G,n}^{(i)}-V_n) = \rho_L\chi_L^{(i)}(u_{L,n}^{(i)}-V_n) \tag{3.24}
$$

In the present work, the gaseous phase consists of vapour(superscript v) and air (superscript a):

$$\begin{aligned}&\rho_G\chi_G^v(u_{G,n}^v - V_n) = \rho_L(u_{L,n} - V_n)\\ &\rho_G\chi_G^a(u_{G,n}^a - V_n) = 0\end{aligned}\tag{3.25}$$

Summing species jump conditions Eqn. 3.24, the mass jump condition Eqn. 3.21 is recovered. Setting $\Psi = u$ in Eqn. 3.19, we obtain the momentum equation containing a dividing surface:

$$\begin{aligned}&\int_\Omega\left(\frac{\partial\rho u}{\partial t} + \nabla\cdot(\rho uu)\right)dV + \int_\Xi[\rho_G u_G(u_G - V) - \rho_L u_L(u_L - V)]\cdot ndS\\ &= \int_\Omega \rho f dV + \int_{\partial\Omega}\tau\cdot ndS\\ &= \int_\Omega \rho f dV + \int_\Omega \nabla\cdot\tau dV + \int_\Xi(\tau_G - \tau_L)\cdot ndS\end{aligned}\tag{3.26}$$

Comparing with Eqn. 3.13, we have a vector momentum jump condition:

$$[\rho_G u_G(u_G - V) - \tau_G]\cdot n = [\rho_L u_L(u_L - V) - \tau_L]\cdot n\tag{3.27}$$

Here $\rho u(u - V)$ is a dyadic tensor. By projecting the vector momentum jump condition onto the normal direction of the interface, considering the surface tension and neglecting the viscous normal stresses $n\cdot S\cdot n$, we have:

$$\rho_G u_{G,n}(u_{G.n} - V_n) + p_G + \sigma\nabla\cdot n = \rho_L u_{L,n}(u_{L,n} - V_n) + p_L\tag{3.28}$$

where σ is the surface tension coefficient and $\nabla\cdot n$ represents the local curvature of the dividing surface [95].

Again setting $\Psi = e + \frac{1}{2}|u|^2$ (e internal energy) in Eqn. 3.19, we derive the energy equation containing a dividing surface:

$$\begin{aligned}&\int_\Omega\left(\frac{\partial\rho\left(e + \frac{1}{2}|u|^2\right)}{\partial t} + \nabla\cdot\left(\rho u(e + \frac{1}{2}|u|^2)\right)\right)dV\\ &+ \int_\Xi\left[\rho_G\left(e_G + \frac{1}{2}|u_G|^2\right)(u_G - V) - \rho_L\left(e_L + \frac{1}{2}|u_L|^2\right)(u_L - V)\right]\cdot ndS\\ &= -\int_{\partial\Omega} q\cdot ndS + \int_\Omega \rho f\cdot udV + \int_{\partial\Omega}\tau\cdot u\cdot ndS\\ &= -\int_\Omega \nabla\cdot qdS - \int_\Xi(q_G - q_L)\cdot ndS + \int_\Omega \rho f\cdot udV\\ &+ \int_\Omega \nabla\cdot(\tau\cdot u)dV + \int_\Xi(u_G\cdot\tau_G - u_L\cdot\tau_L)\cdot ndS\end{aligned}\tag{3.29}$$

Comparing with the total energy equation in each phase, we obtain the energy jump condition:

$$\begin{aligned}&\rho_G\left(e_G+\frac{1}{2}|u_G|^2\right)(u_{G,n}-V_n)+q_G\cdot n-u_G\cdot\tau_G\cdot n\\&=\rho_L\left(e_L+\frac{1}{2}|u_L|^2\right)(u_{L,n}-V_n)+q_L\cdot n-u_L\cdot\tau_L\cdot n\end{aligned}\tag{3.30}$$

or with $h=e+\frac{p}{\rho}$:

$$\begin{aligned}&\rho_G\left(h_G+\frac{1}{2}|u_G|^2\right)(u_{G,n}-V_n)+q_G\cdot n+u_{G,n}\sigma\nabla\cdot n+p_GV_n-u_G\cdot S_G\cdot n\\&=\rho_L\left(h_L+\frac{1}{2}|u_L|^2\right)(u_{L,n}-V_n)+q_L\cdot n+p_LV_n-u_L\cdot S_L\cdot n\end{aligned}\tag{3.31}$$

Comparing with Eqn. 3.21, and neglecting pressure term, the viscous normal stress and the kinetic energy, we have:

$$\rho_G(u_{G,n}-V_n)\Delta H_v-\lambda_G\nabla T_G\cdot n=-\lambda_L\nabla T_L\cdot n\tag{3.32}$$

Here $\Delta H_v=h_G-h_L$ is the latent heat.

3.3.2 Evaporation Flux and Evaporation Rate

As described in the previous section, this work considers a single-component droplet in a gaseous environment consisting of vapour and air. The evaporation flux is defined as:

$$n_{ev}=\rho_G^v(u_{G,n}^v-V_n)=\rho_G(u_{G,n}-V_n)=\rho_L(u_{L,n}-V_n)\tag{3.33}$$

by the mass and species jump conditions Eqn. 3.21 and 3.25, it describes the mass flux per unit area through the interface. It is distinguished from the vapour flux $n^v=\rho_G^vu_G^v$ defined by Eqn. 3.12, the evaporation flux is defined not only at the interface but also in the whole gaseous phase.

Eliminating V_n, we have $n_{ev}=\rho_G^v\left(u_{G,n}^v+\frac{n_{ev}}{\rho_G}-u_{G,n}\right)$. Then, by Fick's law $j_n^v=\rho_G^v(u_{G,n}^v-u_{G,n})=-\rho_GD^v\nabla_n\chi^v$, we derive the evaporation flux of the form:

$$n_{ev}=-\rho_GD^v\frac{1}{1-\chi^v}\nabla_n\chi^v\tag{3.34}$$

which is also implemented in an in-house code Free Surface 3D (FS3D) that will be described in Section 3.9 [108,109]. It is taken as positive when mass is transferred from the liquid to the gas phase. The evaporation flux is enhanced by a factor $\frac{1}{1-\chi^v}$ than the pure diffusive flux. This enhancement is due to the Stefan flow [110]. The 'evaporation flux' of air must be zero, $n_{ev}^a=\rho_G^a(u_{G,n}^a-V_n)=0$. It could be written as the summation of the diffusive part $j^a=\rho_G^a(u_{G,n}^a-u_{G,n})$ and convective part $\rho_G^a(u_{G,n}-V_n)$, $n_{ev}^a=j^a+\rho_G^a(u_{G,n}-V_n)$. The diffusive flux of air j^a is the opposite of the diffusive flux of the vapour j^v and does not vanish. So it leads to the additional velocity of the mixture of air and vapour ($u_{G,n}$ distinguishes from V_n). Therefore, the evaporation flux of vapour $n_{ev} = j^v + \rho_G^v(u_{G,n} - V_n)$ is enhanced. When existing the bulk velocity, the vapour concentration field is redistributed and the normal gradient of vapour concentration $\nabla_n \chi^v$ varies. Under quasi-steady assumptions [71,72], the normal interface velocity V_n is considered as zero. At the interface, $n_{ev} = n^v$ is satisfied (the vapour flux has no tangent component under quasi-steady conditions). The steady species conservation equation $\nabla n^v = 0$ is solved. The analytical solutions for the vapour distribution and vapour flux are obtained, as well as the evaporation flux [71].

The evaporation rate $\dot{M}$ of droplet evaporation is evaluated by integrating the evaporation flux over the droplet surface:

$$\dot{M} = \int_{\partial\Omega} n_{ev} dA \tag{3.35}$$

here dA represents the surface element, its formulation depends on the choice of the coordinate, introduced in Section 3.6. In the analytical model framework developed in Section 5, the evaporation flux is determined from the vapour convection-diffusion equation in the gas phase.

3.4 Non-dimensionalization and Dimensionless Groups

To non-dimensionalise the governing equations, the volume-equivalent radius R is chosen as the characteristic length scale. The characteristic time scale of oscillation is $t_\omega = \frac{1}{\omega_L}$ with the oscillation frequency ω_L, and the characteristic time scale of the diffusion is $t_D = \frac{R^2}{D}$ with the binary diffusivity of the vapour in the gas. Then the dimensionless variables are defined as:

$$x^* = \frac{x}{R}, \quad t^* = \omega_L t, \quad u^* = \frac{u}{R\omega_L}, \quad p^* = \frac{pR}{\sigma}, \quad \omega^* = \frac{\omega}{\omega_L} \tag{3.36}$$

here x represents the coordinate and ω is the vorticity, to be distinguished from the oscillation frequency ω_L.

The dynamic viscosity μ is assumed to be constant, then the dimensionless momentum equation reads:

$$\frac{\rho R^3 \omega_L^2}{\sigma}\left(\frac{\partial u^*}{\partial t^*} + u^* \cdot \nabla^* u^*\right) = -\nabla^* p^* + \frac{\mu \omega_L R}{\sigma} \nabla^{*2} u^* \tag{3.37}$$

By considering the oscillation frequency $\omega_L \approx \omega_2 = \sqrt{\frac{8\sigma}{\rho R^3}}$, where ω_2 is the oscillation frequency in mode 2 by Rayleigh [5], the coefficient in the viscous term becomes:

$$\frac{\mu \omega_L R}{\sigma} \approx \sqrt{8}\frac{\mu}{\sqrt{\rho \sigma R}} = \sqrt{8} Oh \tag{3.38}$$

where Ohnesorge number $Oh = \frac{\mu}{\sqrt{\rho\sigma R}}$ compares the viscous diffusion time scale $\frac{R^2}{\nu}$ with the oscillation time scale $t_\omega = \frac{1}{\omega_L}$. Small Oh number indicates weak viscous damping of the oscillations.

When neglecting the geometry stretching term $\omega \cdot \nabla u$ in the vorticity equation due to the axisymmetric oscillation, the nondimensional vorticity equation reads:

$$\frac{\partial \omega^*}{\partial t^*} + u^* \cdot \nabla^* \omega^* = \frac{\nu}{\omega_L R^2} \nabla^{*2} \omega \tag{3.39}$$

where $\nu = \frac{\mu}{\rho}$ is kinematic viscosity. The penetration depth of the disturbance δ is defined as:

$$\delta = \sqrt{\frac{\nu}{\omega_L}} \tag{3.40}$$

It represents the oscillatory viscous layer thickness [37]. When no convective term is considered, it reduces to a one-dimensional Stokes oscillation problem.

In the presence of the evaporation, the vapour transport in the gas phase is described by the species conservation equation. Its dimensionless form reads:

$$\frac{\partial \chi}{\partial t^*} + u^* \cdot \nabla^* \chi = \frac{D}{\omega_L R^2} \nabla^{*2} \chi \tag{3.41}$$

In the following part of this thesis, χ refers to the vapour mass fraction in the gas phase for simplification. $Pe = \frac{\omega_L R^2}{D}$ is the Péclet number, defined as the ratio between the characteristic oscillatory advection velocity scale $R\omega_L$ and the diffusive transport velocity scale $\frac{D}{R}$. Equivalently, it also represents the time scale ratio of diffusion to oscillation $Pe = \frac{t_D}{t_\omega}$. For $Pe << 1$, the quasi-steady assumption holds, the convective transport induced by a moving interface is ignored (but the Stefan flow still needs to be considered) [71, 72]. In this thesis, the effect of the moving interface on the evaporation characteristics is the main focus. So Pe will be set of order $O(1)$ in the analytical model, and the convection-diffusion equation of the vapour is solved.

3.5 Potential Flow and Laplace's Equation

In the analytical modelling framework adopted in this thesis, the flow fields inside and outside the droplet are described under the assumption of potential flow. Specifically, the flow is assumed inviscid and irrotational, so that $\nabla \times u = 0$ and the velocity can be represented by a velocity potential Φ, $u = \nabla\Phi$. The incompressible flow is assumed, i.e. $\nabla \cdot u = 0$. Then the velocity potential satisfies the Laplace equation $\nabla^2\Phi = 0$.

Although the instantaneous velocity field is described as inviscid and irrotational, viscosity is taken into account by energy dissipation in the evolution equation of the oscillation amplitude, instead of entering the momentum equation. Following the strategy introduced by Tonini and Cossali [42], the instantaneous spatial structure of the flow is determined from the solution of the Laplace's equation under the assumption of potential flow, while energy dissipation due to the viscosity modifies the temporal evolution of the oscillation. In this way, the model combines an irrotational and inviscid description for the instantaneous flow field with a dissipative temporal evolution for the droplet oscillation.

The Laplace equation of a scalar f is written as [99, 111, 112]:

$$\nabla^2 f = 0 \tag{3.42}$$

Its general harmonic solution in a spherical coordinate system (r, θ, φ) reads (refer to Appendix A.1):

$$f(r, \theta, \varphi) = \sum_{l=0}^{\infty} \sum_{m=-l}^{l} \left(A_l^m r^l + B_l^m r^{-(l+1)} \right) P_l^m(cos(\theta)) e^{im\varphi} \tag{3.43}$$

Here $P_l^m(cos(\theta))$ is the associated Legendre functions of the first kind (Appendix A.2). For the axisymmetric droplet, only the case $m = 0$ remains. To exclude the singularity at the center of the droplet, the general solution inside the droplet is given as:

$$f = \sum_{l=0}^{\infty} A_l r^l P_l(cos\theta) \tag{3.44}$$

While boundedness at infinity limits the solution outside the droplet:

$$f = \sum_{l=0}^{\infty} B_l r^{-(l+1)} P_l(cos\theta) \tag{3.45}$$

3.6 Prolate/Spherical/Oblate Coordinate System and Generalized Spheroidal Coordinate System

For an oscillating droplet, the time-dependent deformation of the introduces a moving boundary in the governing equations. A convenient mathematical strategy consists in introducing curvilinear coordinate systems in which the droplet surface coincides with a coordinate surface [99]. In this way, the boundary conditions can be imposed on a fixed coordinate location, while the time dependence is transferred to the coordinate mapping.

Among orthogonal curvilinear coordinate systems, the prolate, spherical and oblate systems are particularly suitable, since their coordinate surfaces include spheroidal geometries. These systems can be described within a unified formulation by introducing a deformation parameter that determines whether the geometry is prolate, spherical or oblate, as illustrated in Figure 2 [42], which introduces a generalized spheroidal coordinate system (ψ, η, φ).

By allowing the deformation parameter to vary in time, the instantaneous droplet surface is represented as a coordinate iso-surface, which simplifies the solution of Laplace's equation and the imposition of interfacial conditions.

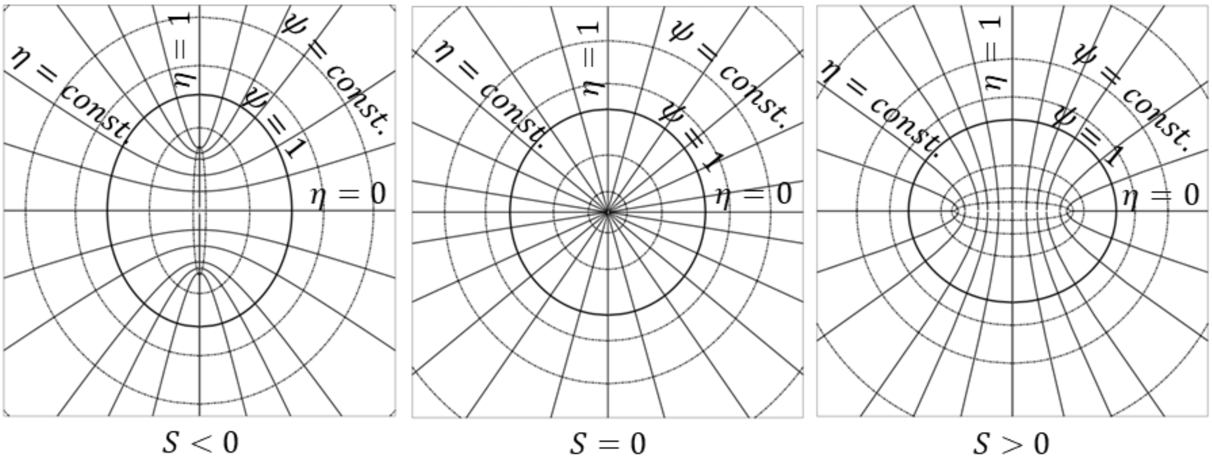

Figure 2: The generalized spheroidal coordinate system (ψ, η, φ): $S < 0$, prolate shape (left); $S = 0$, spherical shape (middle); $S > 0$, oblate shape (right).

3.6.1 Prolate Coordinate System

A prolate coordinate system (ζ, η, φ) is defined through [99, 113]:

$$
\begin{aligned}
x &= a_f\sqrt{\zeta^2-1}\sqrt{1-\eta^2}cos(\varphi)\\
y &= a_f\sqrt{\zeta^2-1}\sqrt{1-\eta^2}sin(\varphi)\\
z &= a_f\zeta\eta
\end{aligned}
\tag{3.46}
$$

where (ζ, η, φ) takes $\zeta \in [1, +\infty)$, $\eta \in [-1, 1]$, and $\varphi \in [0, 2\pi)$. Focus length a_f is the half-distance between the two focus point. The transformation is invertible within the admissible coordinate ranges. In particular, $\varphi = arctan(\frac{y}{x})$, while ζ and η follow uniquely from the defining relations above. Sometimes η is written as $cos(\theta)$ (note that here θ is the spheroidal angle in a spheroidal coordinate system, distinguished from the polar angle θ in a spherical coordinate system). $\zeta = const.$ represents a prolate spheroid and $\eta = 1$ refers to a hyperboloid. Taking $\zeta = const.$ as a prolate ellipsoid, we have $a_r = a_f\sqrt{\zeta^2-1}$ and $a_z = a_f\zeta$. Therefore, $\frac{x^2+y^2}{a_r^2} + \frac{z^2}{a_z^2} = 1$ is satisfied. The volume-equivalent radius of this prolate ellipsoid is $R = \left(\frac{3Vol}{4\pi}\right)^{1/3} = a_f\frac{\varepsilon^{1/3}}{|1-\varepsilon^2|^{1/2}}$ (Vol is the volume). The scale factors $h_\zeta, h_\eta, h_\varphi$ and their product $g^{1/2}$ are:

$$
\begin{aligned}
&h_\zeta = a_f\frac{\sqrt{\zeta^2-\eta^2}}{\sqrt{\zeta^2-1}},\ h_\eta = a_f\frac{\sqrt{\zeta^2-\eta^2}}{\sqrt{1-\eta^2}}\\
&h_\varphi = a_f\sqrt{\zeta^2-1}\sqrt{1-\eta^2},\ g^{1/2} = h_\zeta h_\eta h_\varphi = a_f^3(\zeta^2-\eta^2)
\end{aligned}
\tag{3.47}
$$

The surface element of a prolate spheroid at $\zeta = const.$ is $dA = h_\eta h_\varphi d\eta d\varphi = a_f^2\sqrt{\zeta^2 - \eta^2}\sqrt{\zeta^2 - 1}d\eta d\varphi$.

3.6.2 Spherical Coordinate System

A spherical coordinate system (r, η, φ) is defined through [99, 113]:

$$
\begin{aligned}
x &= r\sqrt{1 - \eta^2}cos(\varphi) \\
y &= r\sqrt{1 - \eta^2}sin(\varphi) \\
z &= r\eta
\end{aligned}
\tag{3.48}
$$

where (r, η, ψ) takes $r \in [0, +\infty)$, $\eta \in [-1, 1]$, and $\varphi \in [0, 2\pi)$. $r = const.$ represents a sphere and $\eta = const.$ refers to a circular cone. The spheroidal angle $\theta_{spheroidal}$ in a spheroidal coordinate system and the polar angle $\theta_{spherical}$ in a spherical coordinate can be transformed by $cos(\theta_{spheroidal}) = \frac{1}{\sqrt{1+\varepsilon^2 tan^2(\theta_{spherical})}}$. The scale factors h_r, h_η, h_φ and their product $g^{1/2}$ are:

$$
h_r = 1,\ h_\eta = \frac{r}{\sqrt{1 - \eta^2}},\ h_\varphi = r\sqrt{1 - \eta^2},\ g^{1/2} = h_r h_\eta h_\varphi = r^2 \tag{3.49}
$$

The surface element of a sphere at $r = const.$ is $dA = h_\eta h_\varphi d\eta d\varphi = r^2 d\eta d\varphi$ ($= r^2 sin(\theta)d\theta d\varphi$ when writing η as $cos(\theta)$).

3.6.3 Oblate Coordinate System

Similar to a prolate coordinate system, an oblate coordinate system (ζ, η, φ) is defined through [99, 113]:

$$
\begin{aligned}
x &= a_f\sqrt{\zeta^2 + 1}\sqrt{1 - \eta^2}cos(\varphi) \\
y &= a_f\sqrt{\zeta^2 + 1}\sqrt{1 - \eta^2}sin(\varphi) \\
z &= a_f\zeta\eta
\end{aligned}
\tag{3.50}
$$

where (ζ, η, φ) takes $\zeta \in [0, +\infty)$, $\eta \in [-1, 1]$, and $\varphi \in [0, 2\pi)$. $\zeta = const.$ represents an oblate spheroid and $\eta = 1$ refers to a hyperboloid. a_f is also the focus length. Taking $\zeta = const.$ as an oblate ellipsoid, we have $a_r = a_f\sqrt{\zeta^2 + 1}$ and $a_z = a_f\zeta$. Therefore, $\frac{x^2+y^2}{a_r^2} + \frac{z^2}{a_z^2} = 1$ is also satisfied. The volume-equivalent radius of this oblate ellipsoid is $R = a_f\frac{\varepsilon^{1/3}}{|1-\varepsilon^2|^{1/2}}$, too. The scale factors $h_\zeta, h_\eta, h_\varphi$ and their products $g^{1/2}$ are:

$$
\begin{aligned}
&h_\zeta = a_f\frac{\sqrt{\zeta^2 + \eta^2}}{\sqrt{\zeta^2 + 1}},\ h_\eta = a_f\frac{\sqrt{\zeta^2 + \eta^2}}{\sqrt{1 - \eta^2}} \\
&h_\varphi = a_f\sqrt{\zeta^2 + 1}\sqrt{1 - \eta^2},\ g^{1/2} = h_\zeta h_\eta h_\varphi = a_f^3(\zeta^2 + \eta^2)
\end{aligned}
\tag{3.51}
$$

The surface element of an oblate spheroid at $\zeta = const.$ is $dA = h_\eta h_\varphi d\eta d\varphi = a_f^2\sqrt{\zeta^2 + \eta^2}\sqrt{\zeta^2 + 1}d\eta d\varphi$.

3.6.4 Generalized Spheroidal Coordinate System

The prolate and oblate coordinate systems have many similarities. The focal point of a prolate and oblate coordinate system is on the z-axis and r-axis, respectively. The spherical coordinate system can be regarded as a particular spheroidal coordinate system with the focus point at the origin. A generalized spherical coordinate system unifies a prolate/spherical/oblate coordinate system by a time-dependent deformation parameter $S(t)$, introduced in [42].

A generalized spheroidal coordinate system in [42] is defined as:

$$\begin{aligned} x &= \frac{R}{(1+S)^{1/3}}\sqrt{\phi^2+S}\sqrt{1-\eta^2}cos(\varphi) \\ y &= \frac{R}{(1+S)^{1/3}}\sqrt{\phi^2+S}\sqrt{1-\eta^2}sin(\varphi) \\ z &= \frac{R}{(1+S)^{1/3}}\phi\eta \end{aligned} \tag{3.52}$$

where (ϕ, η, ψ) takes $\phi \in [0, +\infty)$ for $S \geq 0$ and $\phi \in [|S|^{1/2}, +\infty)$ for $S < 0$, $\eta \in [-1, 1]$, and $\varphi \in [0, 2\pi)$. R is the volume-equivalent radius and $S \in (-1, +\infty)$ is the deformation parameter that is related to aspect ratio ε as $\varepsilon = \frac{\phi}{\sqrt{\phi^2+S}}$, as reports in Figure 3, which illustrates a prolate and oblate droplet of the semi-axes a_r and a_z in a cylindrical coordinate system. $S < 0$, $S = 0$, and $S > 0$ correspond to a prolate, spherical, and oblate coordinate system, respectively. By $S = 0$ and $r = R\phi$, the spherical coordinate system is recovered. By $\zeta^2 = \frac{\phi^2}{|S|}$ and $a_f = \frac{R}{(1+S)^{1/3}}|S|^{1/2}$, the prolate and oblate spheroidal coordinate systems are recovered.

$\phi = const.$ represents a spheroid (sphere as $S = 0$) and $\eta = const.$ refers to a hyperboloid (circular cone as $S = 0$). Taking $\phi = const.$ as a spheroid, of which the semi-axis is $a_r = \frac{R}{(1+S)^{1/3}}\sqrt{\phi^2+S}$ and $a_z = \frac{R}{(1+S)^{1/3}}\phi$. Its volume is $Vol = \frac{4}{3}\pi a_r^2 a_z = \frac{4}{3}\pi R^3 \frac{(\phi^2+S)\phi}{(1+S)}$.

In the analytical modelling framework of this thesis, the droplet surface is represented as a coordinate iso-surface $\phi = const.$. The volume of the spheroid at $\phi = 1$ is $Vol = \frac{4}{3}\pi R^3$, independent of S (the spheroidal shape). Therefore, in the generalized spheroidal coordinate system, $\phi = 1$ represents the surface of an oscillating spheroidal droplet. For an oscillating droplet, R is constant, while for an evaporating droplet, the volume-equivalent radius R varies in time. At the droplet surface $\phi = 1$, the aspect ratio $\varepsilon = \frac{a_z}{a_r} = \frac{1}{\sqrt{1+S}}$. And the deformation parameter S is $\frac{1-\varepsilon^2}{\varepsilon^2}$. As the droplet oscillates, the deformation parameter $S(t)$ is time-varying, and the droplet oscillation can be completely described by $S(t)$ [42].

$\phi \in [|S|^{1/2}, 1]$ for $S < 0$ and $\phi \in [0, 1]$ for $S \geq 0$ refers to the liquid phase, and $\phi \in (1, +\infty)$ represents the gaseous phase. The generalized spheroidal coordinate system constructed in this way brings great convenience to the problem of an oscillating droplet, whose surface is represented by a spheroidal

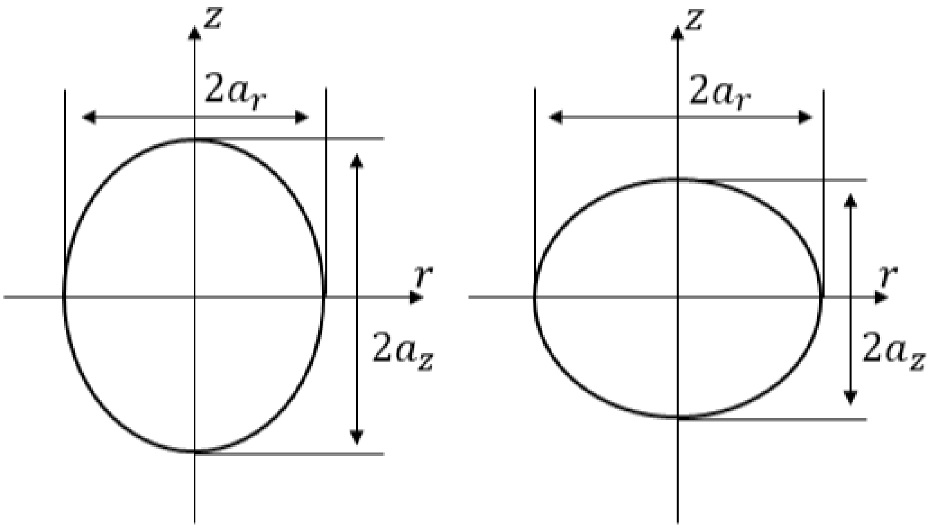

Figure 3: A prolate (left) and oblate (right) droplet of semi-axes a_r and a_z

shape. One of the challenges in handling an oscillating droplet is the moving boundary problem, the location of the interface is time-varying in a time-fixed coordinate system, and the coordinates of the interface must be evaluated at each moment. But in this time-varying generalized spheroidal coordinate system, which is described by a time-varying deformation parameter S, the interface is located at the time-independent coordinate surface $\phi = 1$. The time-varying deformation parameter $S(t)$ and constant equivalent radius R refer to an oscillating droplet without evaporation, which is discussed in Section 4.1. The constant deformation parameter S and time-varying equivalent radius $R(t)$ correspond to a shrinking or expanding droplet of the same shape. As for both time-varying deformation parameter $S(t)$ and equivalent radius $R(t)$, an oscillating and evaporating droplet is represented, which is adopted in Section 5.1.

The oscillating droplet shape is given by the time-varying deformation parameter $S = \frac{1-\varepsilon^2}{\varepsilon^2}$. The deformation parameter S is evaluated by numerically solving the second-order nonlinear ordinary differential energy equation [42] (see Section 4.1):

$$S_{tt} - \frac{7}{6}\Omega_1(S)S_t^2 + \frac{5\sqrt{2}}{2}\omega_2 Oh\Omega_2(S)S_t + \omega_2^2\Omega_3(S)S = 0 \tag{3.53}$$

here S_{tt} represents the second order derivative of S with respect to time t, and Oh is the Ohnesorge number. ω_2 is the oscillation frequency in the second mode by normal mode analysis (refer to Section 3.7). $\Omega_1(S), \Omega_2(S)$ and $\Omega_3(S)$ are coefficients dependent of droplet shape S, viscosity ratio $\frac{\mu_G}{\mu_L}$ and density ratio $\frac{\rho_G}{\rho_L}$.

The scale factors $h_\phi, h_\eta, h_\varphi$ and their product $g^{1/2}$ in this generalized spheroidal coordinate system are (refer to Appendix A.3):

$$
\begin{aligned}
h_\phi &= \frac{R}{(1+S)^{1/3}}\frac{\sqrt{\phi^2+S\eta^2}}{\sqrt{\phi^2+S}},\ h_\eta = \frac{R}{(1+S)^{1/3}}\frac{\sqrt{\phi^2+S\eta^2}}{\sqrt{1-\eta^2}} \\
h_\varphi &= \frac{R}{(1+S)^{1/3}}\sqrt{\phi^2+S}\sqrt{1-\eta^2},\ g^{1/2} = h_\phi h_\eta h_\varphi = \frac{R^3}{(1+S)}(\phi^2+S\eta^2)
\end{aligned} \tag{3.54}
$$

The surface element of the spheroid at $\phi = 1$ is:

$$
\begin{aligned}
dA &= h_\eta h_\varphi d\eta d\varphi = \frac{R^2}{(1+S)^{2/3}}\sqrt{\phi^2+S\eta^2}\sqrt{\phi^2+S}d\eta d\varphi \\
&\overset{\phi=1}{=} \frac{R^2}{(1+S)^{2/3}}\sqrt{1+S\eta^2}\sqrt{1+S}d\eta d\varphi
\end{aligned} \tag{3.55}
$$

The surface area of this spheroid is evaluated by:

$$
\begin{aligned}
A_{spheroid} &= \int_{\partial\Omega} dA = \int_0^{2\pi}\int_{-1}^{1}\frac{R^2}{(1+S)^{2/3}}\sqrt{1+S\eta^2}\sqrt{1+S}d\eta d\varphi \\
&= 2\pi\frac{R^2}{(1+S)^{1/6}}\frac{2}{\sqrt{S}}\left(\frac{\sqrt{1+S\eta^2}\sqrt{S\eta^2}}{2}+\frac{ln|\sqrt{1+S\eta^2}+\sqrt{S\eta^2}|}{2}\right)\Bigg|_0^{\eta=1} \\
&= 2\pi\frac{R^2}{(1+S)^{1/6}}\left(\sqrt{1+S}+\frac{atanh(\frac{\sqrt{S}}{\sqrt{1+S}})}{\sqrt{S}}\right)
\end{aligned} \tag{3.56}
$$

This is available for all the shapes, whether $S < 0$, $S = 0$ or $S > 0$ (refer to Appendix A.4).

In the following discussions, $\phi = 1$ represents the droplet interface and R refers to the equivalent radius. If the gaseous phase ($\phi \in (1, +\infty)$) is investigated, it could be more convenient to transform $\psi = \frac{1}{\phi}$ to make the computational domain finite ($\psi \in (0, 1)$), where $\psi = 0$ corresponds to infinity and $\psi = 1$ refers to the interface. Then the coordinate system for the gas phase is:

$$
\begin{aligned}
x &= \frac{R}{(1+S)^{1/3}}\frac{\sqrt{1+S\psi^2}}{\psi}\sqrt{1-\eta^2}cos(\varphi) \\
y &= \frac{R}{(1+S)^{1/3}}\frac{\sqrt{1+S\psi^2}}{\psi}\sqrt{1-\eta^2}sin(\varphi) \\
z &= \frac{R}{(1+S)^{1/3}}\frac{1}{\psi}\eta
\end{aligned} \tag{3.57}
$$

with the scale factors $h_\psi, h_\eta, h_\varphi$ and their product $g^{1/2}$ (Appendix A.3):

$$
\begin{aligned}
h_\psi &= \frac{R}{(1+S)^{1/3}}\frac{\sqrt{1+S\eta^2\psi^2}}{\psi^2\sqrt{1+S}},\ h_\eta = \frac{R}{(1+S)^{1/3}}\frac{\sqrt{1+S\eta^2\psi^2}}{\psi\sqrt{1-\eta^2}} \\
h_\varphi &= \frac{R}{(1+S)^{1/3}}\frac{\sqrt{1+S\psi^2}\sqrt{1-\eta^2}}{\psi},\ g^{1/2} = h_\psi h_\eta h_\varphi = \frac{R^3}{(1+S)}\frac{1+S\eta^2\psi^2}{\psi^4}
\end{aligned} \tag{3.58}
$$

Notice that the scale factors of (ψ, η, φ) cannot be obtained by substituting $\psi = \frac{1}{\phi}$ in the scale factors of (ϕ, η, φ) (Appendix A.3). Since φ is the azimuthal angle, the generalized spheroidal coordinate system in 2D reads:

$$\begin{aligned} r &= \frac{R}{(1+S)^{1/3}} \frac{\sqrt{1+S\psi^2}}{\psi} \sqrt{1-\eta^2} \\ z &= \frac{R}{(1+S)^{1/3}} \frac{1}{\psi} \eta \end{aligned} \tag{3.59}$$

with $r^2 = x^2 + y^2$. The interface velocity (at $\psi = 1$) V is evaluated by $V = (V_r, V_z) = \left(\frac{dr}{dt}\Big|_{\psi=1}, \frac{dz}{dt}\Big|_{\psi=1} \right)$. Then, the normal interface velocity V_n is derived (refer to Appendix A.5):

$$\begin{aligned} V_n &= V \cdot n = (V_r, V_z) \cdot \left(\sqrt{\frac{1-\eta^2}{1+S\eta^2}}, \frac{\eta\sqrt{1+S}}{\sqrt{1+S\eta^2}} \right) \\ &= \frac{(1-3\eta^2)R}{6\sqrt{1+S\eta^2}(1+S)^{5/6}} S_t + \frac{(1+S)^{1/6}}{\sqrt{1+S\eta^2}} R_t = V_{os} + V_{sh} \end{aligned} \tag{3.60}$$

where n is the unit normal vector of the interface with positive direction towards the gaseous phase. S_t and R_t are the time derivatives of S and R. The normal interface velocity consists of two parts, one is due to the droplet oscillation V_{os} and the other is due to the droplet evaporation/shrinking V_{sh}. For an oscillating droplet without evaporation, the latter part V_{sh} disappears. Recalling the mass jump condition Eqn. 3.21 and definition of the evaporation flux Eqn. 3.33, we obtain the boundary conditions for the liquid and gaseous phase $u_{G,n} = V_n = u_{L,n}$ for an oscillating droplet without evaporation, which will be used in the oscillation analysis.

3.7 Normal Mode Analysis of Droplet Oscillation

The instantaneous droplet interface can be described as a perturbation about a spherical reference configuration of the volume-equivalent radius R. In a spherical coordinate system, the interface position r_s can be written as [6, 9, 10, 114]:

$$r_s(\theta, \varphi, t) = R(1 + \xi(\theta, \varphi, t)) = R(1 + \sum_{l=0}^{\infty} \sum_{m=-l}^{l} C_l^m(t) P_l^m(cos(\theta)) e^{im\varphi}) \tag{3.61}$$

where ξ denotes the surface displacement from the undeformed sphere, P_l^m are the associated Legendre polynomials and C_l^m are time-dependent modal amplitudes. For axially symmetric configurations, the dependence on the azimuthal angle vanishes ($m = 0$), and the expansion reduces to

$$r_s(\theta, \varphi, t) = R(1 + \sum_{l=0}^{\infty} C_l(t) P_l(cos(\theta))) \tag{3.62}$$

The $l = 0$ mode corresponds to a uniform radial expansion/shrink, and the $l = 1$ represents a translation of the droplet. The first non-trivial shape deformation arises at mode $l = 2$. For inviscid linear surface-tension-driven oscillations, Rayleigh [5] showed that the natural frequency of the l^{th} mode is

$$\omega_l = \sqrt{\frac{l(l-1)(l+1)\sigma}{\rho R^3}} \tag{3.63}$$

In particular, the lowest non-trivial deformation mode $l = 2$ has the frequency $\omega_2 = \sqrt{\frac{8\sigma}{\rho R^3}}$. Because the mode $l = 2$ corresponds to the lowest-frequency deformation mode and higher mode experience rapid decays [9, 17], ω_2 is commonly adopted as a characteristic oscillation frequency in theoretical analysis and scaling arguments. The interface is approximated by retaining only the dominant mode $l = 2$ in many studies of droplet oscillations:

$$r_s = R(1 + C_2(t)P_2(cos(\theta))) \tag{3.64}$$

This representation corresponds to the classical spherical harmonic expansion truncated at mode $l = 2$, which represents the first order deformation of the small disturbance. In the present analytical framework, the droplet is instead assumed to maintain a spheroidal shape with semi-axes a_r and a_z. A spheroidal surface can also be expanded in Legendre polynomials:

$$r_s(\theta) = R(1 + \sum_{l=0}^{\infty} C_l(\varepsilon)P_l(cos(\theta))) \tag{3.65}$$

Due to axial symmetry and reflection symmetry about the equatorial plane, only even-order modes are present in this expansion. A spheroidal shape satisfies 2D form $\frac{r^2(1-\eta^2)}{a_r^2} + \frac{r^2\eta^2}{a_z^2} = 1$ in the spherical coordinates (r, η) (η is the cosine of the polar angle), which satisfies the volume constraint $\frac{4\pi}{3}a_r^2 a_z = \frac{4\pi}{3}R^3$. The droplet surface r_s reads:

$$r_s(\eta) = \frac{R\varepsilon^{2/3}}{\sqrt{\eta^2 + \varepsilon^2(1-\eta^2)}} \tag{3.66}$$

Then, the displacement from the undisturbed surface is $R\xi(\eta) = \frac{R\varepsilon^{2/3}}{\sqrt{\eta^2+\varepsilon^2(1-\eta^2)}} - R$. When the droplet radius is expanded as $r_s = R(1 + \sum_{l=0}^{\infty} C_l P_l(\eta))$, the coefficients can be evaluated as (Appendix A.2):

$$C_l = \frac{2l+1}{2}\int_{-1}^{1} \xi(\eta)P_l(\eta)d\eta \tag{3.67}$$

The first few coefficients are shown in Figure 4, with respect to ε. As the droplet oscillates, the aspect ratio varies with time. Thus, the coefficients are also time-dependent. For a spherical shape $\varepsilon = 1$, all

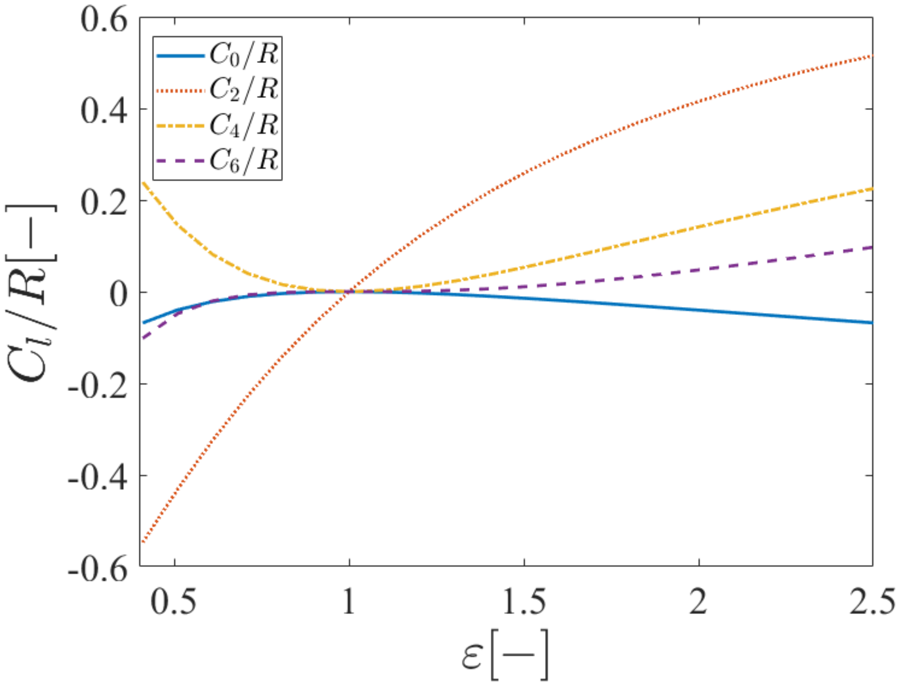

Figure 4: Coefficients C_0, C_2, C_4, C_6 with respect to aspect ratio ε.

coefficients are zero. The droplet shape, which is truncated in different modes $l = 2$, $l = 4$ and $l = 6$, can be referred in Appendix A.2.

Figure 5 compares the droplet shape in mode $l = 2$ and the spheroidal droplet shape with the same volume and aspect ratio ε. For small and medium droplet deformations, both shapes agree well. As the oscillation amplitude increases, the difference between two shapes becomes larger, since the droplet shape in mode $l = 2$.

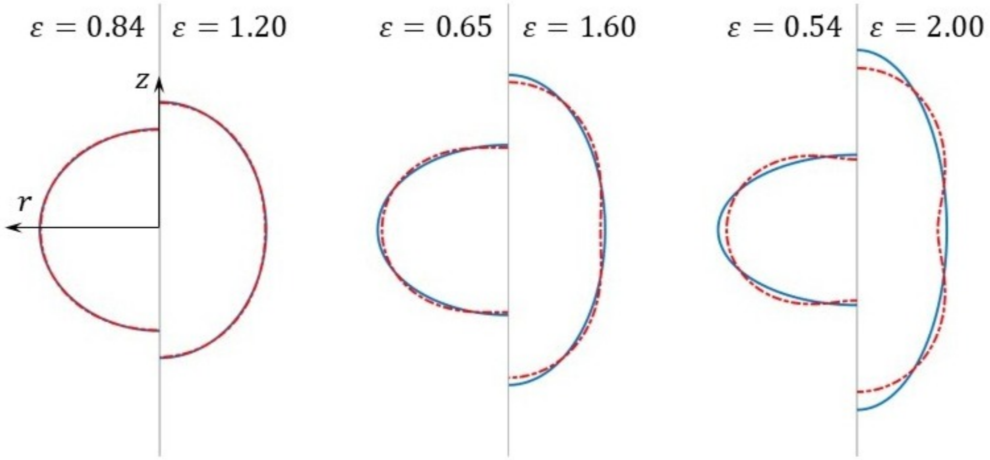

Figure 5: The spheroidal droplet shape (blue line) and the droplet shape given by the mode $l = 2$ (red line) with the same volume and aspect ratio, for varied deformations.

For an oscillating spheroidal droplet with small aspect ratio $\varepsilon = 1 + \epsilon$ ($|\epsilon| << 1$) and $S = \frac{1-\varepsilon^2}{\varepsilon^2}$, we have:

$$S = \frac{1-\varepsilon^2}{\varepsilon^2} \approx -2\epsilon \tag{3.68}$$

Then, a spheroidal surface can be expanded by Eqn. 3.65 and 3.67:

$$r_s = R(1 + C_0 + C_2 P_2(\eta) + O(\epsilon^2)) \tag{3.69}$$

with

$$C_0 = -\frac{S^2}{45} + O(\epsilon^3) = O(\epsilon^2), \quad C_2 = -\frac{S}{3} + O(\epsilon^2) = O(\epsilon) \tag{3.70}$$

For small amplitude oscillation $C_2 = O(\epsilon)$, the classical representation truncated in mode $l = 2$ by Eqn. 3.64 is expressed as:

$$r_s = R(1 + C_0 + C_2 P_2(\eta)) \tag{3.71}$$

Here C_0 represents the radius correction for the volume conservation, and we have $C_2 = O(\epsilon)$ and $C_0 = -\frac{1}{5}C_2^2$. This expression matches the expansion of the spheroidal shape. Therefore, in the limit of small deformations, the spheroidal shape is consistent with the classical spherical harmonic representation truncated in mode $l = 2$ in the first order of small disturbance. The spheroidal shape has only one degree of the freedom, it can be completely determined by one deformation parameter. The coefficients of its expansion in spherical harmonic are not independent. However, the coefficients by the classical representation are independent geometric degrees of freedom, whose evolution is coupled through the kinematic/dynamic conditions as well as the volume constraints. In the presence of viscosity, the higher modes decay rapidly. As a result, the droplet shape is typically dominated by the second mode, and the spheroidal approximation provides a good representation of the moving interface and great convenience in calculation.

In the present analytical modelling framework, the droplet is assumed to maintain a spheroidal shape. This assumption is introduced as a geometric constraint that enables separation of variables of the Laplace equation in the generalized spheroidal coordinate system, rather than as a modal truncation of the classical spherical harmonic expansion (such as the mode $l = 2$ representation). As a consequence, the moving boundary problem is reformulated as a problem with a fixed coordinate surface, while the time dependence of the droplet shape is described by a single time-dependent deformation parameter.

3.8 Modelling Hierarchy and Scope

The governing equations and interfacial conditions presented in this chapter constitute the complete continuum description of a deforming and evaporating droplet in a gaseous environment. This formulation includes the Navier–Stokes equations in both phases, species transport in the gas phase, and the thermal energy equation, coupled through appropriate jump conditions at the moving interface. In the subsequent sections, two complementary modelling approaches are adopted, both rooted in the general framework introduced above but operating at different levels of physical description.

First, a reduced analytical model is developed in Section 4.1 and Section 5.1. In this framework, the oscillatory flow field is represented using a potential-flow approximation, based on the assumption that the droplet maintains a spheroidal shape. Viscous effects are not resolved through the full Navier–Stokes equations but are incorporated phenomenologically through damping terms in the deformation parameters. Evaporation is described by a convection–diffusion equation in the gas phase, accounting for the influence of droplet shape oscillations on the local mass transfer. The thermal energy equation is not solved within this reduced model, and physical properties are assumed constant. Consequently, thermal coupling effects and temperature-dependent material properties are not explicitly considered.

Second, direct numerical simulations are presented in Section 4.2 and 5.2, where the full two-phase Navier–Stokes equations are solved together with species and energy transport equations using the FS3D solver. In this framework, viscous stresses and temperature fields are resolved without the simplifying assumptions adopted in the reduced analytical model.

The analytical and DNS approaches therefore represent different modelling fidelities. The reduced model provides a simplified and physically interpretable description of evaporation from an oscillating droplet, whereas the DNS offers a more complete resolution of the coupled hydrodynamic and thermal transport processes. Comparisons between the two approaches must therefore be interpreted in light of their respective assumptions and scope.

3.9 Numerical Tools

The analytical modelling framework is based on specific assumptions, such as potential flows and spheroidal geometry. To explore the physical implications of these assumptions and to provide complementary insight into the flow and mass transfer mechanisms, numerical simulations are performed. An in-house code, Free Surface 3D (FS3D), offered by the ITLR of the University of Stuttgart, will be used for the study of the evaporation of an oscillating droplet (summarized in Section 5.2) and as a comparison to the analytical oscillation model (in Section 4.2). What follows is a short introduction to the numerical tool FS3D.

FS3D, originally developed by Rieber [115], can simulate incompressible multiphase flows, including sharp interfaces between the immiscible phases [116]. It solves the incompressible Navier-Stokes equations, consisting of the mass and momentum conservation equations, as well as the energy equation for phase transition. The interface is reconstructed based on the Volume of Fluid method (VOF) [117] and the piecewise linear interface calculation (PLIC) method [118]. To discretize the incompressible Navier-Stokes equations in space, the finite volume method is applied. Employing the Marker and Cell (MAC) method [21], scalars (like densities) are stored at the cell centers, while vectors (like velocities) are stored on the cell faces. Without any turbulent model, FS3D can resolve the smallest temporal and spatial scales by DNS. As a price, it requires great computational efforts, which are solved by using OpenMP and MPI (Message Passing Interface). FS3D takes into account the complicated processes like moving interface, phase transition and turbulent flows. Multiphase flow phenomena can be simulated by FS3D, such as droplet oscillation, splash, collision and evaporation [74, 82, 109, 119–121].

The incompressible conservation equations in a one-field form are solved, and the different phases and species are regarded as a single fluid with variable material properties that may jump discontinuously across the interface. Slightly different from the momentum Eqn. 3.14 and energy Eqn. 3.16 described in Section 3.2, the conservation equations read:

$$\begin{aligned}
&\frac{\partial \rho}{\partial t} + \nabla \cdot (\rho u) = 0 \\
&\frac{\partial \rho u}{\partial t} + \nabla \cdot (\rho u u) = \rho g - \nabla P + \nabla \cdot S + f_\sigma \\
&\frac{\partial \rho c_p T}{\partial t} + \nabla \cdot (\rho c_p u T) = \nabla \cdot (\lambda \nabla T) + \dot{q}'''
\end{aligned} \tag{3.72}$$

g is the gravitational acceleration as the source term. f_σ models the surface tension in the vicinity of the interface. $\dot{q}'''$ refers to an additional source term due to the phase change at the interface, instead of using the energy jump condition. For small Eckert numbers and incompressible flows, the viscous heating term and pressure work term are neglected.

According to the VOF method, an additional indicator variable is applied to distinguish different phases. For a droplet in a gaseous phase, this variable f_L represents the volume fraction of the fluid in a cell:

$$f_L = \begin{cases} 0, & in\ the\ continuous\ (gaseous)\ phase \\ (0,1), & in\ the\ interfacial\ cells \\ 1, & in\ the\ dispersed\ (liquid)\ phase \end{cases} \tag{3.73}$$

and f_v refers to the volume fraction of the vapour to discern the vapour and ambient gas. The local material properties can be expressed in a one-field form, which may jump through the interface, e.g.

the density ρ reads:

$$\rho = \rho_L f_L + \rho_G^v f_v + \rho_G^a (1 - f_L - f_v) \tag{3.74}$$

The temperature dependence of material properties is also considered. As a consequence of the VOF method, additional transport equations for the VOF variables are solved:

$$\begin{aligned} &\frac{\partial f_L}{\partial t} + \nabla \cdot (f_L u_L) = -\frac{\dot{m}'''}{\rho_L} \\ &\frac{\partial f_v}{\partial t} + \nabla \cdot (f_v u_G) = \nabla (D^v \nabla f_v) + \frac{\dot{m}'''}{\rho_G^v} \end{aligned} \tag{3.75}$$

for the liquid and gaseous phase, respectively. $\dot{m}'''$ denotes the volumetric mass source due to the phase change, which is determined from the evaporation flux [74]. The evaporation flux is also evaluated from the vapour mass fraction by Eqn. 3.34 [108, 109]. The vapour mass fraction χ^v reads:

$$\chi^v = \frac{f_v \rho_G^v}{(1 - f_L)\rho_G}, \; \rho_G = \frac{\rho_G^v f_v + \rho_G^a (1 - f_L - f_v)}{1 - f_L} \tag{3.76}$$

More detailed descriptions about FS3D can be found in [109, 115]. The analytical formulation allows the identification of dominant mechanisms under clearly stated assumptions, while minor factors can be ignored temporarily. For the coupled partial differential equations, it is difficult to obtain analytical solutions. A commercial software, COMSOL Multiphysics, helps to solve the coupled partial differential equations in an evaporation model for an oscillating droplet (summarized in Section 5.1).

Distinguished from FS3D, COMSOL Multiphysics is a commercial numerical solver and simulation software package for various physics and engineering applications, based on the finite element method. It includes many physical models, such as electric, acoustics, chemical species transport, fluid flow, heat transfer and structural mechanics. However, we mainly take advantage of COMSOL Multiphysics as a numerical solver for the coupled partial differential equations, described in Section 5.1. No physics models or packages are applied in our work described in Section 5. The additional package, LiveLink for MATLAB, provides an interface between COMSOL Multiphysics and MATLAB based on the COMSOL client-server architecture. Via this package, we can set up the computational loops and perform post-processing in MATLAB.

Chapter 4. Droplet Oscillation

In the previous chapter, the governing equations and interfacial conditions for two-phase system were introduced. In addition, a generalized spheroidal coordinate system was presented.

In the present chapter, the oscillatory motion of the droplet is analysed in the absence of the evaporation. An analytical oscillation model is first introduced [42]. Based on the assumption that the droplet maintains a spheroidal shape, the droplet deformation is represented by the deformation parameter $S(t)$. This assumption enables the analytical solution of Laplace equation in the generalized spheroidal coordinate system. Under the assumption of potential flow, the flow field in both phases are constructed. Through the energy equation between the total energy and viscous dissipation, an ODE for the deformation parameter is derived. This analytical oscillation mode will be integrated with droplet evaporation in Section 5.1 to propose an evaporation model for an oscillating droplet. The in-house FS3D code is employed to perform direct numerical simulations. The numerical results are compared with the analytical solutions, which is under the assumption of potential flow.

4.1 Analytical Model for an Oscillating Droplet under the Assumption of a potential flow

In order to describe the droplet oscillation, an analytical model is constructed under two main assumptions. First, the flow in both phases is assumed to be potential, so that the velocity field can be represented by a velocity potential satisfying Laplace equation. Second, the droplet interface is assumed to maintain a spheroidal shape during the oscillation. Then, the moving boundary problem can be reformulated into a fixed boundary problem in a time-dependent generalized spheroidal coordinate system, in which the solution of Laplace equation is much simplified. The Laplace equation of velocity potential in both phases reads:

$$\nabla^2 \Phi_{G,L} = 0 \tag{4.1}$$

again with Φ as the velocity potential and subscripts G, L representing the gaseous and the liquid phase, respectively. Due to the symmetry of the droplet and uniform boundary conditions, Φ is symmetrical about $\eta = 0$ in the interval $\eta \in [-1, 1]$. The gaseous phase is described by $\psi \in [0, 1)$, and the liquid phase by $\psi \in [1, +\infty)$ for $S \geq 0$ and $\psi \in [1, |S|^{-1/2}]$ for $S < 0$.

The initial condition for both is set as $\Phi_{G,L} = 0$, so the initial velocity field is zero. The boundary conditions for both phases are imposed. At the interface, due to the absence of evaporation, the normal velocity within the two phases is continuous. Referring to Appendix A.5, the part due to the evaporation disappears, and the normal interface velocity V_n reads:

$$V_n = \frac{(1-3\eta^2)R}{6\sqrt{1+S\eta^2}(1+S)^{5/6}}S_t \tag{4.2}$$

and at the interface $\psi = 1$, it is satisfied that $u_{G,n} = V_n = u_{L.n}$:

$$\begin{aligned} -\frac{1}{h_\psi}\frac{\partial \Phi_G}{\partial \psi}\bigg|_{\psi=1} &= V_n \\ -\frac{1}{h_\psi}\frac{\partial \Phi_L}{\partial \psi}\bigg|_{\psi=1} &= V_n \end{aligned} \tag{4.3}$$

The minus sign is due to the coordinate ψ and normal interface velocity having opposite directions. In the following, the minus sign in the velocity as the gradient of the potential is in default in this generalized spheroidal coordinate system (ψ, η, φ). At infinity from the droplet $\psi = 0$, Φ_G remains unchanged:

$$\Phi_G|_{\psi=0} = 0 \tag{4.4}$$

At the droplet center $\psi \longrightarrow +\infty$ for $S \geq 0$ and $\psi = |S|^{-1/2}$ for $S < 0$, the velocity is zero:

$$\begin{aligned} \frac{1}{h_\psi}\frac{\partial \Phi_G}{\partial \psi}\bigg|_{\psi\longrightarrow+\infty} &= 0, \qquad && S \geq 0 \\ \frac{1}{h_\psi}\frac{\partial \Phi_G}{\partial \psi}\bigg|_{\psi=|S|^{-1/2}} &= 0, \qquad && S < 0 \end{aligned} \tag{4.5}$$

With the initial and boundary conditions described above, the Laplace equation will be solved in the following to obtain the distribution of the velocity potential $\Phi_{G,L}$. The velocity field is then derived:

$$u_{G,L} = -\nabla\Phi_{G,L} \tag{4.6}$$

Here, the minus sign appears due to the same reason as above.

4.1.1 Analytical Solutions of the Velocity Fields in both Phases

In the generalized coordinate system (ψ, η, φ), the Laplace equation $\nabla^2\Phi = 0$ reads:

$$\frac{1}{g^{1/2}}\left[\frac{\partial}{\partial\psi}\left(\frac{g^{1/2}}{h_\psi^2}\frac{\partial\Phi}{\partial\psi}\right) + \frac{\partial}{\partial\eta}\left(\frac{g^{1/2}}{h_\eta^2}\frac{\partial\Phi}{\partial\eta}\right)\right] = 0 \tag{4.7}$$

Substituting the scale factors h_ψ, h_η and their product $g^{1/2}$, we have:

$$\begin{aligned} \frac{\partial}{\partial\psi}\left(\frac{R}{(1+S)^{1/3}}(1+S\psi^2)\frac{\partial\Phi}{\partial\psi}\right) + \frac{\partial}{\partial\eta}\left(\frac{R}{(1+S)^{1/3}}\frac{1}{\psi^2}(1-\eta^2)\frac{\partial\Phi}{\partial\eta}\right) &= 0 \\ 2S\psi\Phi_\psi + (1+S\psi^2)\Phi_{\psi\psi} + \frac{-2\eta}{\psi^2}\Phi_\eta + \frac{1-\eta^2}{\psi^2}\Phi_{\eta\eta} &= 0 \end{aligned} \tag{4.8}$$

Here the subsripts ψ, η represent the partial derivatives with respect to ψ, η. To construct the Legendre equation (refer to Appendix A.2), we set a new variable ψ^*:

$$\psi^* = \begin{cases} \dfrac{1}{\psi}, & S = 0 \\ \dfrac{1}{\psi\sqrt{-S}}, & S \neq 0 \end{cases} \tag{4.9}$$

Assuming the form of $\Phi(\psi, \eta) = F(\psi^*)G(\eta)$ and separating the variables, yields:

$$(1 - \eta^2)G_{\eta\eta} - 2\eta G_\eta + l(l+1)G = 0 \tag{4.10}$$

and

$$\begin{aligned} &-\psi^2 F_{\psi\psi} + l(l+1)F = 0, && S = 0 \\ &(1 - \psi^{*2})F_{\psi^*\psi^*} - 2\psi^* F_{\psi^*} + l(l+1)F = 0, && S \neq 0 \end{aligned} \tag{4.11}$$

with non-negative integer l (see below). Therefore, F and G have the solution of the form:

$$G_l(\eta) = c_{l,1}P_l(\eta) + c_{l,2}Q_l(\eta) \tag{4.12}$$

and

$$F_l(\psi^*) = \begin{cases} c_{l,1}\psi^{*l} + c_{l,2}\psi^{*-l-1}, & S = 0 \\ c_{l,1}P_l(\psi^*) + c_{l,2}Q_l(\psi^*), & S \neq 0 \end{cases} \tag{4.13}$$

to note that here $c_{l,1}$ and $c_{l,2}$ in different equations represent coefficients in each term and are not the same, for the sake of simplicity. The coefficients are discussed in the following. Due to $\eta \in [-1, 1]$, so $P_l(\eta)$ and $Q_l(\eta)$ of $G(\eta)$ are Legendre functions $P_l(x)$ and $Q_l(x)$ of a real variable. The domain of variable ψ^* reads:

$$\psi^* = \begin{cases} \dfrac{1}{\psi} \in (1, +\infty), & S = 0 \\ \dfrac{1}{\psi\sqrt{-S}} \in (1, +\infty)\dfrac{1}{\sqrt{-S}}, & S < 0 \\ \dfrac{1}{\psi\sqrt{-S}} \in (1, +\infty)\dfrac{1}{\sqrt{-S}}, & S > 0 \end{cases} \tag{4.14}$$

in the gaseous phase, and

$$\psi^* = \begin{cases} \dfrac{1}{\psi} \in [0, 1], & S = 0 \\ \dfrac{1}{\psi\sqrt{-S}} \in |S|^{1/2}, 1]\dfrac{1}{\sqrt{-S}}, & S < 0 \\ \dfrac{1}{\psi\sqrt{-S}} \in [0, 1]\dfrac{1}{\sqrt{-S}}, & S > 0 \end{cases} \tag{4.15}$$

in the liquid phase. Since the domain of variable ψ^* for $S \neq 0$ is not limited inside $(-1, 1)$, $P_l(\psi^*)$ and $Q_l(\psi^*)$ of $F(\psi^*)$ are therefore the Legendre functions $P_l(z)$ and $Q_l(z)$, of which the complex variable domain are $|arg(z+1) < \pi|$ and $|arg(z-1) < \pi|$ [111, 122], respectively (refer to Appendix A.2). Before solving for the coefficient in each term, we can simplify the expression of $F(\psi^*)$ and $G(\eta)$ first. Starting with $G(\eta)$, at the poles $\eta = \pm 1$, $Q_l(\eta)$ is singular. Thus, $c_{l,2} = 0$, $G_l(\eta) = c_{l,1} P_l(\eta)$. In fact, the Legendre functions of the first kind of non-integral degree are also unbounded in the interval $[-1, 1]$. To obtain a non-trivial solution, the degree has to be an integer value. Due to the symmetry about $\eta = 0$, it is satisfied that $G(\eta) = G(-\eta)$. For l = odd, $P_l(\eta)$ is odd, and l = even, $P_l(\eta)$ is even. Therefore, l is even, written as $2k$ and $G(\eta)$ has the form (Appendix A.2):

$$G(\eta) = \sum_{k=0}^{+\infty} c_{2k} P_{2k}(\eta) \tag{4.16}$$

with non-negative integer $k = 0, 1, 2, 3...$ for both liquid and gaseous phases.

For $F(\psi^*)$, it is more complex and discussed for different S and in both phases. For a spherical shape $S = 0$, $F(\psi^*)$ is a polynomial. For the liquid phase, ψ^{*-2k-1} is singular at $\psi^* = 0$ (droplet center), therefore $c_{2k,2} = 0$. While for the gaseous phase, ψ^{*2k} diverges as $\psi^* \longrightarrow +\infty$ (infinity), $c_{2k,1} = 0$.

For a prolate shape $S < 0$, in the liquid phase, $Q_{2k}(\psi^*)$ is singular at $\psi^* = 1$ (droplet center), so $c_{2k,2} = 0$. In the gaseous phase, $P_{2k}(\psi^*)$ diverges as $\psi^* \longrightarrow +\infty$ (infinity), so $c_{2k,1} = 0$.

For an oblate shape $S > 0$, in the liquid phase, $\frac{\partial F(\psi^*)}{\partial \psi^*} = c_{2k,1}\frac{\partial P_{2k}(\psi^*)}{\partial \psi^*} + c_{2k,2}\frac{\partial Q_{2k}(\psi^*)}{\partial \psi^*} = 0$ at $\psi^* = 0$ (droplet center) is required. $\left.\frac{\partial P_{2k}(\psi^*)}{\partial \psi^*}\right|_{\psi^*=0} = 0$ ($P_{2k}(\psi^*)$ is even) and $\left.\frac{\partial Q_{2k}(\psi^*)}{\partial \psi^*}\right|_{\psi^*=0} \neq 0$, so $c_{2k,2} = 0$ is obtained. In the gaseous phase, $P_{2k}(\psi^*)$ diverges as $\psi^* \longrightarrow +\infty$ (infinity), so $c_{2k,1} = 0$.

In conclusion, the velocity potential $\Phi_{G,L}$ has the form:

$$\Phi_G = \sum_{k=0}^{\infty} \begin{cases} c_{2k}\psi^{*-2k-1} P_{2k}(\eta), & S = 0, \psi^* = \dfrac{1}{\psi} \in (1, +\infty) \\ c_{2k} Q_{2k}(\psi^*) P_{2k}(\eta), & S > 0, \psi^* = \dfrac{1}{\psi\sqrt{-S}} \in (1, +\infty) \cdot \dfrac{1}{\sqrt{-S}} \\ c_{2k} Q_{2k}(\psi^*) P_{2k}(\eta), & S < 0, \psi^* = \dfrac{1}{\psi\sqrt{-S}} \in (1, +\infty) \cdot \dfrac{1}{\sqrt{-S}} \end{cases} \tag{4.17}$$

$$\Phi_L = \sum_{k=0}^{\infty} \begin{cases} c_{2k}\psi^{*2k} P_{2k}(\eta), & S = 0, \psi^* = \dfrac{1}{\psi} \in [0, 1] \\ c_{2k} P_{2k}(\psi^*) P_{2k}(\eta), & S > 0, \psi^* = \dfrac{1}{\psi\sqrt{-S}} \in [0, 1] \cdot \dfrac{1}{\sqrt{-S}} \\ c_{2k} P_{2k}(\psi^*) P_{2k}(\eta), & S < 0, \psi^* = \dfrac{1}{\psi\sqrt{-S}} \in [|S|^{1/2}, 1] \cdot \dfrac{1}{\sqrt{-S}} \end{cases} \tag{4.18}$$

Due to the identical normal component of the gas $u_{G,n}$ and liquid $u_{L,n}$ velocity at the interface and the normal interface velocity V_n, the coefficient of each term in $\Phi_{G,L}$ can be derived. Substituting Eqn.

4.2 in Eqn. 4.3, yields:

$$\frac{\partial \Phi_G}{\partial \psi} = \frac{\partial \Phi_L}{\partial \psi} = \frac{R^2 P_2(\eta) S_t}{3(1+S)^{5/3}} \tag{4.19}$$

By comparing the term of $P_{2k}(\eta)$, k can only take the value of 1. The coefficient in each term is then derived:

$$\Phi_G = \begin{cases} \dfrac{R^2 S_t}{9(1+S)^{5/3}} \psi^3 P_2(\eta), & S = 0 \\ \dfrac{-\sqrt{-S} R^2 S_t}{3(1+S)^{5/3}} \dfrac{Q_2(\frac{1}{\psi\sqrt{-S}})}{Q_2'(\frac{1}{\sqrt{-S}})} P_2(\eta), & S \neq 0 \end{cases} \tag{4.20}$$

$$\Phi_L = \begin{cases} \dfrac{-R^2 S_t}{6(1+S)^{5/3}} \dfrac{1}{\psi^2} P_2(\eta), & S = 0 \\ \dfrac{-\sqrt{-S} R^2 S_t}{3(1+S)^{5/3}} \dfrac{P_2(\frac{1}{\psi\sqrt{-S}})}{P_2'(\frac{1}{\sqrt{-S}})} P_2(\eta), & S \neq 0 \end{cases} \tag{4.21}$$

The velocity in both phases is then obtained, in the gaseous phase $u_G = (u_{G,\psi}, u_{G,\eta})$ reads:

$$u_{G,\psi} = -\frac{1}{h_\psi} \frac{\partial \Phi_G}{\partial \psi} = \frac{-R S_t}{3(1+S)^{4/3}} \frac{\sqrt{1+S\psi^2}}{\sqrt{1+S\psi^2\eta^2}} J(\psi, S) P_2(\eta) \tag{4.22}$$

with $J(\psi, S)$ defined as (refer to Appendix A.6):

$$J(\psi, S) = \begin{cases} \psi^4, \quad S = 0 \\ \dfrac{Q_2'(\frac{1}{\psi\sqrt{-S}})}{Q_2'(\frac{1}{\sqrt{-S}})} = \begin{cases} \dfrac{\frac{3}{\psi\sqrt{-S}} 2atanh(\psi\sqrt{-S}) - \frac{3+S\psi^2}{1+S\psi^2} - 3}{\frac{3}{\sqrt{-S}} 2atanh(\sqrt{-S}) - \frac{3+S}{1+S} - 3}, & S < 0 \\ \dfrac{\frac{3}{\psi\sqrt{S}} 2arctan(\psi\sqrt{S}) - \frac{3+S\psi^2}{1+S\psi^2} - 3}{\frac{3}{\sqrt{S}} 2arctan(\sqrt{S}) - \frac{3+S}{1+S} - 3}, & S > 0 \end{cases} \end{cases} \tag{4.23}$$

and

$$u_{G,\eta} = -\frac{1}{h_\eta} \frac{\partial \Phi_G}{\partial \eta} = \frac{R S_t}{3(1+S)^{4/3}} \frac{\sqrt{1-\eta^2}}{\sqrt{1+S\psi^2\eta^2}} K(\psi, S) P_2'(\eta) \tag{4.24}$$

with $K(\psi, S)$ defined as:

$$K(\psi, S) = \begin{cases} -\dfrac{\psi^4}{3}, \quad S = 0 \\ \dfrac{Q_2(\frac{1}{\psi\sqrt{-S}})}{Q_2'(\frac{1}{\sqrt{-S}})} \psi\sqrt{-S} = \begin{cases} \dfrac{\left(\frac{3}{2\psi\sqrt{-S}} - \frac{\psi\sqrt{-S}}{2}\right) 2atanh(\psi\sqrt{-S}) - 3}{\frac{3}{\sqrt{-S}} 2atanh(\sqrt{-S}) - \frac{3+S}{1+S} - 3}, & S < 0 \\ \dfrac{\left(\frac{3}{2\psi\sqrt{S}} + \frac{\psi\sqrt{S}}{2}\right) 2arctan(\psi\sqrt{S}) - 3}{\frac{3}{\sqrt{S}} 2arctan(\sqrt{S}) - \frac{3+S}{1+S} - 3}, & S > 0 \end{cases} \end{cases} \tag{4.25}$$

And in the liquid phase, $u_L = (u_{L,\psi}, u_{L,\eta})$ reads:

$$u_{L,\psi} = -\frac{1}{h_\psi}\frac{\partial \Phi_G}{\partial \psi} = \frac{-RS_t}{3(1+S)^{4/3}}\frac{\sqrt{1+S\psi^2}}{\sqrt{1+S\psi^2\eta^2}}\frac{3\eta^2-1}{2\psi} \tag{4.26}$$

and

$$u_{L,\eta} = -\frac{1}{h_\eta}\frac{\partial \Phi_G}{\partial \eta} = \frac{RS_t}{3(1+S)^{4/3}}\frac{\sqrt{1-\eta^2}}{\sqrt{1+S\psi^2\eta^2}}\frac{\eta(3+S\psi^2)}{2\psi} \tag{4.27}$$

The velocity field in both liquid and gaseous phases in the Cartesian coordinate system (r, z) can also be derived by the following:

$$\begin{aligned} u_{G,r} &= \frac{\partial \Phi_G}{\partial r}, \quad u_{L,r} = \frac{\partial \Phi_L}{\partial r} \\ u_{G,z} &= \frac{\partial \Phi_G}{\partial z}, \quad u_{L,z} = \frac{\partial \Phi_L}{\partial z} \end{aligned} \tag{4.28}$$

and

$$\begin{aligned} \frac{\partial \Phi_{G,L}}{\partial r} &= \frac{\partial \Phi_{G,L}}{\partial \psi}\psi_r + \frac{\partial \Phi_{G,L}}{\partial \eta}\eta_r \\ \frac{\partial \Phi_{G,L}}{\partial z} &= \frac{\partial \Phi_{G,L}}{\partial \psi}\psi_z + \frac{\partial \Phi_{G,L}}{\partial \eta}\eta_z \end{aligned} \tag{4.29}$$

with

$$\begin{bmatrix} \psi_r & \psi_z \\ \eta_r & \eta_z \end{bmatrix} = \frac{\psi}{a(1+S\psi^2\eta^2)}\begin{bmatrix} -\psi\sqrt{1+S\psi^2}\sqrt{1-\eta^2} & -\psi(1+S\psi^2)\eta \\ -\sqrt{1+S\psi^2}\sqrt{1-\eta^2}\eta & 1-\eta^2 \end{bmatrix} \tag{4.30}$$

by the coordinate transformation matrix (Appendix A.7). Substituting Eqn. 4.20 and 4.21 in Eqn. 4.29, yields the velocity field in Cartesian coordinate system:

$$\begin{aligned} u_{G,r} &= \frac{RS_t}{3(1+S)^{4/3}}\frac{\sqrt{1+S\psi^2}\sqrt{1-\eta^2}}{1+S\psi^2\eta^2}\left(-J(\psi,S)P_2(\eta) + 3K(\psi,S)\eta^2\right) \\ u_{G,z} &= \frac{RS_t}{3(1+S)^{4/3}}\frac{\eta}{1+S\psi^2\eta^2}\left(-J(\psi,S)(1+S\psi^2)P_2(\eta) - 3K(\psi,S)(1-\eta^2)\right) \\ u_{L,r} &= \frac{RS_t}{3(1+S)^{4/3}}\frac{\sqrt{1+S\psi^2}\sqrt{1-\eta^2}}{2\psi} \\ u_{L,z} &= \frac{RS_t}{3(1+S)^{4/3}}\frac{-\eta}{\psi} \end{aligned} \tag{4.31}$$

Then the velocity magnitude in both phases is derived:

$$\begin{aligned} |u_G| &= \sqrt{u_{G,\psi}^2 + u_{G,\eta}^2} = \sqrt{u_{G,r}^2 + u_{G,z}^2} \\ &= \frac{R|S_t|}{3(1+S)^{4/3}}\frac{1}{\sqrt{1+S\psi^2\eta^2}}\sqrt{J^2(\psi,S)(1+S\psi^2)P_2^2(\eta) + 9K^2(\psi,S)\eta^2(1-\eta^2)} \\ |u_L| &= \sqrt{u_{L,\psi}^2 + u_{L,\eta}^2} = \sqrt{u_{L,r}^2 + u_{L,z}^2} = \frac{R|S_t|}{3(1+S)^{4/3}}\frac{1}{2\psi}\sqrt{1+3\eta^2+S\psi^2(1-\eta^2)} \end{aligned} \tag{4.32}$$

The Cartesian non-dimensional velocity components $(\overline{u}_r, \overline{u}_z)$ in the two phases are therefore written as:

$$
\begin{aligned}
\overline{u}_{G,r} &= \frac{u_{G,r}}{|u_G|} = \frac{S_t}{|S_t|}\frac{\sqrt{1+S\psi^2}\sqrt{1-\eta^2}}{\sqrt{1+S\psi^2\eta^2}}\frac{-J(\psi,S)P_2(\eta)+3K(\psi,S)\eta^2}{\sqrt{J^2(\psi,S)(1+S\psi^2)P_2^2(\eta)+9K^2(\psi,S)\eta^2(1-\eta^2)}}\\
\overline{u}_{G,z} &= \frac{u_{G,z}}{|u_G|} = \frac{S_t}{|S_t|}\frac{\eta}{\sqrt{1+S\psi^2\eta^2}}\frac{-J(\psi,S)(1+S\psi^2)P_2(\eta)-3K(\psi,S)(1-\eta^2)}{\sqrt{J^2(\psi,S)(1+S\psi^2)P_2^2(\eta)+9K^2(\psi,S)\eta^2(1-\eta^2)}}\\
\overline{u}_{L,r} &= \frac{u_{L,r}}{|u_L|} = \frac{S_t}{|S_t|}\frac{\sqrt{1+S\psi^2}\sqrt{1-\eta^2}}{\sqrt{1+3\eta^2+S\psi^2(1-\eta^2)}}\\
\overline{u}_{L,z} &= \frac{u_{L,z}}{|u_L|} = \frac{-S_t}{|S_t|}\frac{2\eta}{\sqrt{1+3\eta^2+S\psi^2(1-\eta^2)}}
\end{aligned}
\tag{4.33}
$$

4.1.2 Energy Balance and Deformation Parameter

Based on the assumption of potential flow, the flow field is represented. Viscous effects are not considered by entering the momentum equation, rather through the dissipation terms in the energy balance. In this way, the decay of the oscillation amplitude can be described under the assumption of potential flow [42].

The velocity field in both phases are already known. Then, the kinetic energy can be calculated:

$$
E_k = \int \frac{1}{2}\rho u^2 dV = \frac{\pi}{135}\frac{R^5 S_t^2(3+S)}{(1+S)^{8/3}}(\rho_L + \rho_G \Lambda(S)) \tag{4.34}
$$

with

$$
\Lambda(S) = \frac{6}{(3+S)(1+S)}
\begin{cases}
\dfrac{3S(3+2S)+2\sqrt{-S}(S^2+9S+9)atanh(\sqrt{-S})-3(1+S)(3+S)atanh^2(\sqrt{-S})}{2S^2\left(\frac{1}{2\sqrt{-S}}\left(\frac{3+S}{1+S}\right)+\frac{3}{S}atanh(\sqrt{-S})+\frac{3}{2\sqrt{-S}}\right)^2}, & S<0\\
\dfrac{-3S(3+2S)+2\sqrt{S}(S^2+9S+9)arctan(\sqrt{S})-3(1+S)(3+S)arctan^2(\sqrt{S})}{2S^2\left(\frac{1}{2\sqrt{S}}\left(\frac{3+S}{1+S}\right)-\frac{3}{S}arctan(\sqrt{S})+\frac{3}{2\sqrt{S}}\right)^2}, & S>0
\end{cases}
\tag{4.35}
$$

and the surface energy between two phases reads:

$$
E_\sigma = \sigma\int_{\psi=1} dA = 4\pi R^2\sigma\beta(S) \tag{4.36}
$$

with

$$
\beta(S) = \frac{(1+S)^{1/3}}{2}\left(1+\frac{ln(\sqrt{S}+\sqrt{1+S})}{\sqrt{S}\sqrt{1+S}}\right) \tag{4.37}
$$

The total energy consists of the kinetic and surface energy:

$$E_T = E_k + E_\sigma = \frac{\pi}{135}\frac{R^5 S_t^2(3+S)}{(1+S)^{8/3}}(\rho_L + \rho_G\Lambda) + 4\pi R^2\sigma\beta \tag{4.38}$$

The viscous dissipation rate is defined with a negative sign [8]:

$$D_\mu = \int -\frac{1}{2}\mu(\nabla u + (\nabla u)^T) : (\nabla u + (\nabla u)^T)dV = \int_{\psi=1} -\mu\frac{\partial|u|^2}{\partial n}dS \tag{4.39}$$

The total dissipation rate in two phases is:

$$D_{\mu,T} = -\frac{4\pi R^3}{9}\frac{S_t^2}{(1+S)^2}\left(\mu_L + \mu_G M(S)\right) \tag{4.40}$$

with

$$M(S) = \begin{cases} -\dfrac{(9S+12S^2+S^3)+(18+30S+9S^2-S^3)\sqrt{-S}atanh(\sqrt{-S})-9(1+S)^2atanh^2(\sqrt{-S})}{\left[(3+2S)\sqrt{-S}-3(1+S)atanh(\sqrt{-S})\right]^2}, & S<0 \\ \dfrac{8}{3}, & S=0 \\ -\dfrac{-(9S+12S^2+S^3)+(18+30S+9S^2-S^3)\sqrt{S}arctan(\sqrt{S})-9(1+S)^2arctan^2(\sqrt{S})}{\left[(3+2S)\sqrt{S}-3(1+S)arctan(\sqrt{S})\right]^2}, & S>0 \end{cases} \tag{4.41}$$

The energy balance equation is:

$$\frac{dE_T}{dt} = D_{\mu,T} \tag{4.42}$$

Then, substituting into the energy equation yields Eqn. 3.53:

$$S_{tt} - \frac{7}{6}\Omega_1(S)S_t^2 + \frac{5\sqrt{2}}{2}\omega_2 Oh\Omega_2(S)S_t + \omega_2^2\Omega_3(S)S = 0 \tag{4.43}$$

with the coefficients:

$$\begin{aligned} \Omega_1(S) &= \frac{6}{7}\left(\frac{7+\frac{5}{3}S}{2(1+S)(3+S)} - \frac{1}{2}\frac{\rho_G}{\rho_L}\frac{\Lambda'}{1+\frac{\rho_G}{\rho_L}\Lambda}\right), \\ \Omega_2(S) &= \frac{3(1+S)^{2/3}}{3+S}\frac{1+\frac{\mu_G}{\mu_L}M}{1+\frac{\rho_G}{\rho_L}\Lambda}, \\ \Omega_3(S) &= \frac{\beta'}{S}\frac{135(1+S)^{8/3}}{4(3+S)\left(1+\frac{\rho_G}{\rho_L}\Lambda\right)}. \end{aligned} \tag{4.44}$$

Here, Λ' and β' denote the derivatives with respect to S.

Eqn. 4.43 governs the temporal evolution of the deformation parameter $S(t)$. Once $S(t)$ is solved by numerically solving this nonlinear ordinary differential equation, the droplet shape and associated flow fields can be determined.

4.2 Direct Numerical Simulation of Droplet Oscillation using FS3D

Based on the assumption of potential flow, now we can describe the flow field both inside and outside the droplet, as described above. We also wonder how this assumption deviates from the reality. Now the code FS3D (Fress Surface 3D) is employed to perform direct numerical simulations to analyse droplet oscillations, whose results are compared with the analytical solutions in a suitable way, to better show the deviation of this assumption from the real situation.

4.2.1 Computational Settings and Grid Resolution Convergency Study

The droplet radius R, gas ρ_G and liquid ρ_L density, gas μ_G and liquid μ_L dynamical viscosity, surface tension coefficient σ are listed in Tab.1.

Table 1: Parameter settings

$R\ [m]$	$\rho_G\ [kg/m^3]$	$\rho_L\ [kg/m^3]$	$\mu_G\ [Pa\cdot s]$
0.5333×10^{-3}	1.1894	998.19	18.198×10^{-6}
$\mu_L\ [Pa\cdot s]$	$\sigma\ [N/m]$	$\omega_2\ [1/s]$	$Oh\ [-]$
0.003	76.4×10^{-3}	2009.2 by [9]	0.014876

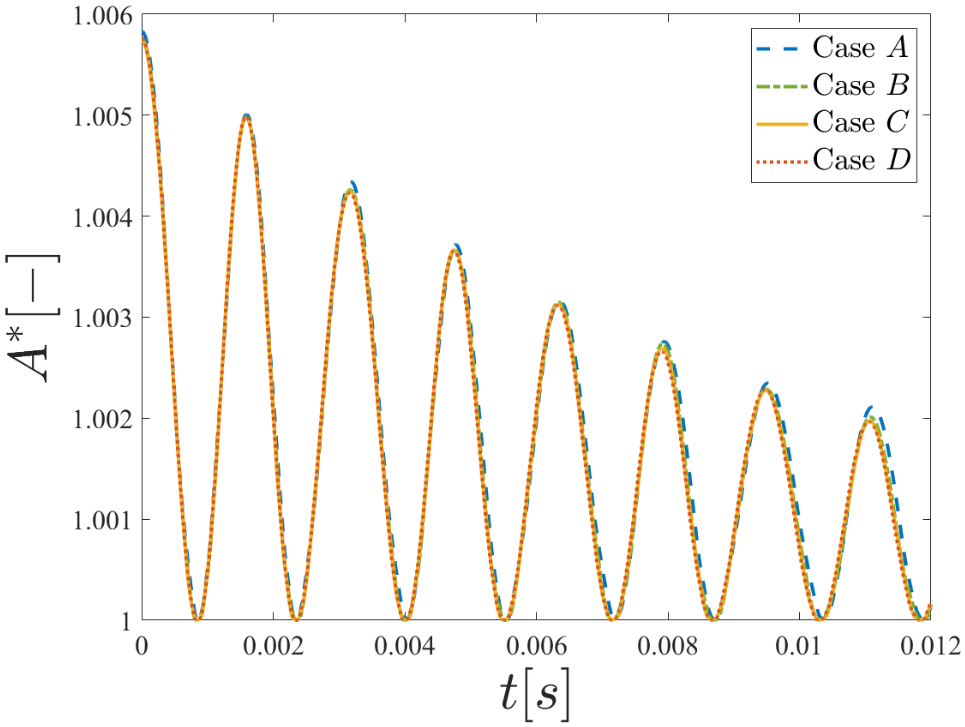

Figure 6: Normalized surface area A^* with time for four cases with various grid numbers: case A: 128^3, case B: 192^3, case C: 256^3 and case D: 384^3.

The grid resolution convergency study is done by comparison among four cases with various grid numbers: case A: 128^3, case B: 192^3, case C: 256^3 and case D: 384^3. The temporal evolution of the normalized surface area $A^* = \frac{A}{A_{min}}$ for these four cases is shown in Figure 6. Case C and D collapse together. The relative difference between Case B and C is about 3×10^{-5}. By considering the computational accuracy and efforts, the grid numbers 256^3 in case C are chose for the following simulations.

4.2.2 Results from FS3D Simulations and Discussions

This section displays the simulation results for droplet oscillations. The analytical solutions are calculated with the same parameters as the simulations, listed in Tab. 1. The deformation parameter $S(t)$ is obtained by numerically solving Eqn. 4.43. The instant flow field is described by Eqn. 4.31. The initial aspect ratio in both simulation and analytical model is set to $\varepsilon = 1.20$.

Figure 7 compares the velocity field calculated by the analytical model and predicted by the numerical code FS3D at varied times. The velocity field by the analytical model is in the left column. For the spherical shape, the velocity is the highest and differs for different oscillation directions. As the droplet contracts from a prolate shape to an oblate shape, the streamline in the gaseous phase is from the equator back to the poles, while for the droplet rebounding from an oblate shape to a prolate shape, the streamline flows from the poles to the equator. It is observed that the velocity on the droplet surface in the gaseous phase and liquid phase has the same normal component, but different tangential components, since the boundary condition on the surface (Eqn. 4.2) only restricts the normal component of the velocity within both phases. Due to the inviscid assumption, there is no tangential conditions at the interface. This discontinuity of the tangential velocity is most evident for spherical shapes, when the velocity is high, and much smaller when the velocity field is slow. Note that in Figure 7, the prolate and oblate shapes are close to the maximum extended shapes, so the velocity for corresponding shapes is very small but not zero. Code FS3D solves the full momentum equation, its results are shown in the right column in Figure 7. The vortex is evident near the interface in the gas phase, this is the main difference between the gas velocity field by the analytical model and by the numerical code FS3D. The vortex is located where the discontinuity of the tangential velocity within two phases, due to the assumption of a potential flow, is the largest. The vortex is stronger for spherical shapes. However, no evident vortex in the liquid phase is observed for any shapes, and the liquid velocity field by the analytical model and numerical code FS3D is quite similar. This comparison of the velocity field mainly brings us an impression of the difference caused by the assumption of a potential flow, but not quantitatively.

The velocity field by the analytical model is based on the assumption of a potential flow, while that by the numerical code FS3D does not hold this assumption and is rotational. Therefore, the

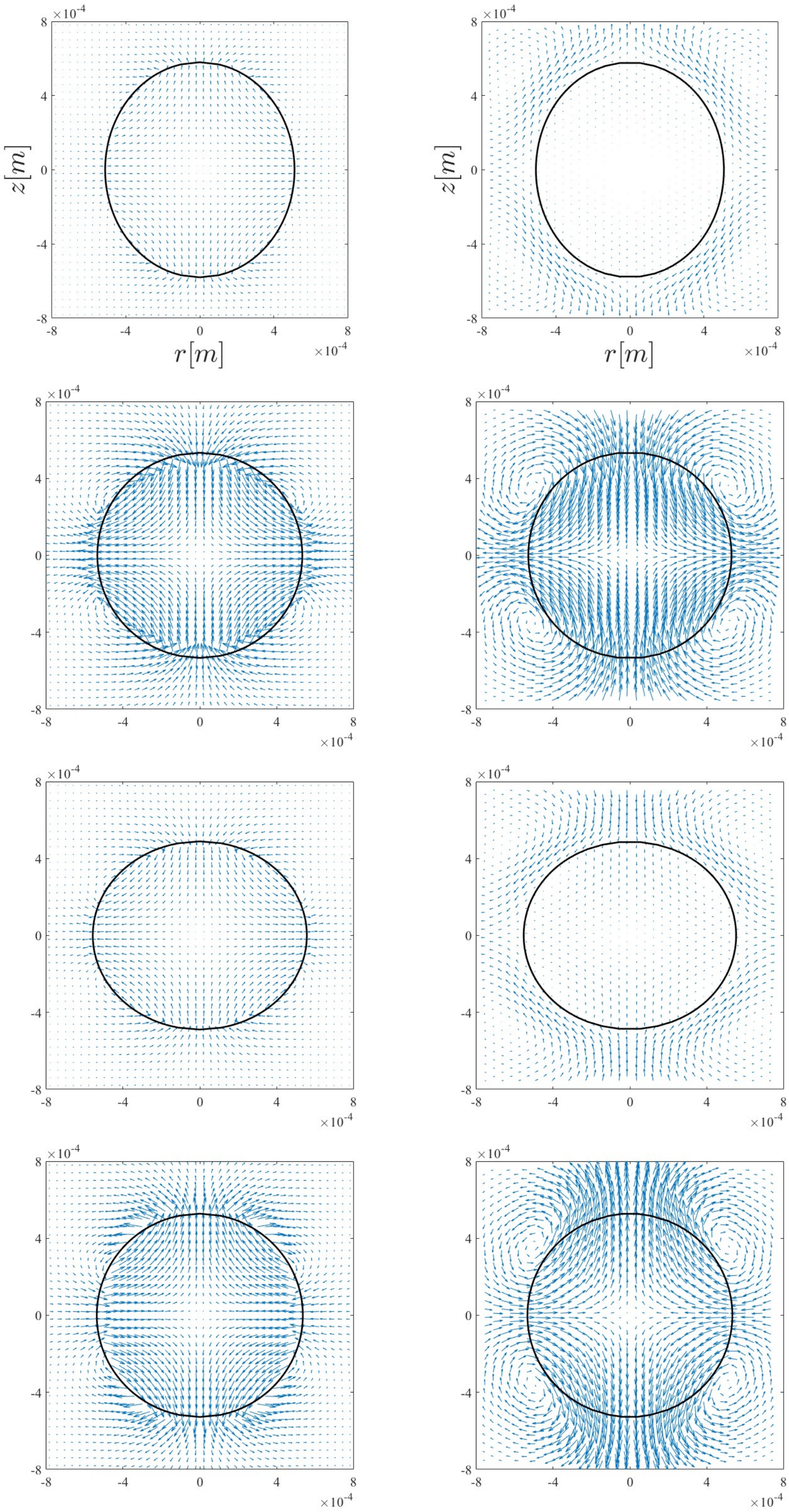

Figure 7: Velocity field (side view) obtained by the analytical model (left column) and by the numerical code FS3D (right column) under the same oscillating conditions, within one period (not the first period). From top to bottom: aspect ratio $\varepsilon = 1.1341, 1.0063, 0.8784, 0.9882$.

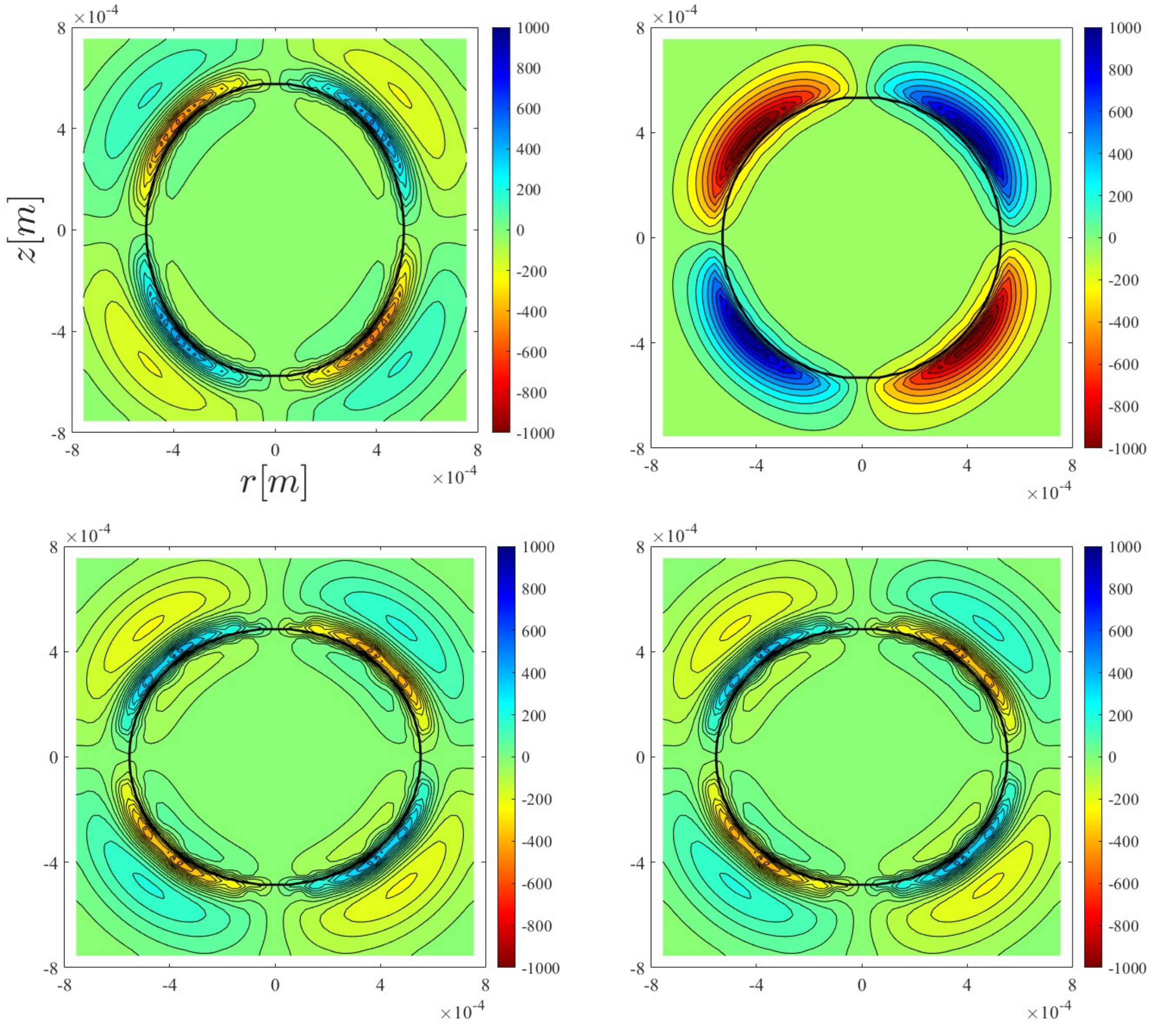

Figure 8: Vorticity field (side view) by the results of the numerical code FS3D, within one period (not the first period). From top left to bottom right: aspect ratio $\varepsilon = 1.1341, 1.0063, 0.8784, 0.9882$.

difference caused by this assumption can be quantitatively discussed by the vorticity field obtained by the simulations, as reported in Figure 8. The value represents the vorticity intensity, and the positive and negative sign corresponds to the vorticity pointing into and out of the plane. The vorticity inside the droplet remains confined to a very thin region near the interface and is overall much weaker than that in the gaseous phase. In the gaseous phase, the vorticity is strongest when the velocity is largest (spherical state). The vortex has an opposite direction for different oscillation directions. For a prolate and an oblate shape, when the velocity is slow, the vorticity is much smaller compared to that for a spherical shape. Except for a narrow vortex near the surface, another one in the opposite direction can be observed at a larger distance from the surface, since the droplet is close to the maximum extended shape, and the flow changes direction. The vortex of the opposite direction is generated on the surface and spreads into the gaseous phase. Therefore, two vortices of opposite directions can be observed.

In the present case, the kinematic viscosity is $\nu_G = 15.3 \times 10^{-6}\ m^2/s$ and $\nu_L = 3.0 \times 10^{-6}\ m^2/s$. Then the penetration distance of the vorticity from the droplet surface can be estimated by $\delta = \sqrt{\frac{\nu}{\omega_L}}$ [37] (see Section 3.4). When evaluating the oscillation frequency ω_L approximately by ω_2 the oscillation frequency in mode $l = 2$, δ_L is 0.03868 mm for the liquid phase, and δ_G is 0.08726 mm for the gaseous phase. The larger viscosity in the gaseous phase means that the vorticity can diffuse for a longer distance, as illustrated in Figure 8. It leads to a thicker viscous layer and a smoother vorticity gradient.

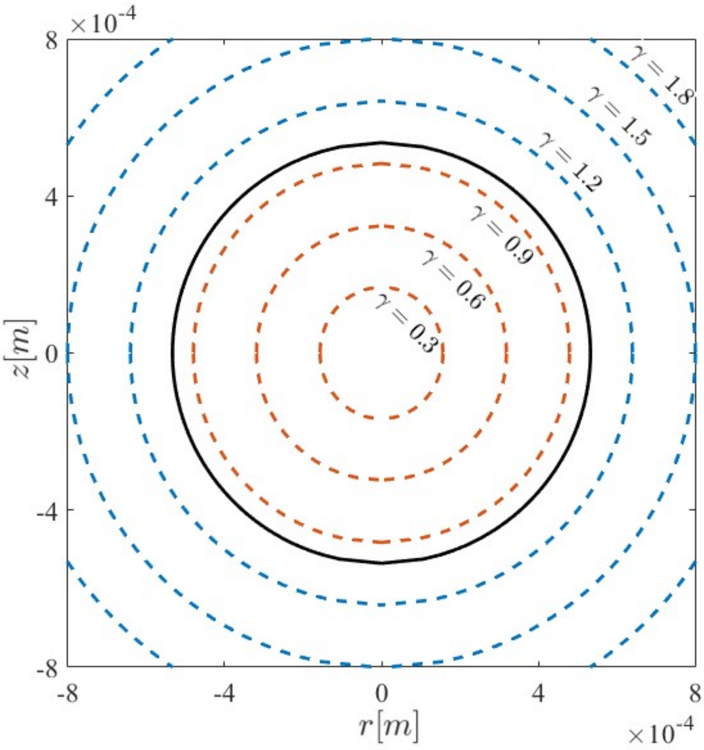

Figure 9: Concentric spheres of the volume-equivalent radius γR, for varied values of γ ($\gamma = 0.9, 0.6, 0.3$ inside the droplet, $\gamma = 1.2, 1.5, 1.8$ outside the droplet).

The difference caused by the assumption of a potential flow can also be quantitatively investigated through the velocity components at different distances from the surface. The non-dimensional velocity $\overline{u} = (\frac{u_r}{|u|}, \frac{u_z}{|u|})$ at different concentric spheres of the volume-equivalent radius γR is taken into account. As discussed above, the vortex is the strongest for spherical shapes. For a maximum prolate/oblate shape, the velocity is very slow and the velocity magnitude is quite small, so the fluctuations of the non-dimensional velocity by the numerical code FS3D can be evident. Therefore, we choose an almost spherical shape of $\varepsilon = 1.0063$ to investigate in the following. In the gaseous phase, we choose the concentric spheres of different equivalent radius $\gamma = 1.2, 1.5, 1.8$ in the gaseous phase, and $\gamma = 0.9, 0.6, 0.3$ in the liquid phase, as reported in Figure 9, which shows different locations for varied values of γ.

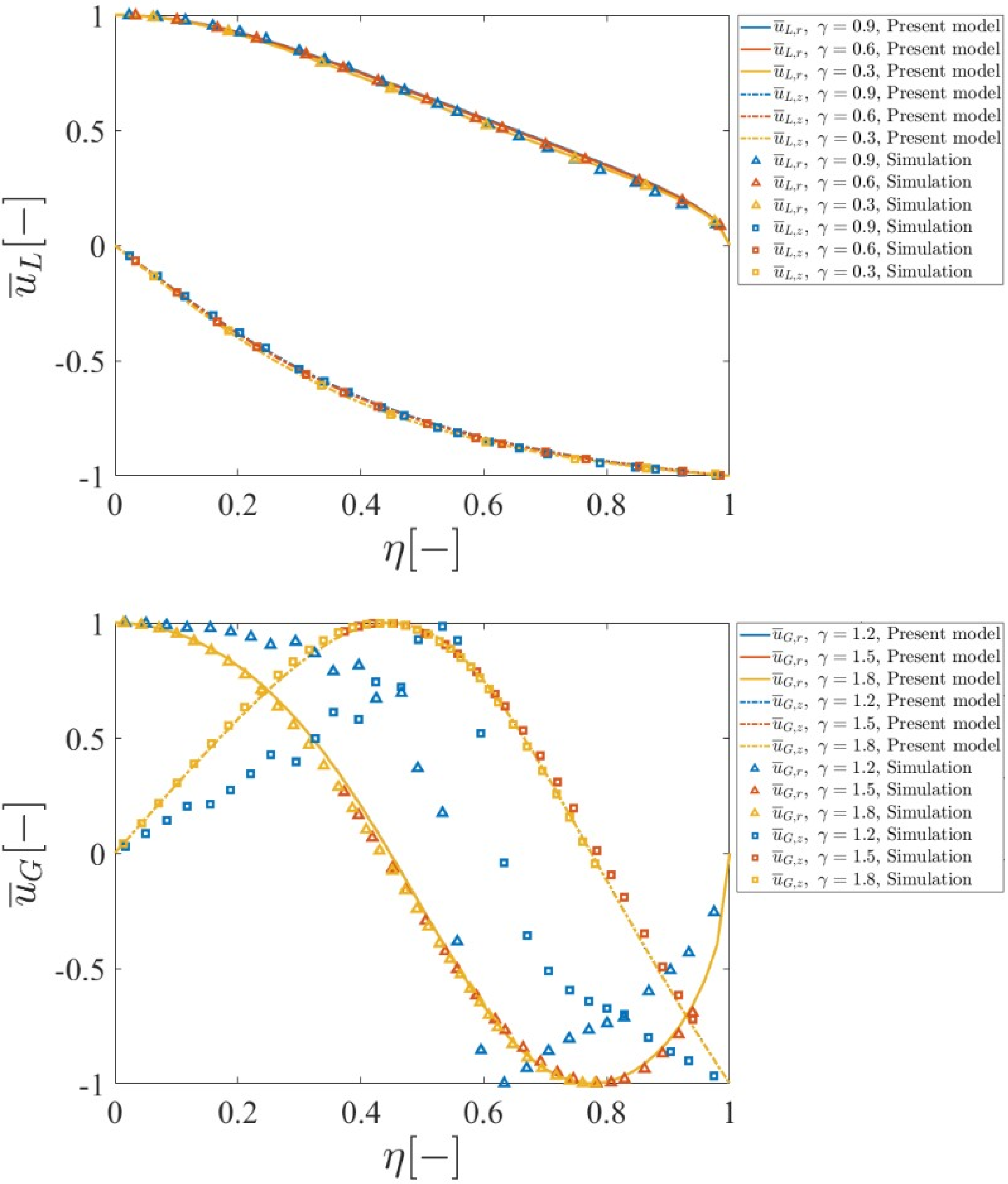

Figure 10: Non-dimensional velocity in the liquid phase (top) $\overline{u}_L = (\frac{u_{L,r}}{|u_L|}, \frac{u_{L,z}}{|u_L|})$ and gaseous phase (bottom) $\overline{u}_G = (\frac{u_{G,r}}{|u_G|}, \frac{u_{G,z}}{|u_G|})$ at different locations inside ($\gamma = 0.9, 0.6, 0.3$) and outside ($\gamma = 1.2, 1.5, 1.8$) the droplet, by the analytical model (lines) and the numerical code FS3D (scatter plots). Analytical results collapse together.

The non-dimensional velocity $\overline{u}$ for a spherical shape ($\varepsilon = 1.0063$) at different locations by the analytical model (by Eqn. 4.33) and the numerical code FS3D are compared in Figure 10, to better show the difference caused by the assumption of a potential flow. Due to the symmetry, the region between $\eta = 0$ and 1 is chosen to display. In both phases, the non-dimensional velocity components $\overline{u}_r, \overline{u}_z$ by the analytical model overlap for different γ. For a spherical shape $S = \frac{1-\varepsilon^2}{\varepsilon^2} = 0$, the non-dimensional velocity by Eqn. 4.33 is only dependent on η, but independent of ψ. Therefore, the non-dimensional velocity at different locations collapses together. Under the assumption of a potential flow, for a spherical droplet, the non-dimensional velocity profile at different locations inside the droplet and outside the droplet is the same, respectively. In the liquid phase, the numerical and analytical results coincide very well, which is also observed from the vorticity field. In the gaseous phase, due to the strong vortex near the surface, the results of the numerical code FS3D deviate from those of the analytical model at the confocal ellipsoid of $\gamma = 1.2$, which crosses through the vortex center. The maximal difference between them is about 0.85 (about $\eta = 0.47$), where the velocity by the analytical model has the opposite direction as the velocity by the numerical code FS3D due to the vortex. Although the difference ($0.85 \sim 0.56$ for $\eta = 0.47 \sim 0.53$) is evident, the trend of velocity with η is still similar for both methods. As the distance from the surface increases over the penetration distance of the vorticity, the difference between the analytical model and the numerical code FS3D is quickly reduced. At the concentric spheres of $\gamma = 1.5$ and 1.8, the results by both methods agree very well.

From the results and discussion above, it was found that the main difference caused by the assumption of a potential flow from the numerical results is the absence of a vortex in the gaseous phase near the surface. For spherical shapes, when the velocity is at its highest value, this vortex is the strongest. While close to the maximal extended shapes, it is much smaller. Except for this vortex, the velocity field in the gaseous phase of the analytical model and that of the numerical code FS3D are in good agreement. In the liquid phase, the results of both methods at $\gamma = 0.9$ coincide very well, since vortex inside the droplet is only confined in a narrow area near the surface, for the whole oscillating process.

Chapter 5. Evaporation Characteristics of an Oscillating Droplet

In this chapter, the evaporation of an oscillating droplet is investigated. An initially spheroidal droplet suspended in air undergoes shape oscillations driven primarily by the interplay between surface tension and inertia, while viscous effects lead to the damping of the oscillation. Simultaneously, mass transfer occurs across the liquid-gas interface due to vapour diffusion in the surrounding gas phase. In the classical droplet evaporation models [57, 71, 77, 90], vapour transport in the gaseous phase is often assumed to be purely diffusion-controlled under quasi-steady assumptions. In the present work, however, the oscillatory motion of the droplet induces a surrounding flow field, and the vapour transport is therefore governed by a convection-diffusion process. Thermal effects are neglected and the droplet is assumed to remain isothermal, which allows the analysis to focus on the effect of the moving interface induced by the droplet oscillation on the vapour transport and evaporation process. The results predicted by the analytical model under quasi-steady assumptions [71] could be taken as a comparison, to indicate this influence.

Section 5.1 introduces an analytical/numerical evaporation model for an oscillating droplet under the assumption of potential flows. The droplet oscillation model introduced in the last Section 4.1 is integrated with the evaporation to obtain the evaporation model for an oscillating droplet. Then, COMSOL Multiphysics (General Form of PDE) is used to solve the species conservation and Laplace equations. The moving boundary problem is transformed to a fixed boundary one by adopting the generalized spheroidal coordinate system, which is introduced in Section 3.6. The effect of a moving interface on the droplet evaporation characteristics is mainly focused on. In Section 5.2, the evaporation of an oscillating droplet in air is numerically investigated by using the in-house code Free Surface 3D (FS3D), which is developed for direct numerical simulations (DNS) of incompressible multiphase flows (see Section 3.9).

The simplified analytical model for the evaporation of a spheroidal droplet under quasi-steady assumptions in [71] is briefly introduced here, since its analytical solutions under quasi-steady assumptions are generally used as a comparison in our work on the evaporation of an oscillating droplet. The steady species conservation equations in the gaseous phase are solved. Under the quasi-steady assumption, the vapour mass fraction χ distribution for a prolate/spherical/oblate shape in a prolate/oblate coordinate system (ζ, η, φ) or in a spherical coordinate system (r, η, φ), follows:

$$\frac{ln\left(\frac{1-\chi}{1-\chi_s}\right)}{ln\left(\frac{1-\chi_\infty}{1-\chi_s}\right)} = 1 - \frac{atanh\left(\frac{1}{\zeta+\sqrt{\zeta^2-1}}\right)}{atanh\left(\frac{1}{\zeta_0+\sqrt{\zeta_0^2-1}}\right)}, \ prolate \tag{5.1a}$$

$$\frac{ln\left(\frac{1-\chi}{1-\chi_s}\right)}{ln\left(\frac{1-\chi_\infty}{1-\chi_s}\right)} = 1 - \frac{R}{r}, \ spherical \tag{5.1b}$$

$$\frac{ln\left(\frac{1-\chi}{1-\chi_s}\right)}{ln\left(\frac{1-\chi_\infty}{1-\chi_s}\right)} = 1 - \frac{arctan\left(\frac{1}{\zeta+\sqrt{\zeta^2-1}}\right)}{arctan\left(\frac{1}{\zeta_0+\sqrt{\zeta_0^2-1}}\right)}, \quad oblate \tag{5.1c}$$

The evaporation flux $n_{ev.qs}$ and evaporation rate $\dot{M}_{qs}$read:

$$n_{ev.qs} = (R\kappa_G)^{1/4} \frac{\dot{M}_{qs}}{4\pi R^2} \tag{5.2}$$

$$\dot{M}_{qs} = 4\pi\rho_G D R \frac{|1-\varepsilon^2|^{1/2}}{\varepsilon^{1/3}} ln\left(\frac{1-\chi_\infty}{1-\chi_s}\right) \begin{cases} \dfrac{1}{2atanh\left(\zeta_0+\sqrt{\zeta_0^2-1}\right)}, \ prolate \\ \dfrac{1}{2arctan\left(\zeta_0+\sqrt{\zeta_0^2-1}\right)}, \ oblate \end{cases} \tag{5.3}$$

where $\kappa_G = k_1 k_2$ is the Gauss curvature (k_1, k_2 are two principal curvatures), R is the equivalent volume radius, and D is the binary diffusivity of the vapour in air. $\zeta_0 = \sqrt{\left|\frac{\varepsilon^2}{1-\varepsilon^2}\right|}$ denotes the value of the spheroidal coordinate corresponding to the droplet surface. Under quasi-steady assumptions, the evaporation flux of a spheroid is proportional to the fourth root of the dimensionless Gauss curvature. A prolate droplet has a higher evaporation flux at the poles, while an oblate droplet has a higher evaporation flux at the equator.

To distinguish the quasi-steady condition from the unsteady condition, Péclet number $Pe = \frac{t_D}{t_\omega}$ is introduced in Section 3.4, with the characteristic time scale of diffusion $t_D = \frac{R_0^2}{D}$ and the characteristic time scale of oscillation $t_\omega = \frac{1}{\omega_L} \approx \sqrt{\frac{\rho_L R_0^3}{8\sigma}}$ (oscillation frequency is approximated by ω_2). R_0 is the initial volume-equivalent radius. When $Pe \ll 1$, for which the characteristic time scale of mass diffusion is much smaller than the characteristic time of droplet oscillation, the quasi-steady assumption is valid. In the present investigation of the evaporation of an oscillating droplet, however, $Pe = O(10)$. Therefore, the quasi-steady assumption becomes questionable, and deviations from the analytical predictions given by Eqn. 5.2 and 5.3 [71] can be expected, which is the main focus of our investigation.

5.1 An Analytical/Numerical Model for the Evaporation of an Oscillating Spheroidal Droplet

Integrating the droplet oscillation model described in Section 4.1 and the droplet evaporation, this section introduces an analytical/numerical model for the evaporation of an oscillating spheroidal droplet. To simplify the problem, the following assumptions hold for the present model.

(1). The droplet is a perfect spheroid, which oscillates between a prolate and an oblate shape. Therefore, a generalized spheroidal coordinate system (ψ, η, φ), described in Section 3.6, is employed. In which the moving boundary problem is solved and the position of the interface is where $\psi = 1$. The droplet oscillation is completely described by a time-varying deformation parameter $S(t) = \frac{1-\varepsilon^2(t)}{\varepsilon^2(t)}$. $S < 0$, $S = 0$, and $S > 0$ correspond to a prolate, spherical and oblate shape, respectively. Different from the oscillation model in the last section, now the equivalent radius $R(t)$ is also time-varying due to evaporation.

(2). The problem is reduced to a 2D axisymmetric formulation, and one quarter of the droplet ($\eta \in [0, 1]$) is computed, shown in Figure 11. It greatly reduces the cell numbers in numerically solving process, thus saving a lot of computational effort.

(3). The gaseous phase is an ideal mixture of vapour and air. The diffusion of vapour in the gaseous phase is evaluated by Fick's Law. Since the velocity induced by the droplet oscillation is very small, the gaseous pressure is assumed to be constant. The gas density is also assumed to be constant, regardless of whether the vapour fraction differs at varied locations.

(4). The droplet and gas are assumed to be preheated and uniform, and the droplet temperature is considered uniform and constant. Thermal effects in the gas phase are neglected. Thus, no energy equations are solved, and the temperature dependence of the material properties is not taken into account in the present work. As the temperature field is of interest, the energy equations can be solved additionally. The evaporation characteristics of different surface temperatures are also discussed later, showing that the influence of evaporating conditions on the evaporation behaviour of an oscillating droplet is less significant.

(5). The gas viscosity is ignored. Incompressible and irrotational flows are assumed. Thus, the velocity can be obtained as a solution of the Laplace equation for the potential ($\nabla^2\Phi = 0$, Φ is the velocity potential). This assumption greatly simplifies our model, since it avoids solving the momentum equation to obtain the velocity field.

(6). The vapour mass fraction at the interface is given by the saturated state. Together with the 4^{th} assumption of fixed temperature, it is also constant.

(7). The effect of the decreasing droplet radius on the droplet oscillation frequency is ignored, for the sake of simplicity. In the current work, the evaporation rate is moderately low, and the droplet radius decreases by less than 0.05% within five oscillation-periods. Thus, the effect of the decrease in the radius is expected to be small. The volume-equivalent radius is updated in the evaporation problem and geometric mapping, but its feedback on the oscillation frequency is neglected.

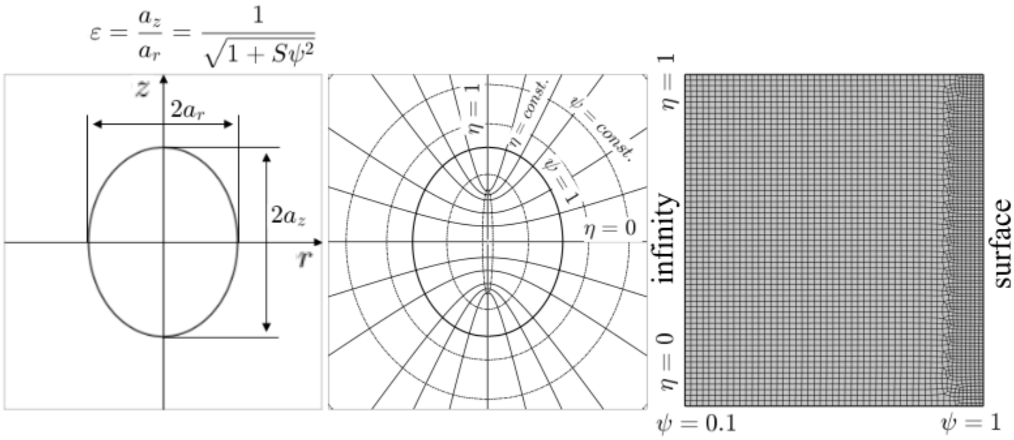

Figure 11: Generalized spheroidal coordinate system and computational domain

5.1.1 Analytical Model

The gas velocity field is described by the gradient of the potential $u = \nabla\Phi$, and the droplet oscillation is only described by the deformation parameter $S(t)$. The vapour distribution is solved for by the time-dependent species conservation equation, which is different from the steady species conservation equation used in [71], and the evaporation can be quantified from the vapour distribution. Therefore, the evaporation model for an oscillating droplet is given by the species conservation (Eqn. 3.11) and Laplace equation (Eqn. 3.42) in the gaseous phase:

$$\frac{\partial \chi}{\partial t} + u \cdot \nabla\chi = D\nabla^2\chi \tag{5.4}$$

$$\nabla^2\Phi = 0 \tag{5.5}$$

D is the binary diffusivity of the vapour in air. We reconstruct the model in a generalized spheroidal coordinate system (ψ, η, φ). τ is dimensionless time by $\tau = \frac{D}{R_0^2}t$ (R_0 the initial volume-equivalent radius). Applying the chain rule, we have:

$$\begin{aligned}\frac{\partial \chi}{\partial t} &= \frac{\partial \chi}{\partial \tau}\frac{\partial \tau}{\partial t} + \frac{\partial \chi}{\partial \psi}\frac{\partial \psi}{\partial t} + \frac{\partial \chi}{\partial \eta}\frac{\partial \eta}{\partial t} = \frac{\partial \chi}{\partial \tau}\frac{D}{R_0^2} + \frac{1}{h_\psi}\frac{\partial \chi}{\partial \psi}h_\psi\psi_t + \frac{1}{h_\eta}\frac{\partial \chi}{\partial \eta}h_\eta\eta_t \\ &= \frac{\partial \chi}{\partial \tau}\frac{D}{R_0^2} + V^* \cdot \nabla\chi\end{aligned} \tag{5.6}$$

with $\nabla\chi = \frac{1}{h_\psi}\frac{\partial\chi}{\partial\psi} + \frac{1}{h_\eta}\frac{\partial\chi}{\partial\eta}$ and the apparent velocity $V^* = [h_\psi\psi_t, h_\eta\eta_t]$ due to the coordinate transformation. Then, in the generalized spheroidal coordinate system, the species conservation in different forms reads:

$$\frac{D}{R_0^2}\frac{\partial\chi}{\partial\tau} + V^*\cdot\nabla\chi + u\cdot\nabla\chi = D\nabla^2\chi \tag{5.7a}$$

$$\frac{D}{R_0^2}\frac{\partial\chi}{\partial\tau} + \nabla\cdot((V^*+u)\chi) = D\nabla^2\chi + \chi\nabla\cdot V^* \tag{5.7b}$$

$$\frac{D}{R_0^2}\frac{\partial\chi}{\partial\tau} + \frac{1}{g^{1/2}}\left(\frac{\partial}{\partial\psi}\left(h_\eta h_\varphi(u_\psi+V_\psi^*)\chi\right) + \frac{\partial}{\partial\eta}\left(h_\psi h_\varphi(u_\eta+V_\eta^*)\chi\right)\right) = \tag{5.7c}$$

$$\chi\nabla\cdot V^* + D\frac{1}{g^{1/2}}\left(\frac{\partial}{\partial\psi}\left(W^\psi\frac{\partial\chi}{\partial\psi}\right) + \frac{\partial}{\partial\eta}\left(W^\eta\frac{\partial\chi}{\partial\eta}\right)\right)$$

and the Laplace equation in different forms reads:

$$\nabla^2\Phi = 0 \tag{5.8a}$$

$$\frac{1}{g^{1/2}}\left(\frac{\partial}{\partial\psi}\left(W^\psi\frac{\partial\Phi}{\partial\psi}\right) + \frac{\partial}{\partial\eta}\left(W^\eta\frac{\partial\Phi}{\partial\eta}\right)\right) = 0 \tag{5.8b}$$

where $h_\psi, h_\eta, h_\varphi$ are the scale factors and $W^\psi, W^\eta, g^{1/2}$ are their products in the generalized spheroidal coordinate system (Appendix A.3).

5.1.1.1 Evaporation Flux n_{ev} and Evaporation Rate $\dot{M}$

As the vapour distribution is solved for, the evaporation flux is evaluated as (Section 3.3):

$$n_{ev} = -\rho_G D\frac{1}{1-\chi}\nabla_n\chi \tag{5.9}$$

at the interface $\psi = 1$, and the evaporation rate is then calculated as the integration of the evaporation flux over the droplet surface:

$$\dot{M} = \int_{\varphi=0}^{2\pi}\int_{\eta=-1}^{1} n_{ev}h_\eta h_\varphi d\eta d\varphi \tag{5.10}$$

Under quasi-steady conditions, the vapour distribution is described by Eqn. 5.1. Transformed in the generalized spheroidal coordinate system, it reads:

$$\frac{ln\left(\frac{1-\chi}{1-\chi_s}\right)}{ln\left(\frac{1-\chi_\infty}{1-\chi_s}\right)} = 1 - \frac{atanh\left(\frac{\sqrt{-S\psi^2}}{1+\sqrt{1+S\psi^2}}\right)}{atanh\left(\frac{\sqrt{-S}}{1+\sqrt{1+S}}\right)},\ S<0 \tag{5.11a}$$

$$\frac{ln\left(\frac{1-\chi}{1-\chi_s}\right)}{ln\left(\frac{1-\chi_\infty}{1-\chi_s}\right)} = 1-\psi,\ S=0 \tag{5.11b}$$

$$\frac{ln\left(\frac{1-\chi}{1-\chi_s}\right)}{ln\left(\frac{1-\chi_\infty}{1-\chi_s}\right)} = 1 - \frac{arctan\left(\frac{\sqrt{S\psi^2}}{1+\sqrt{1+S\psi^2}}\right)}{arctan\left(\frac{\sqrt{S}}{1+\sqrt{1+S}}\right)},\ S>0 \tag{5.11c}$$

As S tends to 0, the vapour distribution of a prolate ($S < 0$) and oblate ($S > 0$) shape converges to that of a spherical shape ($S = 0$). Then the gradient of the vapour mass fraction is calculated, and the evaporation flux $n_{ev.qs}$ under quasi-steady conditions, in the generalized spheroidal coordinate system reads:

$$n_{ev.qs} = \begin{cases} \rho_G D \dfrac{(1+S)^{1/3}}{R} \dfrac{\sqrt{-S}}{2\sqrt{1+S\eta^2}\sqrt{1+S}} \dfrac{ln\left(\frac{1-\chi_\infty}{1-\chi_s}\right)}{atanh\left(\frac{\sqrt{-S}}{1+\sqrt{1+S}}\right)}, & S < 0 \\ \rho_G D \dfrac{(1+S)^{1/3}}{R} ln\left(\dfrac{1-\chi_\infty}{1-\chi_s}\right), & S = 0 \\ \rho_G D \dfrac{(1+S)^{1/3}}{R} \dfrac{\sqrt{S}}{2\sqrt{1+S\eta^2}\sqrt{1+S}} \dfrac{ln\left(\frac{1-\chi_\infty}{1-\chi_s}\right)}{arctan\left(\frac{\sqrt{S}}{1+\sqrt{1+S}}\right)}, & S > 0 \end{cases} \tag{5.12}$$

with vapour mass fraction χ_∞ at infinity, χ_s at the surface. Substituting in Eqn. 5.10 yields the evaporation rate under quasi-steady conditions (Appendix A.8):

$$\dot{M}_{qs} = \begin{cases} 4\pi\rho_G D \dfrac{R}{(1+S)^{1/3}} \dfrac{\sqrt{-S}}{2} \dfrac{ln\left(\frac{1-\chi_\infty}{1-\chi_s}\right)}{atanh\left(\frac{\sqrt{-S}}{1+\sqrt{1+S}}\right)}, & S < 0 \\ 4\pi\rho_G DR ln\left(\dfrac{1-\chi_\infty}{1-\chi_s}\right), & S = 0 \\ 4\pi\rho_G D \dfrac{R}{(1+S)^{1/3}} \dfrac{\sqrt{S}}{2} \dfrac{ln\left(\frac{1-\chi_\infty}{1-\chi_s}\right)}{arctan\left(\frac{\sqrt{S}}{1+\sqrt{1+S}}\right)}, & S > 0 \end{cases} \tag{5.13}$$

The evaporation flux $n_{ev.qs}$ and evaporation rate $\dot{M}_{qs}$, which are predicted by the analytical model assuming quasi-steady mass transfer through the interface [71], are considered as a reference later to quantitatively show the effect of a moving interface on the evaporation characteristics. It was found that a prolate droplet has a higher evaporation rate than an oblate one of the same surface area in [71]. It can be verified by Eqn. 5.13 and Appendix A.4.

5.1.1.2 Normal Interface Velocity V_n and Apparent Velocity V^*

The normal interface velocity V_n in the generalized spheroidal coordinate system, which is used in the boundary conditions at the surface later, reads (Section 3.6, Appendix A.5):

$$V_n = V \cdot n = \frac{(1-3\eta^2)R}{6\sqrt{1+S\eta^2}(1+S)^{5/6}} S_t + \frac{(1+S)^{1/6}}{\sqrt{1+S\eta^2}} R_t = V_{os} + V_{sh} \tag{5.14}$$

where V_{os} is the velocity due to the droplet oscillation and V_{sh} due to the droplet shrinking/evaporation. When the droplet does not evaporate or has a low evaporation rate, the part V_{os} is dominant. V_n has a positive direction towards the gaseous phase.

The apparent velocity V^* in Eqn. 5.7, due to the transformation from Cartesian to the generalized spheroidal coordinate system, is defined as $V^* = [h_\psi \psi_t, h_\eta \eta_t]$. ψ_t and η_t are obtained by the transformation matrix, and V^* is obtained as (Appendix A.9):

$$\begin{aligned} V^* &= [V^*_\psi, V^*_\eta] = [h_\psi \psi_t, h_\eta \eta_t] \\ &= \left[\frac{DR\sqrt{1+S\psi^2}}{R_0^2 \psi (1+S)^{1/3} \sqrt{1+S\eta^2\psi^2}} \left(\frac{R_\tau}{R} - \frac{S_\tau}{3(1+S)} + \frac{\psi^2(1-\eta^2)S_\tau}{2(1+S\psi^2)} \right), \right. \qquad (5.15) \\ &\qquad \left. \frac{DR\psi\eta\sqrt{1-\eta^2}}{R_0^2 (1+S)^{1/3} \sqrt{1+S\eta^2\psi^2}} \left(\frac{SR_\tau}{R} - \frac{SS_\tau}{3(1+S)} + \frac{S_\tau}{2} \right) \right] \end{aligned}$$

$$(5.16)$$

Then its divergence is:

$$\nabla \cdot V^* = -3\frac{DR_\tau}{R_0^2 R} + \frac{D(1-\eta^2\psi^2)S_\tau}{R_0^2(1+S)(1+S\eta^2\psi^2)} \qquad (5.17)$$

5.1.1.3 Initial and Boundary Conditions

To reduce the computational effort, the initial vapour distribution χ is set to be that given under quasi-steady conditions, described by Eqn. 5.11. If the initial vapour distribution χ is set to 0, it cannot have a steady variation even after dozens of oscillation periods. The evaporation rate in the first few periods is too large due to a very high vapour gradient, and it reduces the droplet radius too fast. The effect of a decreasing radius on the droplet oscillation may no longer be negligible. The initial value of velocity potential Φ is set to be uniformly 0 in the whole gaseous phase. Thus, the initial velocity field $u = \nabla\Phi$ is zero.

Shown in Figure 11, the domain is in a range of $\eta \in [0, 1]$ and $\psi \in [0.1, 1]$. One quarter of the gas field is computed as a result of the symmetric droplet. $\psi = 1$ corresponds to the droplet surface, the lowest limit of ψ is set at $\psi = 0.1$, instead of $\psi = 0$, which refers to infinity from the droplet center. As ψ closes to 0, the numerical errors when evaluating $\frac{\partial}{\partial\psi}$ and $\frac{1}{\psi}$ may occur. $\psi = 0.1$ is a good compromise. For a spherical droplet $S = 0$, $\psi = 0.1$ corresponds to a boundary at a distance of ten times radius. It was found that the corresponding boundary is far enough from the droplet surface with enough accuracy. $\eta = 0$ refers to the equator, while $\eta = 1$ corresponds to the poles.

Both vapour mass fraction χ and velocity potential Φ have symmetry conditions at $\eta = 0$ and $\eta = 1$. At $\psi = 0.1$, χ and Φ has Dirichlet conditions $\chi(0.1, \eta, \tau) = \chi_{0.1}$ and $\Phi(0.1, \eta, \tau) = 0$. $\chi_{0,1}$ is also evaluated by the steady vapour distribution from Eqn. 5.11. At the interface $\psi = 1$, the vapour is assumed to be saturated. χ has Dirichlet conditions $\chi(1, \eta, \tau) = \chi_s$, χ_s is the saturated vapour mass fraction. Φ has Neumann condition at $\psi = 1$. Recalling the definition of evaporation flux $n_{ev} = \rho_G(u_{G,n} - V_n)$ and according to Eqn. 5.9 $n_{ev} = -\rho_G D \frac{1}{1-\chi} \nabla_n \chi$, Φ satisfies at surface $\psi = 1$:

$$-\frac{1}{h_\psi}\frac{\partial \Phi}{\partial \psi} = -D\frac{1}{1-\chi}\left(-\frac{1}{h_\psi}\frac{\partial \chi}{\partial \psi}\right) + V_n \tag{5.18}$$

The minus sign before $\frac{\partial \Phi}{\partial \psi}$ and $\frac{\partial \chi}{\partial \psi}$ is due to the positive direction of ψ towards the liquid phase, which is in the opposite direction of V_n.

Once the initial deformation parameter $S_0 = \frac{1-\varepsilon_0^2}{\varepsilon^2}$ is given. The time-varying deformation parameter $S(t)$ is obtained by numerically solving Eqn. 4.43 [42], as well as S_t. The derivative of S with respect to the dimensionless time τ is used in the model by $S_\tau = S_t t_\tau = \frac{R_0^2}{D} S_t$. In the present case, the viscosity is ignored ($Oh = 0$). Thus, the droplet oscillation is fully described and controlled by $\frac{\rho_G}{\rho_L}$ and the oscillation frequency in the second mode ω_2 [5].

5.1.2 Implementation of the Solution

An analytical solution of the coupled species conservation Eqn. 5.7 and Laplace Eqn. 5.8 is not available. The General Form in PDE of COMSOL Multiphysics is employed to numerically solve two equations. Matlab is also used for post-processing. During this process, no additional model is adopted. Referring to Figure 11, the cell number is 3600 and denser near the droplet surface. Tab. 2 lists the values of initial equivalent droplet radius R_0, the binary diffusion coefficient D, the droplet temperature T_L, the gaseous ρ_G and droplet ρ_L density, the vapour mass fraction χ_s at the surface, χ_∞ at infinity, and $\chi_{0.1}$ at $\psi = 0.1$, and the oscillation frequency in the second mode ω_2. The thermophysical properties are estimated corresponding to a water droplet at $T_L = 352.15K$.

Table 2: Parameter settings

$R_0\ [m]$	$D\ [m^2/s]$	$T_L\ [K]$	$\rho_G\ [kg/m^3]$	$\rho_L\ [kg/m^3]$
0.5333×10^{-3}	28.45×10^{-6}	352.15	0.8317	998.819
$\chi_s\ [-]$	$\chi_\infty\ [-]$	$\chi_{0.1}\ [-]$	$\omega_2\ [1/s]$	
0.3369	0	by Eqn. 5.11	2020	

Given the initial deformation parameter (e.g. $S_0 = -0.3056$, corresponding to a spheroidal shape with aspect ratio $\varepsilon_0 = 1.2$) as demanded, $S(t), S_t(t)$ are numerically solved for by Eqn. 3.53. The droplet oscillates between a maximum prolate ($S_{min} = -0.3056$) and maximum oblate ($S_{max} = 0.4253$) shape, whose surface areas are identical. The droplet oscillation frequency is 6.5% lower than the oscillation in the second mode ω_2. This is consistent with the effect of the finite amplitude oscillation on the droplet oscillation frequency in [20, 29, 42]. Figure 12 shows the evolution of the deformation parameter $S(t)$ and a phase plot $S(t) \sim S_t(t)$ of the initial value $S_0 = -0.3056$ ($\varepsilon_0 = 1.2$) and

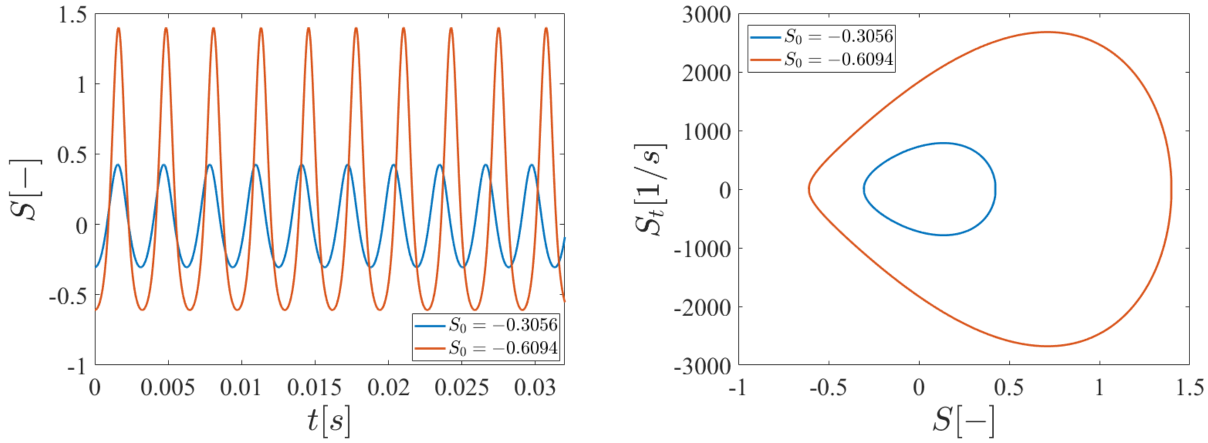

Figure 12: Evolution of the deformation parameter $S(t)$ (left) and a phase plot $S(t) \sim S_t(t)$ (right) of initial value $S_0 = -0.3056$ (blue line) and $S_0 = -0.6094$ (red line), predicted by Eqn. 3.53 [42].

$S_0 = -0.6094$ ($\varepsilon_0 = 1.6$). As the initial droplet deformation increases, the oscillation frequency goes down. The asymmetry in the time spent in a prolate shape and an oblate shape can also be correctly predicted by Eqn. 3.53. The dwell time of an oscillating droplet in a prolate shape is larger than that in an oblate shape, and increases with an increasing initial droplet deformation [30, 42], also reported in Figure 12. It is worth noting that for a maximum extended shape (maximum oblate shape S_{max}, and maximum prolate shape S_{min}), S_t is zero. But for a spherical shape $S = 0$, S_t does not take the maximum values.

5.1.2.1 Computational Loop, Grid and Timestep Resolution Convergence Study

A computational loop with timestep $\Delta t = 2.5 \times 10^{-7}\ s$ is set up. With known vapour mass fraction χ and velocity potential Φ distributions, combined with the values of parameters S, S_τ, R and R_τ, Eqn. 5.7 and 5.8 are solved. New χ and Φ distributions are solved for, and then they are taken as the initial distributions in the next timestep. The evaporation flux n_{ev} by Eqn. 5.9 and the evaporation rate $\dot{M} = \int_{\eta=0}^{1} 4\pi \frac{R^2}{(1+S)^{2/3}} \sqrt{1+S\eta^2}\sqrt{1+S} n_{ev} d\eta$ by Eqn. 5.10 are evaluated at the interface $\psi = 1$. Then the new values of parameters S and S_τ for the next timestep are updated by the solution of Eqn. 3.53. The values of R and R_τ for the next timestep are calculated by mass balance and renewed $R_t(t+\Delta t) = \frac{-\dot{M}}{4\pi R^2(t)\rho_L}$, $R(t+\Delta t) = R(t) + R_t(t+\Delta t)\Delta t$, $R_\tau(t+\Delta t) = \frac{R_0^2}{D} R_t(t+\Delta t)$. After all, the computational loop is repeated. In the first timestep, R takes the initial droplet equivalent volume radius R_0, and R_t is set by the evaporation rate under the quasi-steady conditions.

A series of tests of varied grid and timestep resolutions is conducted to exclude their effect on the simulation results of Eqn. 5.7 and 5.8. Tab. 3 lists the tests of varied cell numbers and timesteps. Figure 13 displays the temporal evolution of the evaporation rate within five periods in various tests

Table 3: Test simulations of varied grid and timestep resolutions

Timestep \ Cell numbers	3600	7600	13100
$2.5 \times 10^{-7}s$	test A	test E	test F
$2.5 \times 10^{-6}s$	test J		
$2.5 \times 10^{-5}s$	test K		

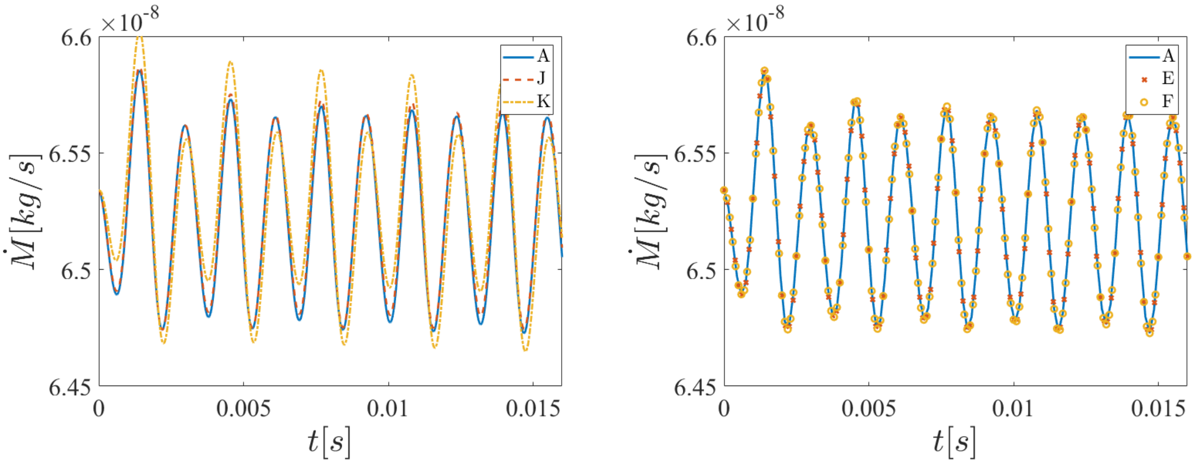

Figure 13: (Left) Timestep resolution effect on the transient evaporation rate, test A: $\Delta t = 2.5 \times 10^{-7}s$**, test J:** $10\Delta t = 2.5 \times 10^{-6}s$ **and test K:** $100\Delta t = 2.5 \times 10^{-5}s$**; (Right) grid resolution effect on the transient evaporation rate, test A:** 3600 **cells, test E:** 7600 **cells, and test F:** 13100 **cells.**

with varied grid and timestep resolutions. The relative difference between test A of timestep Δt and K of $100\Delta t$ is less than 0.23%, and that between test A of timestep Δt and J of $10\Delta t$ is about 0.02%. Between test A of 3600 and F of 13100 cells, the difference is less than 10^{-6}. Taking into account both the accuracy and the computational effort, the value of timestep $\Delta t = 2.5 \times 10^{-7}s$ and cell numbers 3600 adopted in the present setting are assumed sufficient and reliable.

5.1.3 Results From Analytical/Numerical Model and Discussions

The numerical solutions of the present model include two parts: results under steady and unsteady conditions. The analytical results by assuming quasi-steady mass transfer through the interface, described by Eqn. 5.12 and 5.13 [71], are taken as a reference. It is important to mention $Oh = 0$ in this section. In Section 5.1.3.1, the evaporation flux from the numerical solutions of Eqn. 5.7 and 5.8 under steady conditions were compared with the analytical solutions under quasi-steady conditions (Eqn. 5.12), to verify the correctness of the present approach. The values of S and R were set as constant, and as a consequence, S_τ and R_τ remained zero in the computational loop, so that a steady evaporation case is set up. In Section 5.1.3.2, the evaporation of an oscillating droplet (time-varying boundary) is then discussed by numerically solving Eqn. 5.7 and 5.8, in the computational loop the time-varying $S(t)$ is given by numerically solving ordinary differential energy conservation Eqn.

4.43. The numerical results are also compared with the predictions by the analytical model under quasi-steady assumptions. Thus, the effect of a moving interface on the evaporation characteristic is better displayed. The effect of the initial droplet deformation, described by the initial parameter $S_0 = \frac{1-\varepsilon_0^2}{\varepsilon_0^2}$, on the evaporation characteristic is also discussed later.

5.1.3.1 Results under Steady Conditions

The evaporation flux of a steady spheroid was shown to be proportional to the fourth root of the local Gauss curvature (Eqn. 5.2). By setting constant values of the deformation parameter S and of the equivalent radius R in the computational loop, and after some timesteps, the results converge. A steady solution (steady vapour χ and velocity potential Φ distribution) of the species conservation and Laplace equations is obtained, as well as the evaporation flux. These three droplets of prolate ($S = -0.3056$), spherical ($S = 0$) and oblate ($S = 0.4253$) shapes have the same volume, and the prolate/oblate have the same surface area. Figure 14 shows the spatial distribution of the evaporation flux for these three shapes and its comparison with the analytical solution under quasi-steady conditions. For a prolate droplet the evaporation flux is the highest at the poles ($\eta = \pm 1$), and for an oblate droplet the flux is the highest at the equator ($\eta = 0$). While a spherical droplet has an uniform distribution of the evaporation flux over the surface. The evaporation flux of the present model and of the analytical model under quasi-steady assumptions overlap well. The relative difference between them is less than 2×10^{-5}. The good agreement confirms the capability of the present model under quasi-steady conditions.

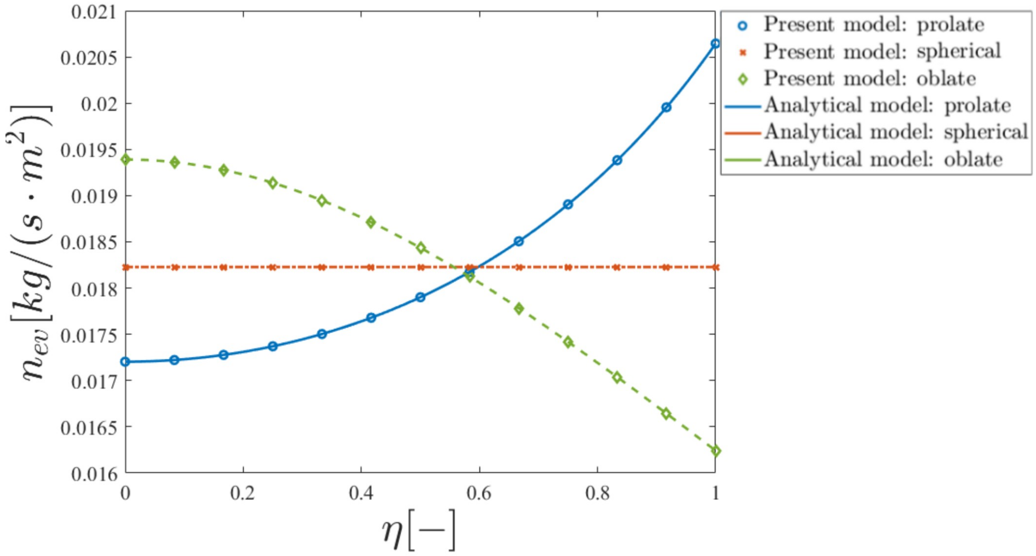

Figure 14: Spatial distribution of the evaporation flux for three shapes, compared with the analytical solution under quasi-steady conditions [71].

5.1.3.2 Results under Unsteady Conditions

This section presents the results of the analytical/evaporation evaporation model for an oscillating droplet and analyses the effect of a moving interface on the evaporation characteristics by taking the results under quasi-steady conditions [71] as a reference. S_{max} (and $S_t = 0$) corresponds to a maximum extension in an oblate shape, while a maximum extension in a prolate shape is obtained for S_{min} (and $S_t = 0$). The spherical shape corresponds to $S = 0$. The case of the initial deformation parameter $S_0 = -0.3056$ ($\varepsilon_0 = 1.2$) is first analysed, and Figure 15 shows the spatial distribution of the dimensionless evaporation flux $\overline{n}_{ev} = \frac{n_{ev}}{n_{ev.sph}}$ over the droplet surface at four different times, when a maximum prolate (S_{min}), spherical ($S = 0$) and oblate S_{max} shape is reached. $n_{ev.sph}$ is the evaporation flux of a spherical droplet with the same surface area under the same evaporating conditions. The dimensionless time is $\bar{t} = t\frac{\omega_2}{2\pi}$. The evaporation flux under quasi-steady conditions in the same evaporating conditions is also reported for comparison. When the droplet contracts from a prolate shape to an oblate shape, the evaporation flux at the poles decreases while it increases at the equator. Conversely, as the droplet returns from an oblate shape to a prolate shape, the flux at the

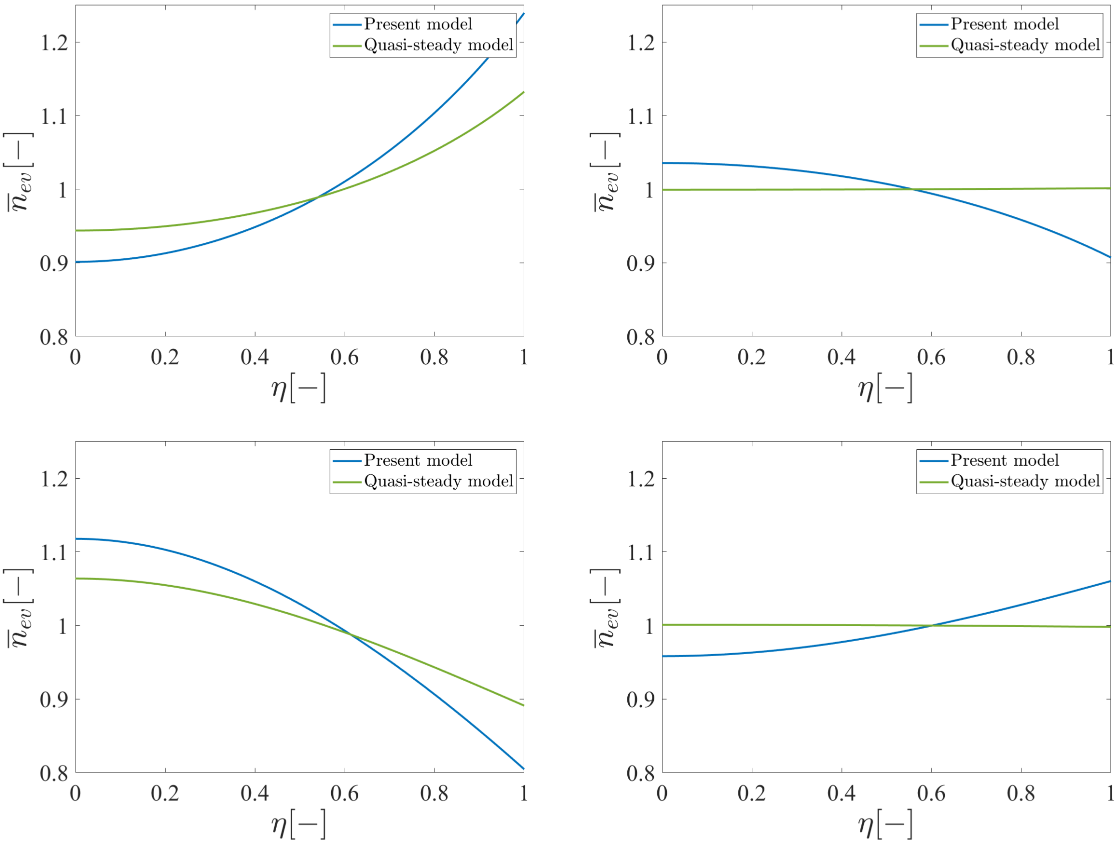

Figure 15: Dimensionless evaporation flux of an oscillating droplet (blue line) and that under quasi-steady conditions (green line). Top left, $t = 0.02818\ s$, maximum prolate shape; Top right, $t = 0.02900\ s$, a spherical shape; Bottom left, $t = 0.02975\ s$, maximum oblate shape; Bottom right, $t = 0.03048\ s$, a spherical shape.

poles increases, while it decreases at the equator. For a spherical shape, the flux is not uniform, unlike the steady solutions; it also depends on the oscillation direction, i.e., towards the prolate or oblate shape. The flux distribution over the surface still has a similar tendency with that under quasi-steady solutions (the highest value at the poles for a prolate shape and at the equator for an oblate shape), but it is quantitatively different. In particular, the flux is no longer proportional to the fourth root of the dimensionless Gauss curvature, and this has an important implication for the time-varying evaporation rate, which will be explained later. Figure 16 reports the maximum relative difference $\left|\frac{n_{ev}-n_{ev.qs}}{n_{ev.qs}}\right|_{max}$ between the evaporation flux n_{ev} and that under quasi-steady conditions $n_{ev.qs}$ within one period with respect to the surface location η. The maximum relative difference at the equator and poles is about 6.6% and 12.6%, respectively. The smallest difference appears near $\eta = 0.58$, where the droplet surface exhibits the smallest movement during the oscillation and the effect of the moving boundary is lower.

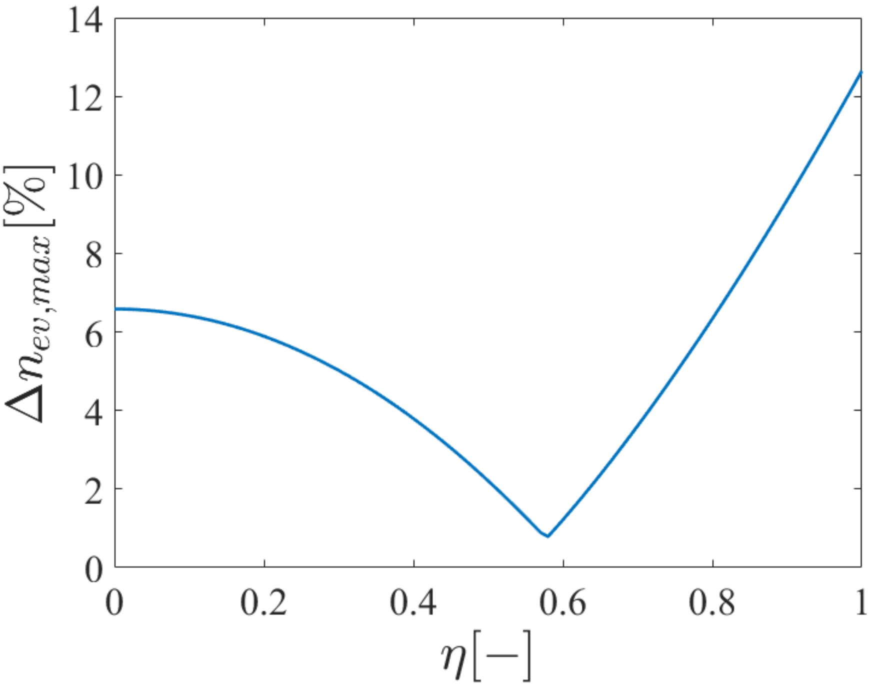

Figure 16: Maximum relative difference $\Delta n_{ev,max} = \left|\frac{n_{ev}-n_{ev.qs}}{n_{ev.qs}}\right|_{max}$ within one period (not the first period) with respect to the surface location η.

The time dependence characteristics of the evaporation flux are discussed here. The temporal evolution of the dimensionless evaporation flux at the poles (red line) and the equator (blue line) is shown in Figure 17. It is found that the peak of the evaporation flux at the poles is ahead of the maximum prolate shape, while the peak at the equator is ahead of the maximum oblate shape. There exists a phase shift between the evaporation flux and the droplet oscillation. For the present case of initial droplet shape $\varepsilon_0 = 1.2$, the phase shift of the peak of the flux at the poles ahead of the maximum

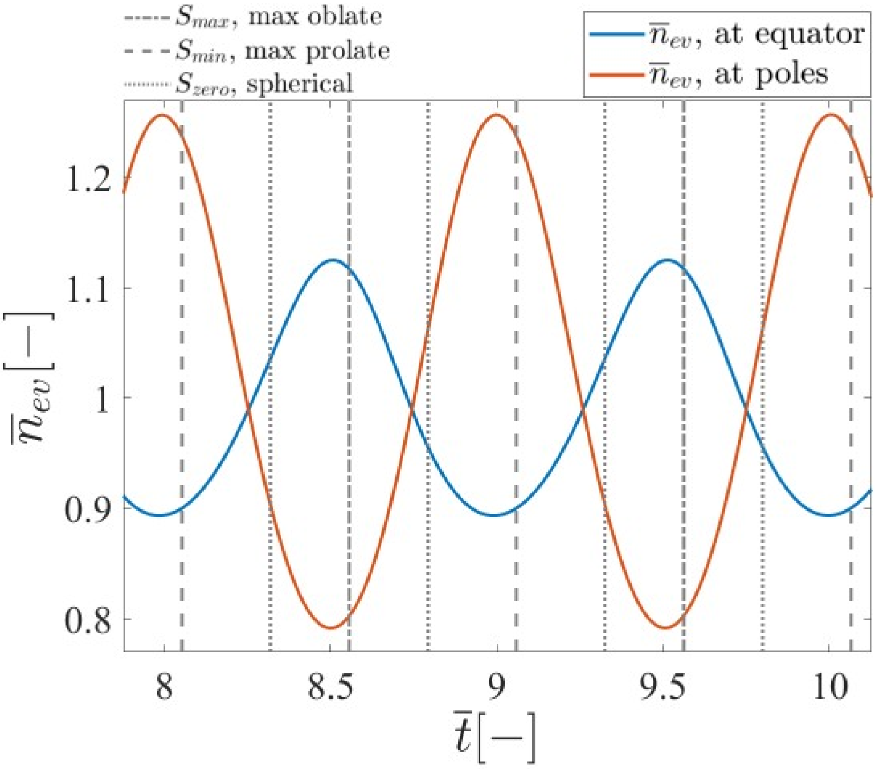

Figure 17: Temporal evolution of the dimensionless evaporation flux at the poles (orange line) and the equator (blue line).

prolate shape (S_{min}) is 0.3206 rad, and the corresponding minimum at the equator is 0.3708 rad ahead of S_{min}. Similarly, the phase shift of the peak at the equator ahead of the maximum oblate shape (S_{max}) is 0.2393 rad, and the corresponding minimum at the poles is 0.2895 rad ahead of S_{max}. The phase shift between the evaporation flux and the droplet oscillation differs at different surface locations and times. Although the phase shift between the evaporation flux and the droplet oscillation exists, the evaporation flux at each location oscillates with the same frequency as the droplet oscillation. Under unsteady conditions, the evolution of the vapour distribution is much slower than the evolution of the interface. As the interface moves, the instantaneous vapour distribution does not match the corresponding steady vapour distribution for the instantaneous droplet shape, which leads to a different evaporation flux compared with the results under quasi-steady assumptions. This unsteady vapour distribution still varies periodically. Thus, a periodic evaporation flux is obtained, but with a different phase shift at different surface locations, compared with the results under quasi-steady conditions.

By integration of the instantaneous evaporation flux over the surface (Eqn. 5.10), the time-varying evaporation rate $\dot{M}$ is evaluated, as reported in Figure 18, which also shows the temporal variation of the dimensionless evaporation rate $\overline{M} = \frac{\dot{M}}{\dot{M}_{sph}}$ (blue line). $\dot{M}_{sph}$ is the evaporation rate of a spherical droplet with the same surface area under the same evaporating conditions. It is evident that the peak of the evaporation rate is ahead of the maximum prolate or oblate shape, and the minimum evaporation

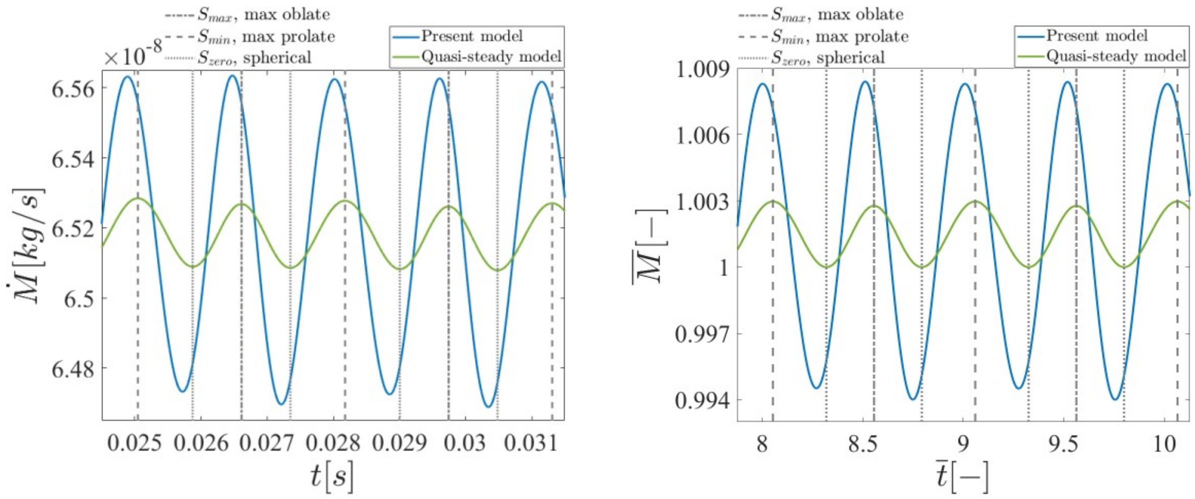

Figure 18: Left: temporal evolution of the evaporation rate (blue line), compared with the analytical solutions (green line) under quasi-steady conditions [71]; Right: temporal evolution of the dimensionless evaporation rate.

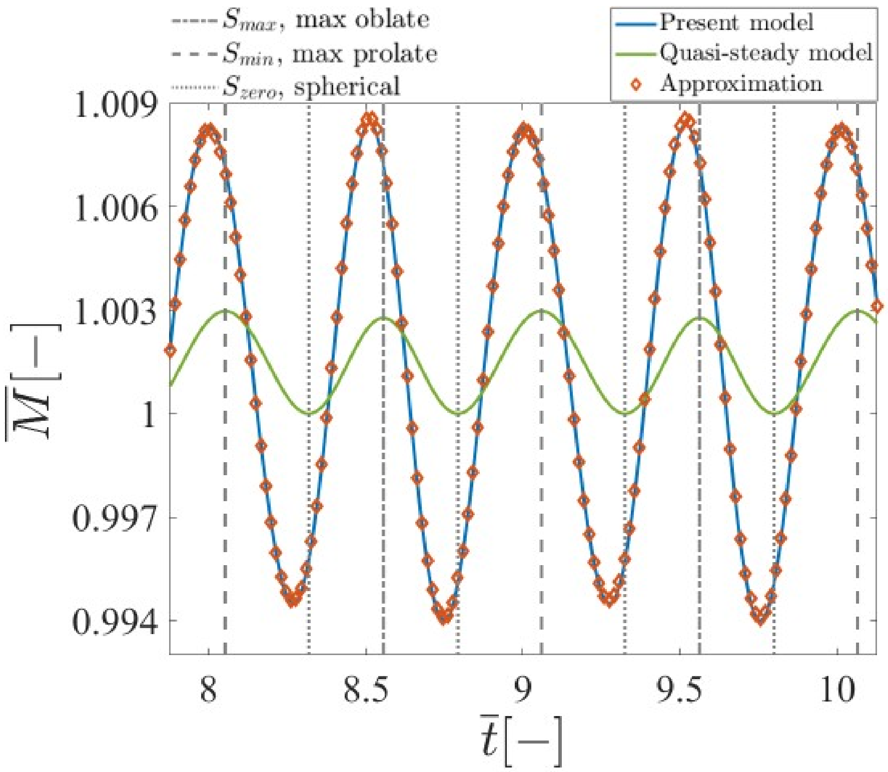

Figure 19: Temporal evolution of the dimensionless evaporation rate (blue line) from the present model, compared with that (red diamonds) from the approximation $n'_{ev} = n_{ev.qs} f(\eta, S, S_t)$.

rate appears before the spherical shape, which does not follow the results predicted by the analytical model under quasi-steady assumptions [71]. This phase shift can be attributed to the evaporation flux for an oscillating droplet, which is different from that under quasi-steady conditions, as mentioned previously. The difference of the evaporation flux distribution from that under quasi-steady conditions can be taken into account by a function $f(\eta, S, S_t)$:

$$n_{ev} = n_{ev.qs} f(\eta, S, S_t) \tag{5.19}$$

As observation, $f(\eta, S, S_t)$ depends on η, as well as S and S_t. From the available numerical data, it is fitted in the form of a fourth order polynomial $f(\eta, S, S_t) = A_0(S, S_t) + A_2(S, S_t)\eta^2 + A_4(S, S_t)\eta^4$ (the odd terms are ignored by 2^{nd} assumption of the symmetrical droplet). Recalling Eqn. 5.10 yields:

$$\dot{M} = \int_{\varphi=0}^{2\pi} \int_{\eta=-1}^{1} n_{ev.qs} f(\eta, S.S_t) h_\eta h_\varphi d\eta d\psi = \dot{M}_{qs} \int_{\eta=0}^{1} f(\eta, S.S_t) d\eta \tag{5.20}$$

Under quasi-steady conditions, the consistency of the evaporation rate and the droplet shape can be explained as the following. From Eqn. 5.13, we known:

$$S = 0 : \frac{\partial \dot{M}_{qs}}{\partial S} = 0, \frac{\partial^2 \dot{M}_{qs}}{\partial S^2} > 0;\ S_{min} : \frac{\partial \dot{M}_{qs}}{\partial S} < 0;\ S_{max} : \frac{\partial \dot{M}_{qs}}{\partial S} > 0 \tag{5.21}$$

The time derivative of $S(t)$ follows:

$$S_{min} : S_t = 0, S_{tt} > 0;\ S = 0 : S_t \neq 0;\ S_{max} : S_t = 0, S_{tt} < 0 \tag{5.22}$$

Thus, for a maximum prolate (S_{min}) or oblate shape (S_{max}), the evaporation rate follows $\frac{\partial \dot{M}_{qs}}{\partial t} = \frac{\partial \dot{M}_{qs}}{\partial S} S_t = 0$ and $\frac{\partial^2 \dot{M}_{qs}}{\partial t^2} = \frac{\partial \dot{M}_{qs}}{\partial S} S_{tt} + \frac{\partial^2 \dot{M}_{qs}}{\partial S^2} S_t^2 < 0$. $\dot{M}_{qs}$ takes the maximum.
As for a spherical shape ($S = 0$), $\dot{M}_{qs}$ follows $\frac{\partial \dot{M}_{qs}}{\partial t} = \frac{\partial \dot{M}_{qs}}{\partial S} S_t = 0$, but $\frac{\partial^2 \dot{M}_{qs}}{\partial t^2} = \frac{\partial \dot{M}_{qs}}{\partial S} S_{tt} + \frac{\partial^2 \dot{M}_{qs}}{\partial S^2} S_t^2 > 0$. $\dot{M}_{qs}$ takes the minimum.
The peak and the minimum of the evaporation rate for steady spheroids are consistent with the droplet shape. But for an oscillating droplet, $n_{ev} = n_{ev.qs} f(\eta, S, S_t)$, the evaporation rate follows:

$$\frac{\partial \dot{M}}{\partial t} = \frac{\partial \dot{M}}{\partial S} S_t + \frac{\partial \dot{M}}{\partial S_t} S_{tt} = \frac{\partial \dot{M}_{qs}}{\partial S} F S_t + \dot{M}_{qs} \frac{\partial F}{\partial S} S_t + \dot{M}_{qs} \frac{\partial F}{\partial S_t} S_{tt} \tag{5.23}$$

with $F = \int_{\eta=0}^{1} f(\eta, S, S_t) d\eta$. For a maximum prolate (S_{min}) or oblate shape (S_{max}), we have $\frac{\partial \dot{M}}{\partial t} = \dot{M}_{qs} \frac{\partial F}{\partial S_t} S_{tt} \neq 0$, $\dot{M}$ does not have a maximum. As for the spherical shape ($S = 0$), we have $\frac{\partial \dot{M}}{\partial t} = \dot{M}_{qs} \frac{\partial F}{\partial S} S_t + \dot{M}_{qs} \frac{\partial F}{\partial S_t} S_{tt} \neq 0$, $\dot{M}$ does not have a minimum. This difference in evaporation flux leads to the phase shift of the evaporation rate and the droplet oscillation.
Figure 19 compares the dimensionless evaporation rate $\overline{M}$ integrated by n_{ev} and by the approximation $n'_{ev} = n_{ev.qs} f(\eta, S, S_t)$, of which $A_{0,2,4}(S, S_t)$ are fitted in a form of a fourth-order double polynomial

$(A_{0,2,4}(S,S_t) = \sum_{i=0}^{4} c_i S^i S_t^{4-i})$. The good agreement verifies the assumed form of $f(\eta, S, S_t)$ in the fourth-order polynomial and the fact that the difference between the evaporation flux and that under quasi-steady conditions leads to a phase shift between the evaporation rate and droplet oscillation.

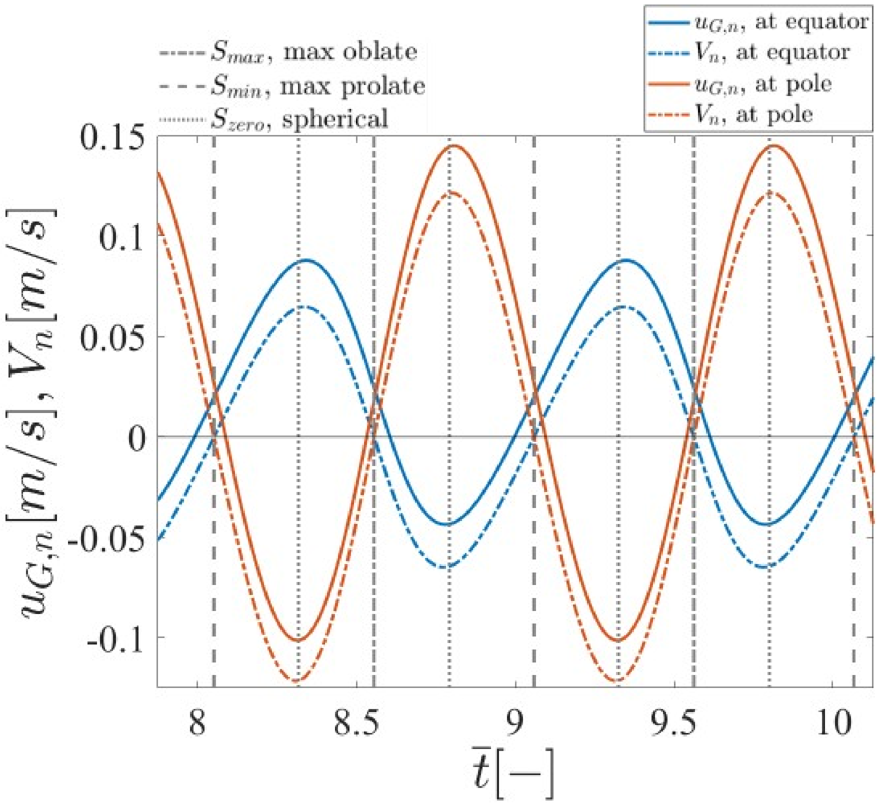

Figure 20: Temporal evolution of the normal component of the interface velocity V_n and the gas velocity $u_{G,n}$ at the poles and the equator.

Due to evaporation, the velocity at the interface between the two phases differs, as reported in Figure 20 that shows the temporal evolution of the normal component of the interface velocity V_n and gas velocity ($u_{G,n}$) at the equator and the poles. For a maximum prolate or oblate shape ($S_t = 0$), the interface velocity is almost zero (Eqn. 5.14), since S_t is dominant and the radius change rate R_t for a low evaporation rate can be ignored. However, the gas velocity at the interface is not zero due to the evaporation. This difference between the interface velocity and the gas velocity may contribute to a vapour distribution different from that under quasi-steady conditions, and to the evaporation flux, which differs from that under quasi-steady conditions.

The effect of the moving interface on the evaporation characteristic can also be analysed through the amplitude of the evaporation rate. This depends on the initial droplet deformation, which also affects the phase shift between the evaporation rate and droplet oscillation. Tab. 4 lists the tests of different initial droplet deformations. Test series A1-A4 are of an initial prolate shape, while test series B1-B4 of an initial oblate shape have the same surface area corresponding to A1-A4. Figure 21 shows the temporal evolution of the dimensionless evaporation rate in tests A1-A4 and B1-B4. The amplitude

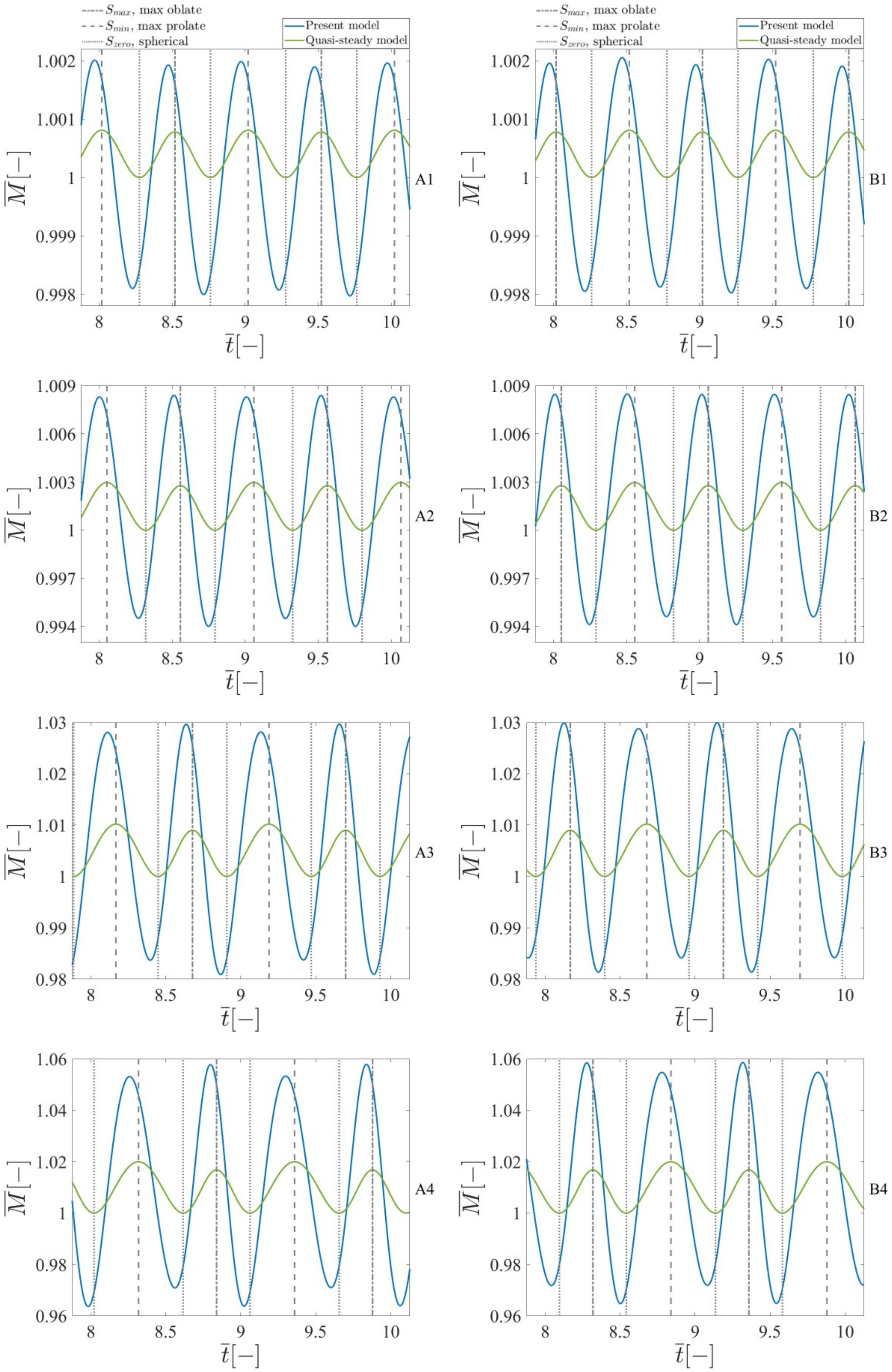

Figure 21: Temporal evolution of the dimensionless evaporation rate in tests A1-A4 (left column) and B1-B4 (right column).

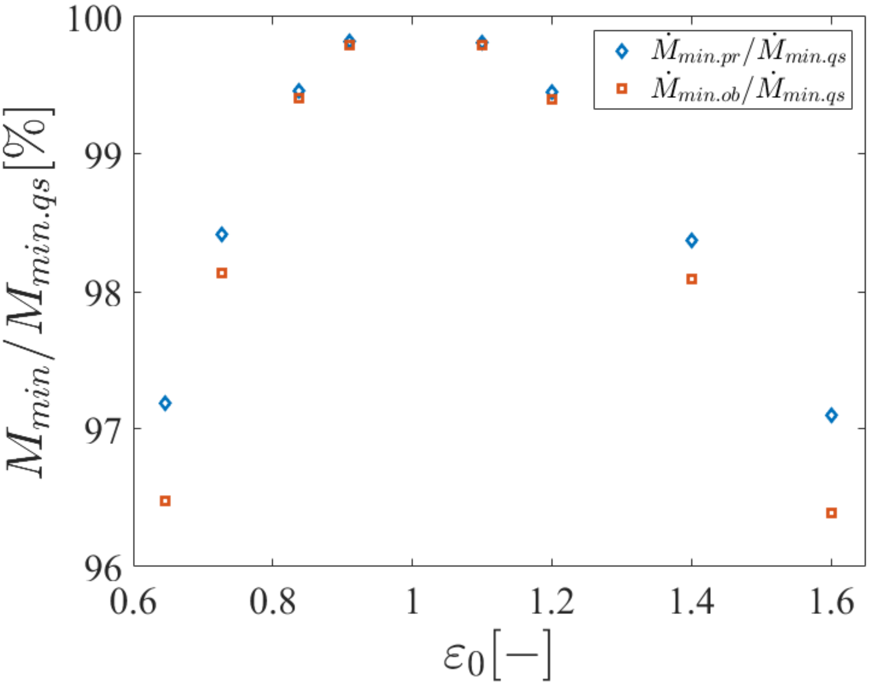

Figure 22: The ratio of the minimum evaporation rate $\dot{M}_{min}$ (in a prolate shape $\dot{M}_{min.pr}$ and an oblate shape $\dot{M}_{min.ob}$) to that under quasi-steady conditions $\dot{M}_{min.qs}$, with respect to different initial droplet shape ε_0.

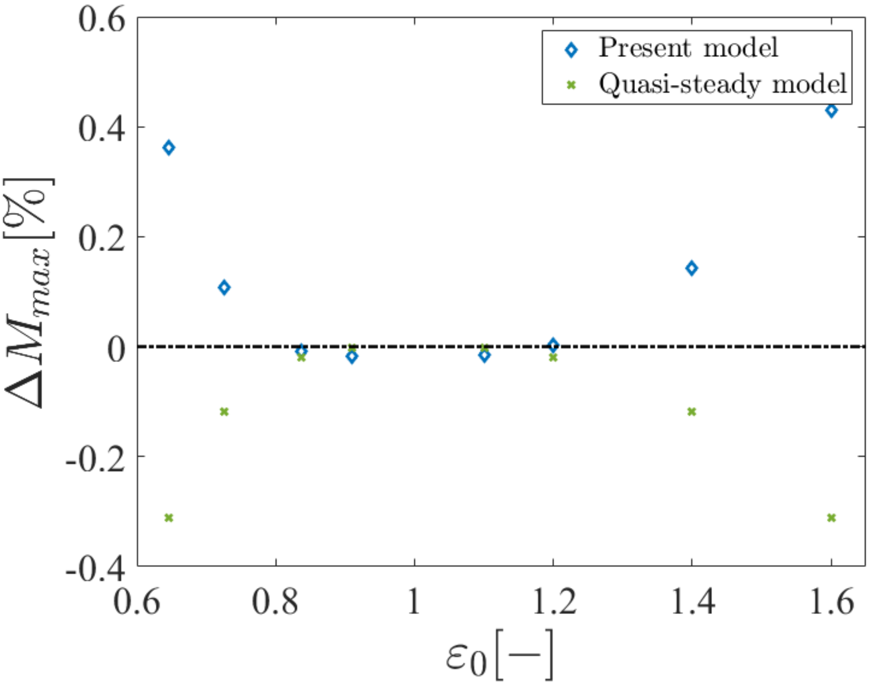

Figure 23: Relative difference $\Delta\dot{M}_{max} = \frac{\dot{M}_{max.ob}-\dot{M}_{max.pr}}{\dot{M}_{max.pr}}$ between the maximum evaporation rate in an oblate shape $\dot{M}_{max.ob}$ and a prolate shape $\dot{M}_{max.pr}$, with respect to the initial droplet deformation ε_0.

Table 4: Simulations of different initial droplet shape S_0 (ε_0)

$S_0 = -0.1736$ $\varepsilon_0 = 1.1$ test A1	$S_0 = -0.3056$ $\varepsilon_0 = 1.2$ test A2	$S_0 = -0.4898$ $\varepsilon_0 = 1.4$ test A3	$S_0 = -0.6094$ $\varepsilon_0 = 1.6$ test A4
$S_0 = 0.2066$ $\varepsilon_0 = 0.9104$ test B1	$S_0 = 0.4253$ $\varepsilon_0 = 0.8376$ test B2	$S_0 = 0.8943$ $\varepsilon_0 = 0.7266$ test B3	$S_0 = 1.3986$ $\varepsilon_0 = 0.6457$ test B4

and phase of the evaporation rate and the effect of the initial deformation on them are discussed in the following.

For steady spheroids, the evaporation rate always takes the minimum $\dot{M}_{min.qs}$ for a spherical shape, and $\dot{M}_{min.qs}$ is a constant value, since the decrease in droplet radius within a couple of periods is negligible (see Eqn. 5.13). Figure 22 shows the ratio of the minimum evaporation rate $\dot{M}_{min}$ (in a prolate shape $\dot{M}_{min.pr}$ and an oblate shape $\dot{M}_{min.ob}$) to that under quasi-steady conditions $\dot{M}_{min.qs}$, as a function of the initial deformation ε_0. For an oscillating droplet, the minimum of the evaporation rate $\dot{M}_{min}$ is lower than that predicted under quasi-steady assumptions $\dot{M}_{min.qs}$ (also refer to Figure 21), and the minimum, appearing in a prolate shape $\dot{M}_{min.pr}$, is always higher than that in an oblate shape $\dot{M}_{min.ob}$. As the droplet deformation increases, the difference between the minimum evaporation rate $\dot{M}_{min}$ and that under quasi-steady conditions $\dot{M}_{min.qs}$, and the difference between $\dot{M}_{min.pr}$ and $\dot{M}_{min.ob}$, both increase.

For a steady spheroid, the maximum of the evaporation rate in a prolate shape $\dot{M}_{max.pr.qs}$ is always higher than that in an oblate shape with the same surface area $\dot{M}_{max.ob.qs}$ (see Eqn. 5.13 and Eqn. 3.56). As the deformation increases, this difference also increases. For an oscillating droplet, the maximum evaporation rate $\dot{M}_{max}$ is always higher than that predicted under quasi-steady assumptions $\dot{M}_{max.qs}$ (refer to Figure 21). For oscillating droplets of small initial deformation, such as tests A1 and B1, the maximum evaporation rate in a prolate shape $\dot{M}_{max.pr}$ is also higher than that in an oblate shape $\dot{M}_{max.ob}$. But, for large initial deformations (tests A3, B3, A4, and B4), the maximum evaporation rate in a prolate shape $\dot{M}_{max.pr}$ is lower than that in an oblate shape $\dot{M}_{max.ob}$, by observing the data in Figure 23 that depicts the relative difference $\Delta\dot{M}_{max} = \frac{\dot{M}_{max.ob}-\dot{M}_{max.pr}}{\dot{M}_{max.pr}}$ for different initial droplet shapes ε_0 under unsteady and quasi-steady conditions. This transition happens close to tests A2 and B2. Both $\dot{M}_{max.pr}$ and $\dot{M}_{max.ob}$ increase for a larger droplet deformation (refer to Figure 21), but the increase of $\dot{M}_{max.ob}$ is faster. The minimum and maximum of the evaporation rate in test series A and B with the same initial surface coincide well, which implies that the evaporation rate amplitude depends on the initial deformation, regardless of whether it is a prolate or oblate shape.

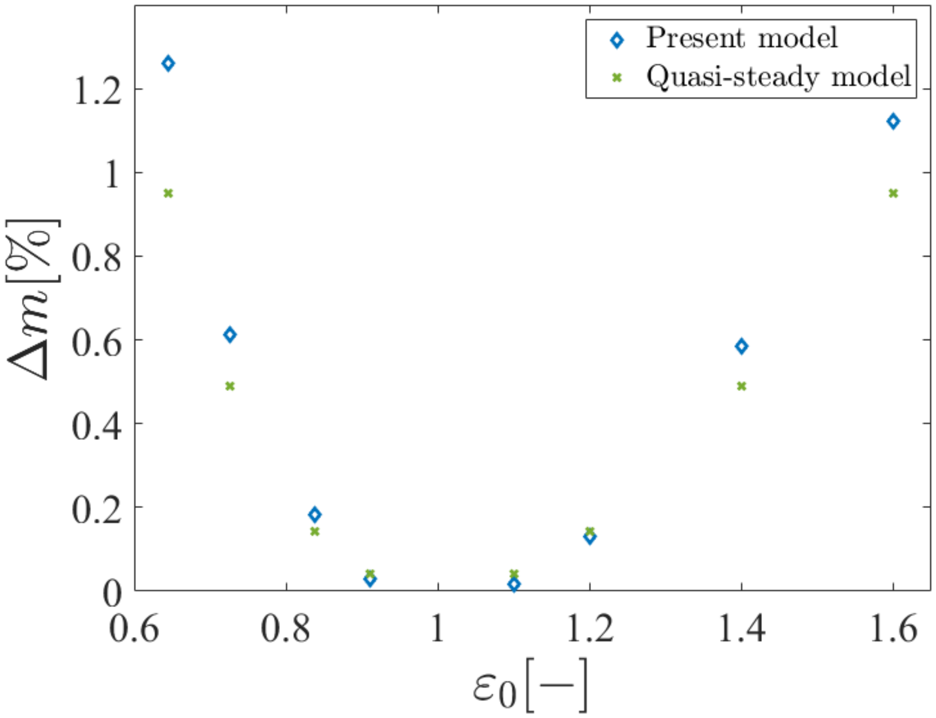

Figure 24: Dimensionless mass loss Δm within one period with respect to the initial droplet deformation ε_0, compared with that obtained under quasi-steady conditions.

In addition, the effect of a moving interface is taken into account by measuring the droplet mass loss within one period. Figure 24 shows the mass loss within one period $\Delta m = \frac{\int_t^{t+\Delta T} \dot{M} dt - \int_t^{t+\Delta T} \dot{M}_{sph} dt}{\int_t^{t+\Delta T} \dot{M}_{sph} dt}$, as a function of the initial aspect ratio ε_0, where $\dot{M}_{sph}$ represents the evaporation rate of a spherical droplet with the same surface area under the same evaporating condition. Δm of an oscillating droplet is in comparison to Δm_{qs} predicted by the analytical model under quasi-steady assumptions. For small droplet deformations, the mass loss Δm predicted by the present model is close to that by the quasi-steady model Δm_{qs}. Both the mass loss and the difference $\Delta m - \Delta m_{qs}$ increase with an increasing initial droplet deformation. The relative difference between Δm and Δm_{qs} is evident for a large droplet deformation. Its effect on the droplet lifetime can be expected for a large droplet deformation, because this difference accumulates with time. After many periods, the radius predicted by both methods differs. It is also worth noting that the decrease in the droplet radius is no longer negligible, as well as its effect on the oscillation dynamics, when oscillation periods is large and the decrease in the radius accumulates. In the present work, the decrease in radius is ignored. The radius decreases by less than 0.05% after five oscillation periods. A slight difference in the mass loss between test series A and B with the same initial droplet surface is observed, since the mass loss is evaluated in the tenth period and is still under the effect of the initial droplet shape. A later period is not chosen to avoid high computational time, as well as the evident decrease in the droplet radius, which can lead to different oscillation dynamics.

Table 5: Oscillation frequency in all tests

	A1, B1	A2, B2	A3, B3	A4, B4
angular frequency $[1/s]$	2015.6	2006.8	1978.5	1942.6

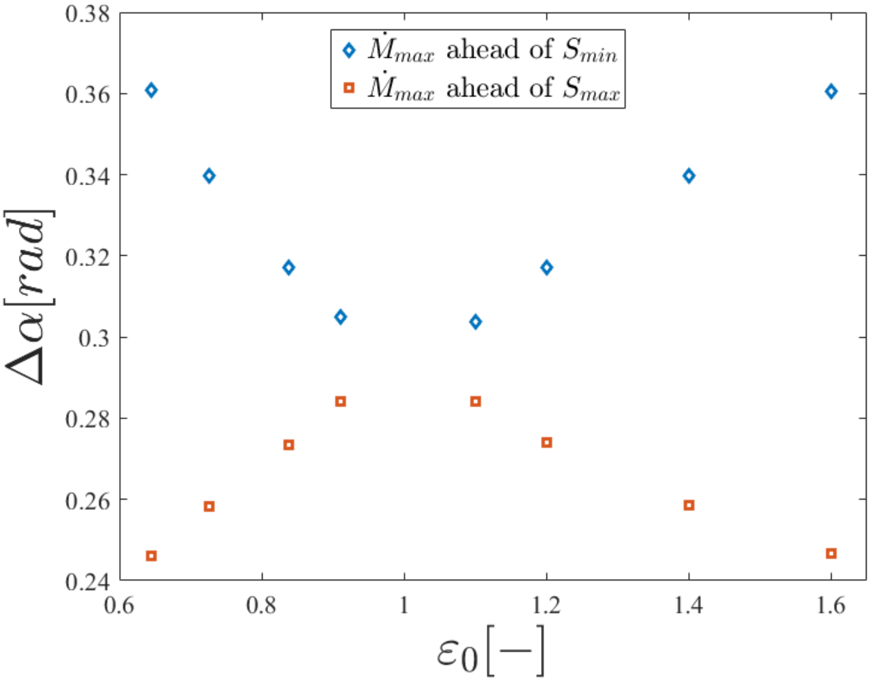

Figure 25: Phase shift of the peak of the evaporation rate $\dot{M}_{max}$ ahead of the maximum prolate (S_{min}) and oblate (S_{max}) shape, with respect to the initial droplet deformation ε_0.

The initial droplet aspect ratio ε_0 also has an effect on the phase of the evaporation rate. It is known that the oscillation frequency decreases with an increasing initial droplet deformation [20,29,30], as listed in Tab. 5. The frequencies of the evaporation rate are identical to the oscillation frequencies in each test, respectively. As mentioned above, there exists a phase shift between the peak of the evaporation rate and the maximum prolate or oblate shape, and between the minimum of the evaporation rate and a spherical shape. The phase shift $\Delta\alpha$ is characterized by the maximum evaporation rate $\dot{M}_{max}$ ahead of the maximum prolate (S_{min}) or oblate (S_{max}) shape, as shown in Figure 25, and by the minimum evaporation rate (in a prolate $\dot{M}_{min.pr}$ or oblate $\dot{M}_{min.ob}$ shape) ahead of the spherical shape ($S = 0$), as reported in Figure 26. With an increasing initial droplet deformation, the phase shift $\Delta\alpha$ between the peak of the evaporation rate $\dot{M}_{max}$ and the maximum prolate (S_{min}) shape increases, while that between $\dot{M}_{max}$ and (S_{max}) decreases. When the initial deformation approaches a spherical shape $\varepsilon_0 = 1$, both phase shifts coincide. The phase shift of the minimum evaporation in a prolate shape ($\dot{M}_{min.pr}$) ahead

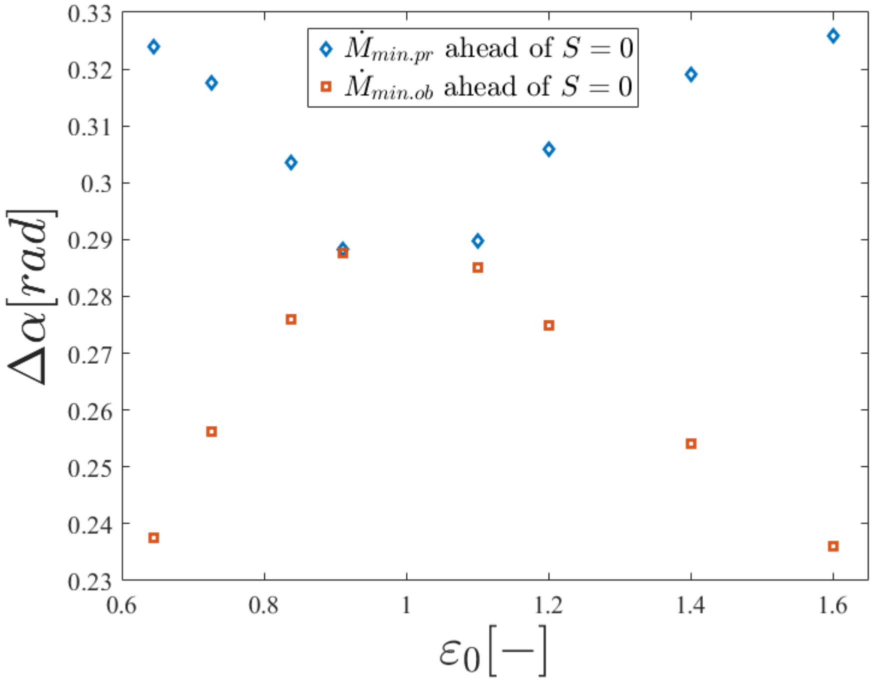

Figure 26: Phase shift of the minimum the evaporation rate (in a prolate $\dot{M}_{min.pr}$ or oblate $\dot{M}_{min.ob}$ shape) ahead of the spherical shape (S = 0), with respect to the initial droplet deformation ε_0.

of a spherical droplet shape ($S = 0$) increases as the initial deformation increases. In contrast, the phase shift of the minimum evaporation rate in an oblate shape ($\dot{M}_{min.ob}$) ahead of a spherical droplet shape ($S = 0$) decreases. As the initial deformation approaches $\varepsilon_0 = 1$, these two phase shifts become closer. For an initial prolate or oblate shape with the same surface area, the phase shifts are similar. Considering together with the close amplitude of the evaporation rate in test series A and B, it can be concluded that the evaporation rate depends on the initial deformation, regardless of whether the droplet is prolate or oblate.

Table 6: Simulation under different evaporating conditions

	$T_L\ [K]$	$\rho_G\ [kg/m^3]$	$\chi_s\ [-]$
A2^L	336.15	0.9601	0.1537
A2^H	368.15	0.6555	0.7595

In the present work, the droplet temperature is assumed to be constant, as well as the vapour mass fraction at the surface. The effect of the evaporating conditions on the evaporation behaviour of an oscillating droplet is discussed here. Test A2^H of a higher evaporating temperature $T_L = 368.15K$ and test A2^L of a lower evaporating temperature $T_L = 336.15K$ are listed in Tab. 6. The evaporation rate of test A2^H is more than five times that of test A2^L, as reported in Figure 27. Despite such different evaporating rates, their profiles are similar. Figure 28 shows the temporal profiles of the dimensionless evaporation rate. Under different evaporating conditions, the profiles of the dimensionless evaporation

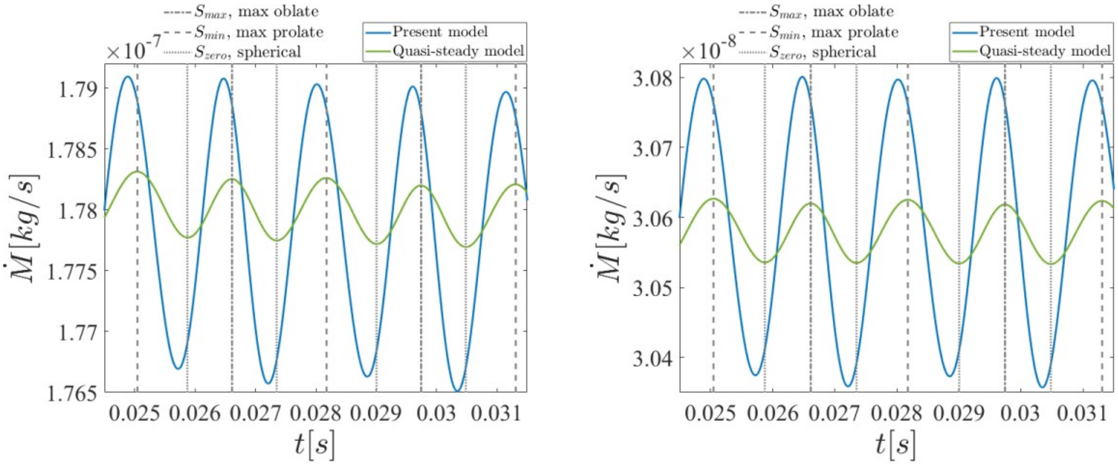

Figure 27: Temporal evolution of the evaporation rate in tests A2^H (left) and A2^L (right).

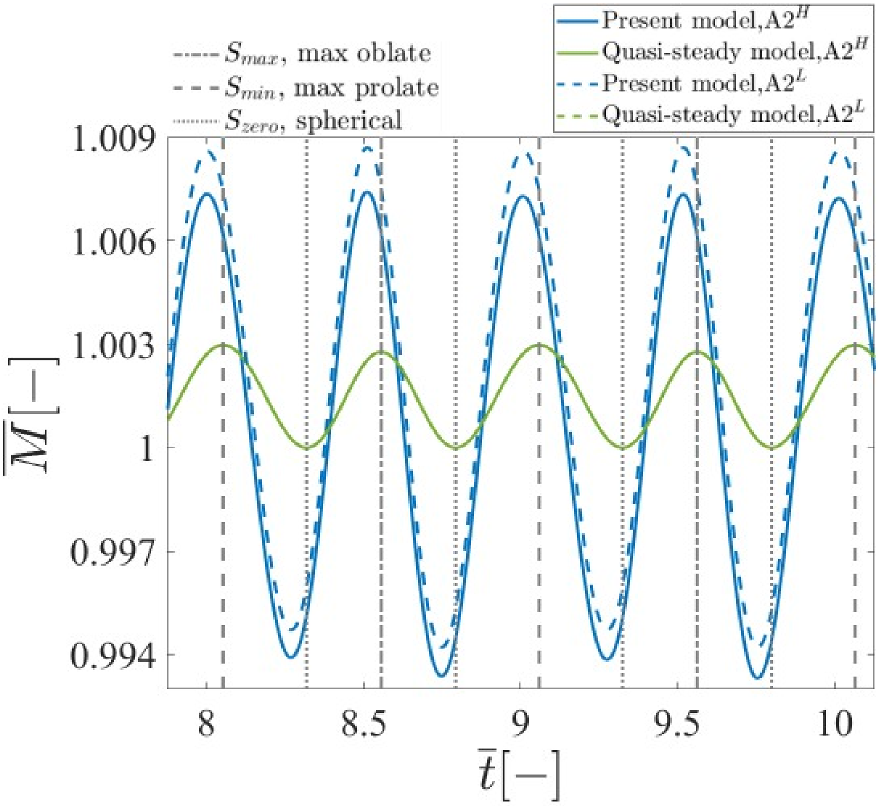

Figure 28: Temporal evolution of the dimensionless evaporation rate in tests A2^H (solid line) and A2^L (dash line).

rate predicted by the quasi-steady model coincide. The amplitude of the dimensionless evaporation rate for an oscillating droplet under different evaporating conditions is slightly different. The phase shift between the evaporation rate and droplet oscillation also has only a very small difference. Therefore, the evaporating conditions only have a slight influence on the evaporation behaviour of an oscillating droplet. This verifies the assumption of a constant droplet temperature when focusing on the effect of a moving interface on the evaporation behaviour.

5.2 Direct Numerical Simulation of the Evaporation of an Oscillating Droplet using FS3D

This section summarises the investigation of the evaporation of an oscillating droplet by DNS (direct numerical simulation). The in-house code FS3D of the institute ITLR in Stuttgart is employed, which is developed for incompressible multiphase flows (Section 3.9). This code solves mass and momentum conservation equations, as well as the energy equation. The flow is assumed to be incompressible. No turbulence model is adopted, and assumptions of fixed droplet temperature and vapour mass fraction at the surface, potential flows, and spheroidal droplet shape in the analytical/numerical model introduced in Section 5.1 do not hold in DNS. Two validation cases are performed to verify the capability of FS3D to predict the evaporation of an oscillating droplet. Then the grid convergency study is discussed for the main simulations in the present work.

5.2.1 Code Validations

Since the experimental or theoretical data for the evaporation of an oscillating droplet are limited until now, the validation of the capability of the code FS3D is split into two independent validation tests. One validation considers the droplet oscillation without evaporation ($Pe \to \infty$). The other one studies the evaporation of spheroidal droplets under quasi-steady conditions ($Pe \to 0$). In the latter validation case, a droplet surface is assumed to be still.

5.2.1.1 Validation of the Capability of FS3D for Droplet Oscillation without Evaporation

In the first validation case, we investigate an oscillating droplet without evaporation. A comparison between the numerical results predicted by FS3D and the available data in the literature [20, 29, 30]. For an oscillating droplet, an asymmetry in the time spent in the prolate and oblate shapes in each period is found [20, 30], as observed in Figure 29 that reports the percentage of time spent by the droplet in the prolate shape within one period increasing as the aspect ratio ε. The numerical results

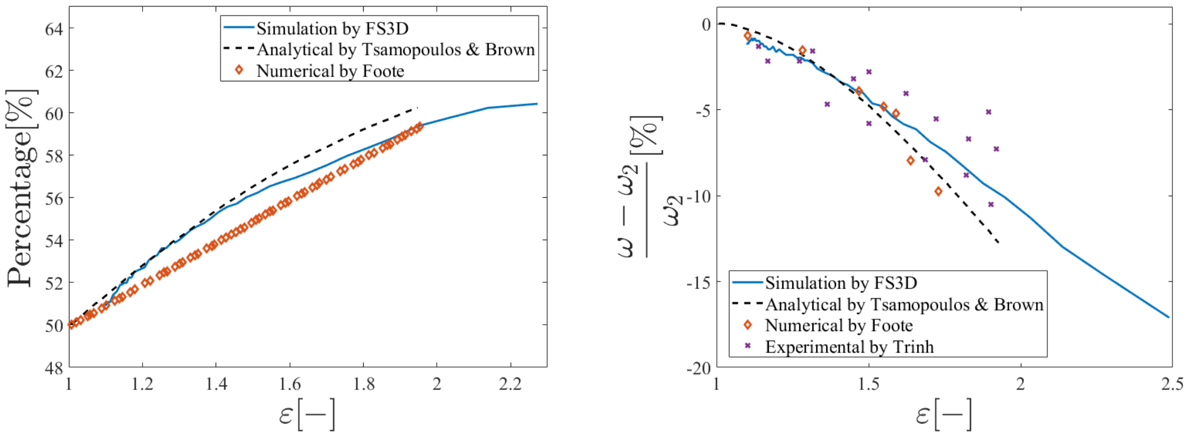

Figure 29: Validation of FS3D for an oscillating droplet without evaporation, by comparison of the results predicted by FS3D to the analytical [30], numerical [20], and experimental [29] data in literature. Left, the percentage of the time spent in a prolate shape in one period with respect to the aspect ratio; Right, the deviation of the droplet oscillation frequency ω from the angular frequency in the second mode ω_2 with respect to the aspect ratio.

by FS3D are in good agreement with the analytical [30] and numerical [20] results. The effect of the oscillation amplitude on the oscillation frequency is summarized in [20, 29, 30]. Referring to Figure 29, the deviation of the droplet oscillation frequency ω from the angular frequency in the second mode $\omega_2 = \sqrt{\frac{8\sigma}{\rho_L R^3}}$ increases as the aspect ratio. These results by FS3D have a similar trend with the analytical [30], numerical [20], and experimental [29] results. This validation case verifies the capability of FS3D to predict the droplet oscillation without evaporation.

5.2.1.2 Validation of the Capability of FS3D for Evaporation of Spheroidal Droplets under Quasi-steady Assumptions

The second validation case focuses on the evaporation of spheroidal droplets under quasi-steady assumptions, which was conducted by Reutzsch [123]. Figure 30 reports the spatial distribution of the non-dimensional evaporation flux $\hat{n}_{ev} = n_{ev}(\frac{\dot{M}}{4\pi R^2})^{-1}$ over the droplet surface $\eta = cos(\theta)$. In this section 5.2, θ is the polar angle in a spherical coordinate system, and $\eta = cos(\theta)$ is defined as the cosine of the polar angle of a point at the droplet surface. $\eta = 1$ refers to the upper pole, $\eta = -1$ corresponds to the lower pole, while $\eta = 0$ is the equator. By Eqn. 5.2, the dimensionless evaporation flux by the analytical model under quasi-steady assumptions is $\hat{n}_{ev.qs} = (R^2\kappa_G)^{1/4}$. For a prolate droplet, $\hat{n}_{ev.qs}$ at the poles is higher than that at the equator. In contrast, an oblate droplet has a higher dimensionless $\hat{n}_{ev.qs}$ at the equator. The spatial distribution of the evaporation flux predicted by FS3D is consistent with the analytical results [71]. Considering both validation cases, FS3D is assumed to be capable of simulating the evaporation of an oscillating droplet, which releases the quasi-steady assumptions.

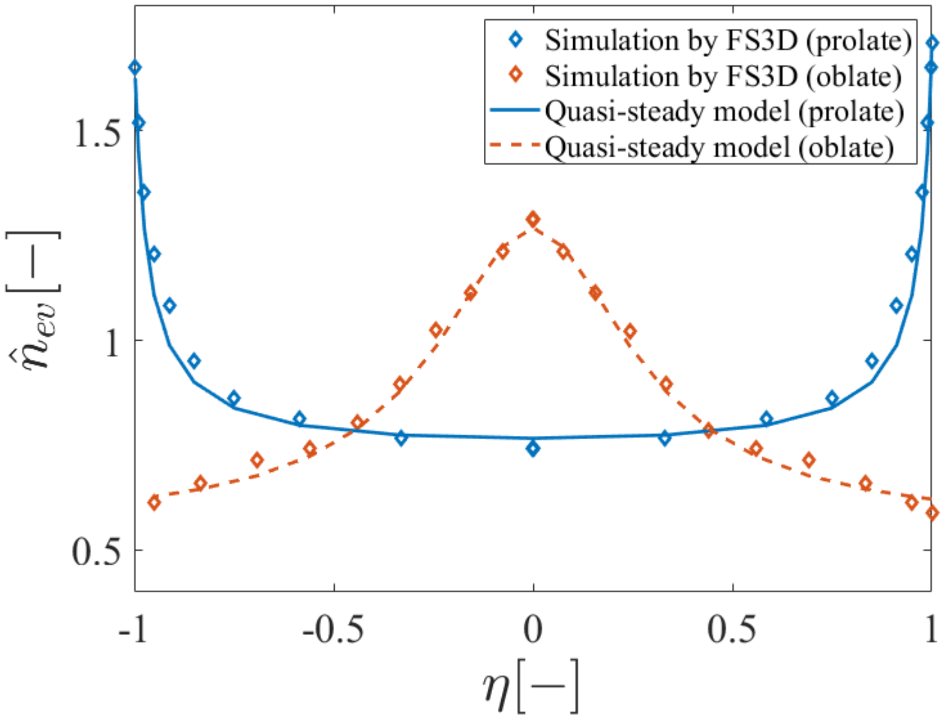

Figure 30: Validation of FS3D for the evaporation of spheroids under quasi-steady conditions. The spatial distribution of non-dimensional evaporation flux $\hat{n}_{ev}$ over the droplet surface η.

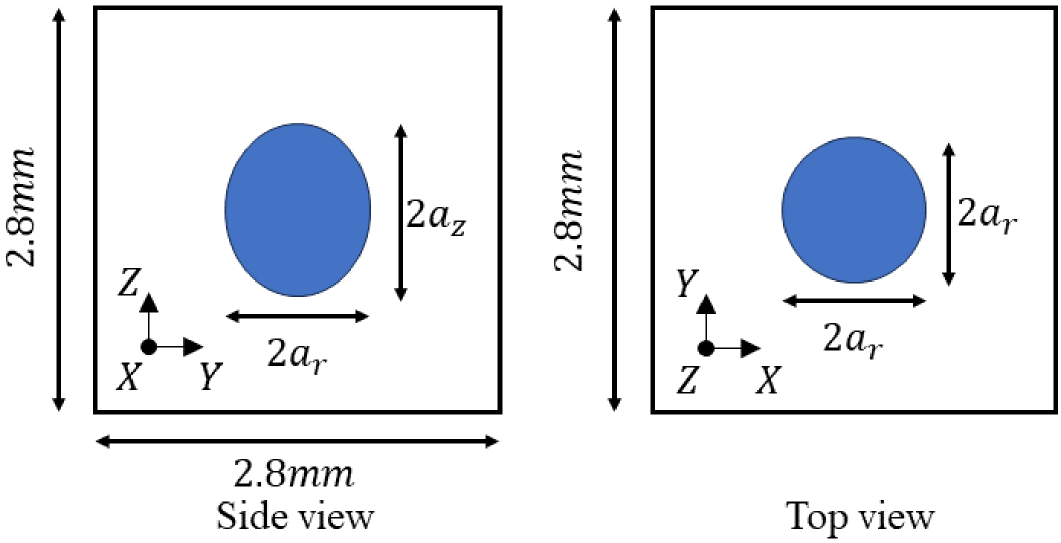

Figure 31: Computational domain.

5.2.2 Computational Settings and Grid Resolution Convergence Study

The computational domain of dimensions 2.8^3 mm^3 is shown in Figure 31. The corresponding cell numbers are 128^3. In the middle of the domain, a water droplet of an initial prolate shape of semi-axis $a_{r,0}$ and $a_{z,0}$ oscillates and evaporates in air. Tab. 7 lists the initial semi-axis $a_{r,0}, a_{z,0}$ (initial aspect ratio $\varepsilon_0 = 1.2$), binary diffusivity coefficient of the vapour in air D, air pressure p_0, initial liquid $T_{L,0}$ and gas $T_{G,0}$ temperature, surface coefficient σ, liquid μ_L and gas μ_G dynamic viscosity. The small initial temperature difference can reduce the effect of the initial temperature difference on the vapour distribution, and thus the computational efforts. Tests with different initial temperature differences are conducted, and similar results are obtained. The continuous boundary conditions for all boundaries are set. The initial vapour distribution in the gaseous phase is set to be that given under steady conditions, described by Eqn. 5.1, to reduce the computational time. Otherwise, much computational time is wasted to achieve a stable varying vapour distribution.

Table 7: Parameter settings

$a_{r,0}$ $[m]$	$a_{z,0}$ $[m]$	D $[m^2/s]$	p_0 $[Pa]$	$T_{L,0}$ $[K]$
0.5×10^{-3}	0.6×10^{-3}	28.45×10^{-6}	0.965×10^5	351
$T_{G,0}$ $[K]$	σ $[mN/m]$	μ_L $[Pa \cdot s]$	μ_G $[Pa \cdot s]$	
350.8	76.40	3×10^{-3}	18.2×10^{-6}	

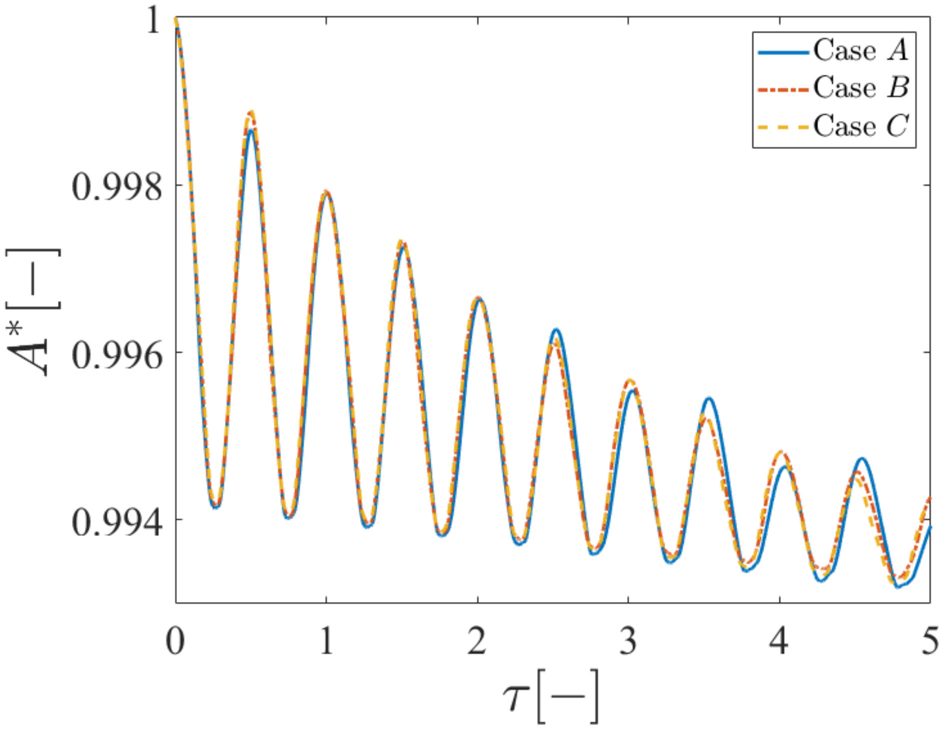

Figure 32: Normalized droplet surface area A^* with non-dimensional time τ for test cases with various cell numbers: $A : 64^3$, $B : 96^3$ and $C : 128^3$

The grid convergence study presented here is performed for the main simulations of oscillating evaporating droplets. Three test cases are conducted, with various cell numbers: case $A : 64^3$, case $B : 96^3$, and case $C : 128^3$. Figure 32 depicts the evolution of the droplet surface area A^*, which is normalized by the initial droplet surface area, with respect to the non-dimensional time τ for three cases. The dimensionless time is $\tau = \frac{t}{t_{period}}$, where the averaged period of five oscillation periods $t_{period} = 3.138\ ms$ is used. The deviation of case A from C is evident since $\tau = 3$. While cases B and C coincide well, with the relative difference about 7% in the fifth period. By considering the computational effort and accuracy, the cell numbers 128^3 in case C is assumed in the present case to be sufficient.

5.2.3 Results from FS3D Simulations and Discussions

The simulation results of the evaporation of an oscillating droplet by FS3D are presented and discussed in this section. Both viscosity and temperature variation are considered in the simulations.

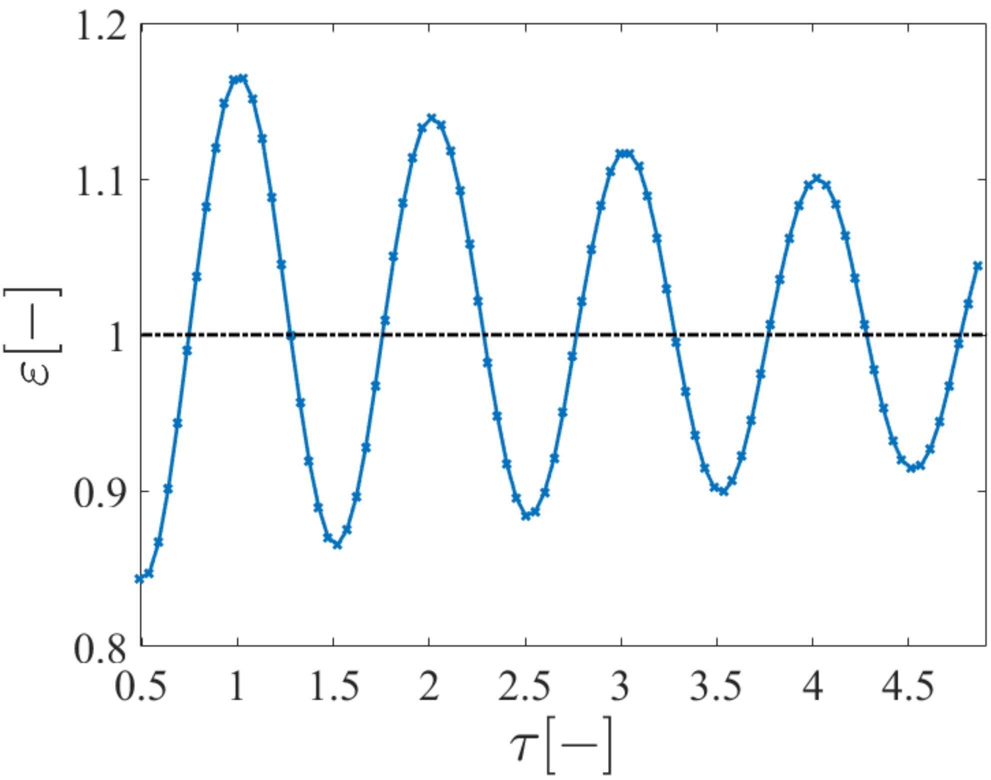

Figure 33: Evolution of the aspect ratio with respect to non-dimensional time, predicted by FS3D.

Figure 33 shows the evolution of the aspect ratio with respect to the non-dimensional time. Due to the viscous dissipation, the oscillation is damped. The initial half period is not taken into account, to avoid the instability in the start. The evaporation rate $\dot{M}$ decreases with time, as observed in Figure 34. As the droplet evaporates, the radius reduces. And this can cause the falling evaporation rate. But,

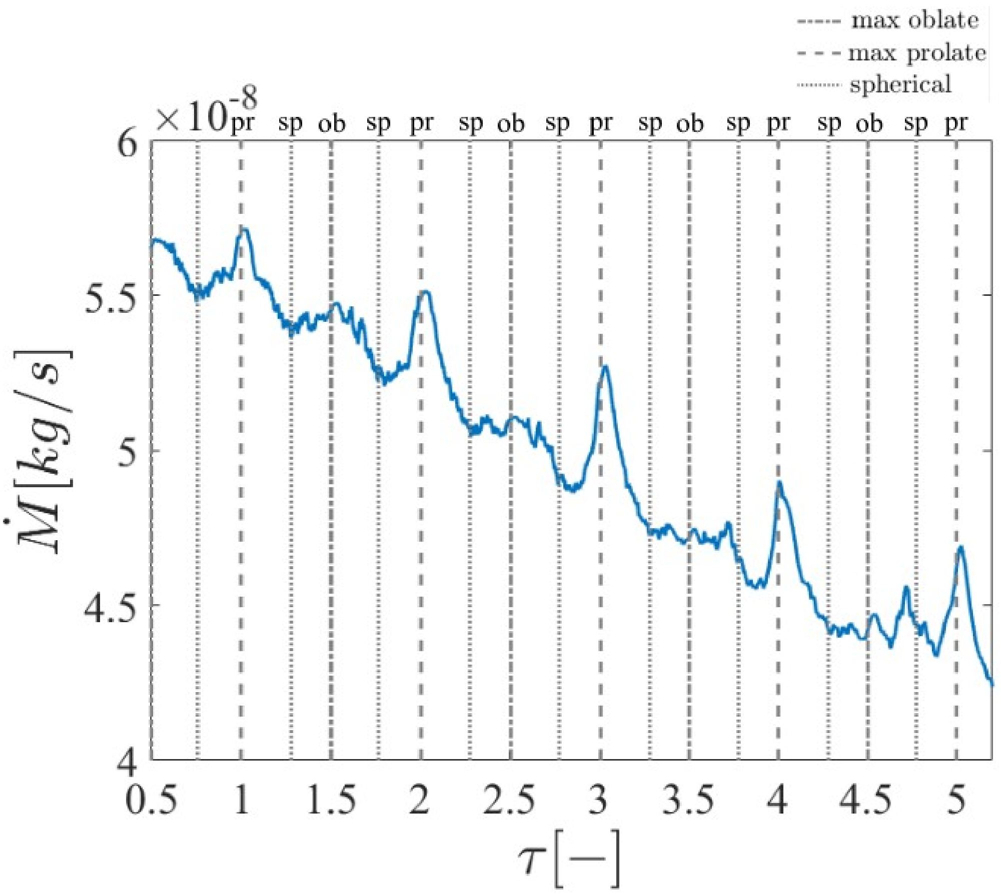

Figure 34: Evolution of the evaporation rate with respect to non-dimensional time.

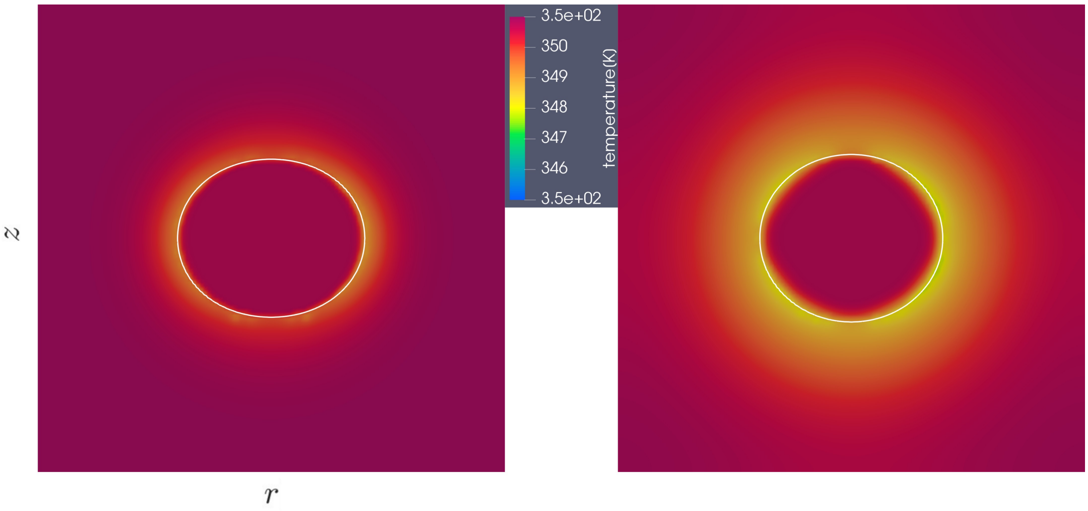

Figure 35: Temperature distribution from side view at two times, $\tau = 0.4908$ (left), $\tau = 3.4353$ (right). The white line represents the position of the interface.

in the present case, this effect is negligible, since the decrease in radius in several periods is very tiny. The main reason for this decreasing evaporation rate can be ascribed to the decreasing temperature at the interface due to the evaporation. The saturated vapour mass fraction at the interface is sensible to the variation of temperature. As the interface temperature goes down, the vapour saturated mass fraction decreases fast, and this causes the falling evaporation rate. Due to the large latent heat of evaporation, the temperature at the interface goes down fast, as reported in Figure 35, which shows the temperature distribution at two times, $\tau = 0.4908$ and $\tau = 3.4353$. The interface temperature and gas temperature in the vicinity of the interface decrease fast, while the effect of the evaporation on the droplet temperature is limited in a thin boundary layer since the thermal diffusivity $\frac{\lambda}{\rho C_p}$ of the liquid is much smaller than that of the gas. The thermal boundary layer in the liquid phase is much thinner than that in the gaseous phase. The heat flux inside the droplet is much higher than that in the gaseous phase due to the thin thermal boundary layer (large temperature gradient) and large thermal conductivity. In fact, the interface temperature is not uniform and varies with time since the spatial and temporal varying evaporation flux. The results predicted by the quasi-steady model under the same evaporating conditions are not set as a comparison, since the time-varying and non-uniform droplet temperature. Although the evaporation rate has some fluctuations, a phase shift is observed between the evaporation rate and the droplet oscillation. This can also be understood as the result of a different evaporation flux over the droplet surface, as described in the last section 5.1.3.2. But the peak of the evaporation rate is behind the maximum prolate shape. The evaporation rate in a prolate shape is evidently higher than that in an oblate shape, which is strongly different from the results under quasi-steady assumptions for a small droplet deformation.

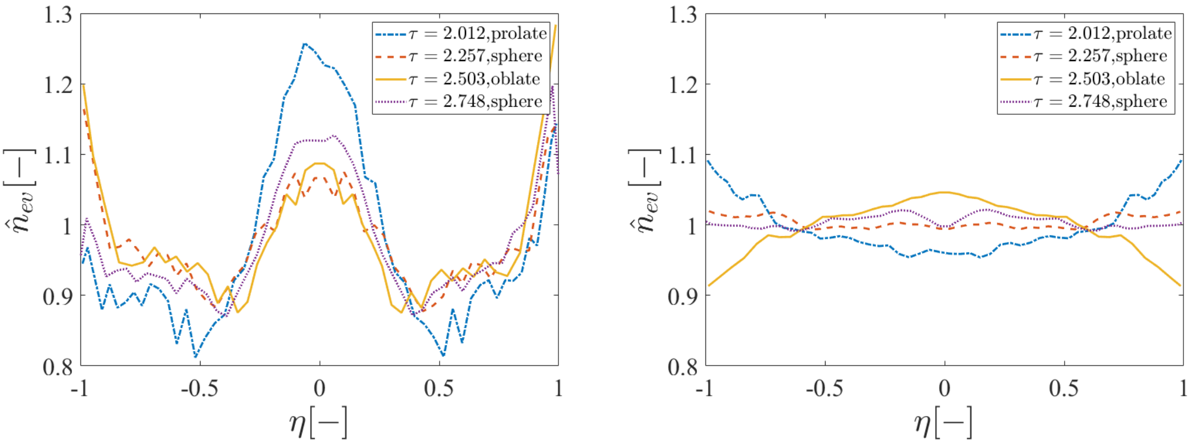

Figure 36: Spatial distribution of evaporation flux over the droplet surface within one period by FS3D simulations (left), compared with the results by the analytical model under quasi-steady assumptions (right).

Table 8: Different locations at surface

	A	*B*	*C*	*D*	*E*	*F*	*G*	*H*	*I*	*J*
polar angel θ	0°	20°	30°	40°	50°	60°	65°	70°	75°	90°

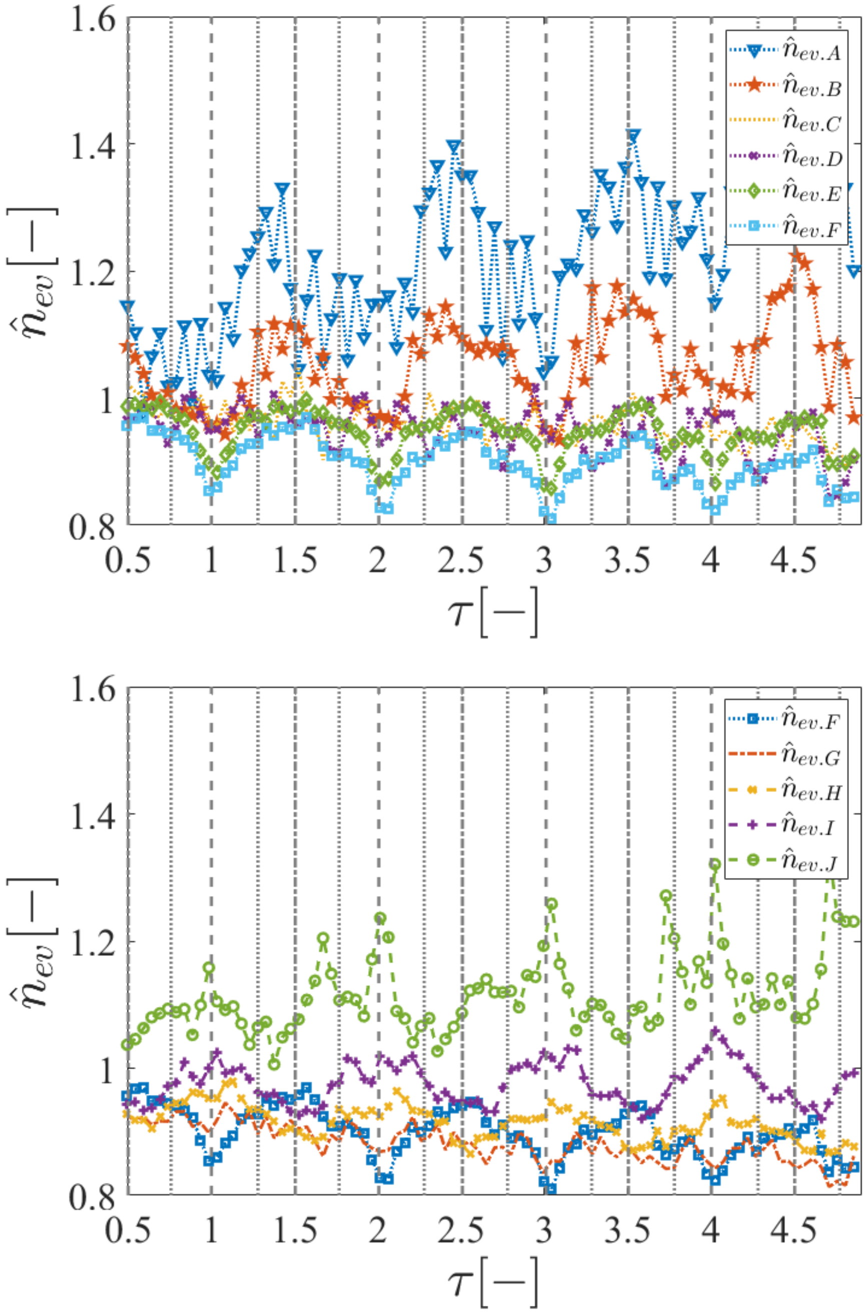

Figure 37: Temporal evolution of non-dimensional evaporation flux at different surface locations, from A ($\theta = 0°$) to J ($\theta = 90°$), by FS3D simulations.

Figure 36 compares the spatial distribution of non-dimensional evaporation flux $\hat{n}_{ev} = n_{ev}(\frac{\dot{M}}{4\pi R^2})^{-1}$ over the droplet surface at various η within one period predicted by FS3D with that by the analytical model under quasi-steady assumptions. Under quasi-steady assumptions, the non-dimensional evaporation flux is $\hat{n}_{ev.qs} = (R^2 \kappa_G)^{1/4}$ by Eqn. 5.2 and it depends on the surface curvature (droplet shape). A prolate droplet has the highest $\hat{n}_{ev}$ at the poles, while an oblate one has the highest at the equator. But the simulation results for an oscillating droplet show strongly different characteristics. The evaporation flux is higher at the equator and the poles, regardless of the droplet shapes. Different surface locations are listed in Tab. 8. The temporal evolution of the evaporation flux at these locations is shown in Figure 37. At different locations, the evaporation flux reaches the peak at different times. The data at the poles A and equator J have more fluctuations due to the large movement and fast variation of the curvature there. In the region near the poles, such as locations B, F, the flux achieves the peak for a maximum oblate shape and has the minimum for a maximum prolate shape. While in the region near the equator, such as locations H, I, the flux reaches the peak for a maximum prolate shape and has the minimum for a maximum oblate shape. This transition occurs at location G. This characteristic is strongly different from the results by the analytical model under quasi-steady assumptions, reported in Figure 38. The flux reaches the peak for a maximum prolate shape from A to E, where the droplet surface curvature is larger in a prolate shape. The flux achieves the peak for a maximum oblate shape from E to J, where an oblate droplet has a larger surface curvature.

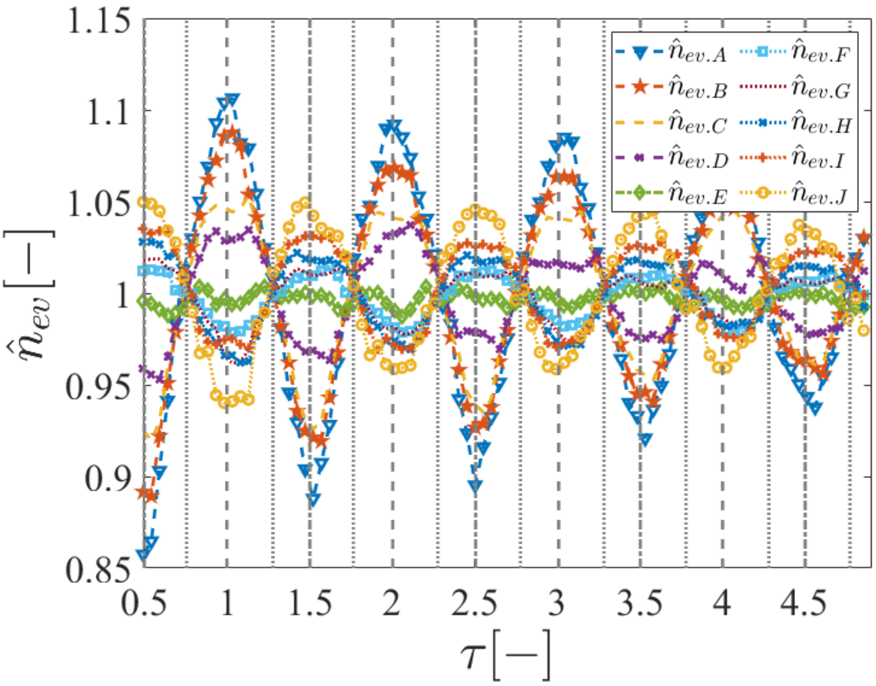

Figure 38: Temporal evolution of non-dimensional evaporation flux by the analytical model under quasi-steady assumptions, at different surface locations.

The evaporation rates predicted by FS3D (Figure 34) and by the analytical/numerical model in Section 5.1 (Figure 18) are on the same scale. In FS3D, the thermal physical properties are estimated locally at each moment. The energy equation is solved, and temperature variation is considered. Thus, the surface temperature decreases as the droplet evaporates. Then, the decreasing saturated vapour mass fraction at the surface leads to a sinking evaporation rate. However, in the analytical/numerical model in Section 5.1, the surface temperature is assumed to be constant. Thus, the evaporation rate in Figure 18 does not goes down. Due to the spatially non-uniform evaporation flux, the local heat flux varies with location in FS3D. The droplet surface temperature is therefore non-uniform, which then affects droplet evaporation. Local surface temperature and evaporation flux are coupled, which may lead to the different evaporation flux profiles in FS3D and the analytical/numerical model (Figure 15 and Figure 36). The different flux profiles lead to different phase shifts between the evaporation rate and droplet oscillation. In the analytical/numerical model, we assumed that the droplet temperature is fixed and has only a slight effect on the evaporation behaviour. But the evaporation flux and surface temperature are coupled, it may be one part of further work.

Chapter 6. Conclusions and Outlook

Droplet evaporation under largely different conditions, such as non-spherical shapes, droplet pairs/arrays, suspended/sessile droplets, non-uniform temperature, multicomponents, and so on, has been investigated over more than one century. However, in the past work on droplet evaporation, the steady mass/heat transfer through the interface is always assumed (quasi-steady assumptions), and the droplet shape is usually assumed to be fixed, whether the droplet is prolate, spherical, or oblate. The evolution of the interface is often assumed to be much slower than the heat/mass diffusion through the interface. For an oscillating droplet, the possible effect of a moving interface has to be taken into account, and the quasi-steady assumption is released, which is investigated in the present work. The main task is to study the effect of the moving interface on the droplet evaporation characteristics. An analytical method is suitable for the present task, as it simplifies the secondary factors and focuses on what we are interested in. An in-house numerical code FS3D (Free Surface 3D), shared by the ITLR of University Stuttgart, and developed for DNS (direct numerical simulation) of multiphase flows, offers more details and another viewpoint on our research.

An analytical droplet oscillation model is first introduced. Two basic assumptions hold: a spheroidal droplet and potential flows. The assumed shape of spheroidal droplets provides great convenience in employing the prolate/spherical/oblate coordinate systems, which can be summarized as a generalized spheroidal coordinate system (ψ, η, φ) in a unified way. Therefore, it is very suitable for a droplet oscillating in a spheroidal shape. The droplet shape and this generalized spheroidal coordinate system are completely described by a time-varying deformation parameter, which can be numerically evaluated from a non-linear ODE describing the droplet energy conservation equation. In this time-varying generalized spheroidal coordinate system, the moving interface between the droplet and gas can be simply described at $\psi = 1$, i.e. the moving boundary problem is transformed to a fixed boundary one. The assumption of potential flow allows to derive the velocity field by solving a Laplace equation for the velocity potential, instead of solving the momentum equation. Solving the Laplace equation in this generalized spheroidal coordinate system, the velocity field in both phases can be given analytically. The simulation results for an oscillating droplet by the in-house code FS3D are used as a comparison to better show how these assumptions in the analytical model possibly deviate from the real situation. Inside the droplet, the velocity field obtained by the analytical model coincides very well with that from the simulations by FS3D. From the simulation results, in the gaseous phase, a vortex is observed where the droplet surface is almost still during the oscillation. This vortex is strong for a spherical droplet when the velocity is fast, and weak when the droplet approaches a maximum extended shape.

Besides the Laplace equation for the velocity potential, the species conservation equation in the gaseous phase is solved. The generalized spheroidal coordinate system is still employed. The present work mainly analyses the effect of a moving interface on the evaporation characteristics. Thus, additional simplifications have been made temporarily. The temperature distribution over the surface is assumed to be fixed and uniform, and the temperature dependence of the physical properties is therefore ignored. Gas density is assumed to be constant at each location, even though the vapour mass fraction varies spatially. The normal velocities within the two phases are discontinuous due to the evaporation. The evaporation flux is calculated in a diffusion form through the jump conditions. The instantaneous evaporation rate is evaluated by integration of the evaporation flux over the surface. The mass loss within one period can be obtained by integrating the evaporation rate over one period. Since the species conservation equation and the Laplace equation are coupled, they are numerically solved by a computational loop, using the General Form of PDE in COMSOL Multiphysics.

The results from the analytical model under quasi-steady assumptions are taken as a reference, by which the effect of a moving interface on the evaporation characteristics is better shown. The evaporation flux for an oscillating droplet has a similar tendency to that from the quasi-steady model, but is quantitatively different. The difference depends on both time and location. This difference leads to a phase shift between the evaporation rate and droplet oscillation. Under quasi-steady assumptions, the evaporation rate reaches the maximum values when the droplet has a maximal extended shape, and has a minimum for a spherical shape. But, for an oscillating droplet, the peak of the evaporation rate is ahead of the maximal extended shape (maximum prolate or oblate shape). The minimum of the evaporation rate is also ahead of the spherical droplet shape. The initial droplet deformation has an effect on the phase shift between the evaporation rate and droplet oscillation. Under the same evaporating conditions, the phase shift becomes larger as the initial droplet deformation increases, whether the droplet is prolate or oblate. The evaporating conditions also have an effect on the phase shift. A droplet of high temperature has a larger phase shift than one of low temperature. Under quasi-steady conditions, the minimum of the evaporation rate is attained for a spherical droplet. The peak of the evaporation rate corresponds to the maximum prolate/oblate shape. A prolate droplet has a higher evaporation rate than an oblate one with the same surface area. For an oscillating droplet, the minimum of the evaporation rate is always lower than the value under quasi-steady conditions. The maximum evaporation rate in a prolate shape is higher than that in an oblate shape when the initial aspect ratio is small. While the initial aspect ratio is over a threshold, the maximum evaporation rate in a prolate shape is lower than that in an oblate shape. The mass loss is investigated by integration of the evaporation rate over one period. For small initial droplet deformation, the mass loss of an oscillating droplet is close to that under quasi-steady conditions. For a large initial droplet deformation, an oscillating droplet has a higher mass loss than a droplet under quasi-steady conditions, and this difference becomes larger when increasing the oscillation amplitude.

The evaporation of an oscillating droplet is also numerically investigated by DNS (direct numerical simulation) with the numerical code FS3D. No assumptions are made, and the effect of temperature is taken into account. The evaporation flux by FS3D is different from that by the quasi-steady model, which is proportional to the fourth root of the local Gauss curvature. Regardless of the droplet shape, the outcomes of these simulations show a higher evaporation flux at the poles and the equator, and the evaporation flux depends on both time and location. It is also observed a phase shift between the evaporation rate and droplet oscillation. In these simulations, the evaporation rate continuously decreases with time, which can be attributed to the fast decrease in the droplet surface temperature due to the high value of the latent heat. The decrease in the surface temperature leads to a lower saturated vapour mass fraction at the interface. The effect of the decrease in the droplet radius can be ignored over only a few periods. The temperature dependence of the physical properties and saturated vapour mass fraction at the interface is not taken into account in the previous analytical/numerical evaporation model for an oscillating droplet. Therefore, it needs to be careful when comparing the evaporation rates by FS3D and the previous analytical/numerical model, but they are still on the same scale.

Outlook

Starting from an analytical droplet oscillation model, combined with the droplet evaporation, an analytical/numerical evaporation model for an oscillating droplet is proposed in this thesis. Many assumptions have been made temporarily, since our main focus is the effect of the moving interface on the droplet evaporation. But these assumptions may also have a crucial effect on the droplet evaporation. The varying droplet surface temperature should be taken into account in further work, due to the sensible temperature dependence of the saturated vapour mass fraction at the interface. This process can become very complex when the heat transfer is considered, since the evaporation rate, the droplet surface temperature, and the velocity field are coupled. The energy and species equations in the gaseous phase have a similar expression, but with different boundary conditions at the interface. And this would allow us to model the temperature variation in the gaseous phase using the same analytical/numerical model. The temperature equation inside the droplet can also be solved numerically. If identical normal liquid interface velocity and normal interface velocity are assumed due to the large density ratio of liquid and gas, the velocity field inside the droplet is decoupled from the evaporation, and its analytical solution is already known. In extreme conditions, e.g., when isothermal lines and streamlines coincide, the analytical solution of the temperature field inside the droplet may be possible. In the case of a water droplet in air, the thermal conductivity of the liquid is much larger than that of the gas, while the temperature diffusivity of the liquid is much lower than that of the gas. A thin thermal boundary layer inside the droplet is expected, compared to the gaseous phase. Due to the large thermal conductivity of the liquid and the thin thermal boundary layer inside the droplet, it may be assumed that the heat flux inside the droplet is dominant and the droplet surface temperature can be determined only by the temperature equation inside the droplet with a boundary condition, which considers the latent heat due to evaporation. The effect of the ignored vortex in the gaseous phase due to the assumption of potential flow on the droplet evaporation can be discussed further. This vortex is strong for a spherical shape and weak when the droplet is extended. An expression for this vortex may need to be analysed in further work. The simulations can be performed over a wide range of density and viscosity ratios as well as oscillation frequencies. For example, when replacing the gaseous phase with the same density and viscosity as the liquid, whether this vortex can still be observed. Through enough simulations, the vortex strength and penetration distance of the vortex may be summarized.

Appendices

Appendix A

A.1 Harmonic Solutions of the Laplace Equation in a Spherical Coordinate System

We consider the Laplace equation of a scalar f in a spherical coordinate system (r, θ, φ):

$$\begin{aligned}
&\nabla^2 f = 0 \\
&\nabla^2 f = \frac{1}{r^2}\frac{\partial}{\partial r}\left(r^2\frac{\partial f}{\partial r}\right) + \frac{1}{r^2 sin(\theta)}\frac{\partial}{\partial\theta}\left(sin(\theta)\frac{\partial f}{\partial\theta}\right) + \frac{1}{r^2 sin^2(\theta)}\frac{\partial^2 f}{\partial\varphi^2}
\end{aligned} \tag{A.1}$$

By separation of variables, f has the form:

$$f(r, \theta, \varphi) = R(r)\Theta(\theta)\Phi(\varphi) \tag{A.2}$$

Substituting into Laplace equation and separating variables lead to three ordinary differential equations:

$$\begin{aligned}
&\frac{1}{R}\frac{\partial}{\partial r}\left(r^2\frac{\partial R}{\partial r}\right) = l(l+1), \\
&(1 - cos^2(\theta))\frac{d^2\Theta}{dcos^2(\theta)} - 2cos(\theta)\frac{d\Theta}{dcos(\theta)} + \left(l(l+1) - \frac{m^2}{1 - cos^2(\theta)}\right)\Theta = 0, \\
&\frac{1}{\Phi}\frac{d^2\Phi}{d\varphi^2} = -m^2.
\end{aligned} \tag{A.3}$$

Here l is a non-negative integer and m takes the integer values $|m| \leq l$. The radial equation $R(r)$ yields the following:

$$R(r) = Ar^l + Br^{-(l+1)}. \tag{A.4}$$

The azimuthal equation $\Phi(\varphi)$ admits the general solution:

$$\Phi(\varphi) = C_1 e^{im\varphi} + C_2 e^{-im\varphi}. \tag{A.5}$$

The polar equation $\Theta(\theta)$ is the associated Legendre equation, and one of its solutions is $P_l^m(cos(\theta))$, the associated Legendre functions of the first kind. The associated Legendre functions of the second kind $Q_l^m(cos(\theta))$, as a solution of the equation for $\Theta(\theta)$, are singular at $cos(\theta) = \pm 1$ (refer to Appendix A.2). The regular solution reads:

$$\Theta(\theta) = P_l^m(cos(\theta)) \tag{A.6}$$

Combining the radial, polar and azimuthal equation yields the general solution of f:

$$f(r, \theta, \varphi) = \sum_{l=0}^{\infty}\sum_{m=-l}^{l}\left(A_l^m r^l + B_l^m r^{-(l+1)}\right)P_l^m(cos(\theta))e^{im\varphi} \tag{A.7}$$

The coefficients A_l^m and B_l^m are determined from boundary conditions.

A.2 Legendre's Equation and Associated Legendre's Equation

The solutions of Legendre's equation

$$(1 - z^2)u'' - 2zu' + \nu(\nu + 1)u = 0 \tag{A.8}$$

with real x or complex variable z, are known as Legendre's functions, P_ν Legendre functions of degree ν of the first kind and Q_ν Legendre functions of degree ν of the second kind [111,122,124]. Therefore, the general solution of Legendre's equation is a linear combination of both kinds:

$$u = c_1 P_\nu + c_2 Q_\nu \tag{A.9}$$

In general, P_ν and Q_ν can be given in different forms. In many physical applications, the degree ν takes non-negative integers. Legendre functions of the second kind Q_ν are singular at 1. Legendre functions of the first kind P_ν of non-integer degree ν are also unbounded in the interval $[-1, 1]$, but P_ν of integer degree ν are bounded in this interval. So to obtain a solution, which is bounded in this interval, the degree must be an integer value l. For degree of integer l, $P_l = P_{-l-1}$ is satisfied, so l only takes non-negative integer values [99, 124]. In the following, the solution for the non-negative integer l is discussed. P_l of non-negative integer degree l with suitable standardization ($P_l(1) = 1$) is also called Legendre polynomials.

For a real variable $x \in (-1, 1)$, $P_l(x)$ read:

$$P_l(x) = (-1)^l \frac{1}{2^l l!} \frac{d^l}{dx^l} \left(1 - x^2\right)^l \tag{A.10}$$

as Rodrigues' formula. It can also be given by a hypergeometric series, which is also available for arbitrary degrees [111,122,124]. The first several terms for $P_l(x)$ are:

$$\begin{aligned} P_0(x) &= 1, & P_1(x) &= x, \\ P_2(x) &= \frac{1}{2}(3x^2 - 1), & P_3(x) &= \frac{1}{2}(5x^3 - 3x), \\ P_4(x) &= \frac{1}{8}(35x^4 - 30x^2 + 3), & P_5(x) &= \frac{1}{8}(63x^5 - 70x^3 + 15x) \end{aligned} \tag{A.11}$$

$P_l(x)$ is also valid for $x = \pm 1$ and even for finite x. An important property is $P_l(x) = P_l(-x)$ for even l and $-P_l(x) = P_l(-x)$ for odd l. The Legendre function of the second kind $Q_l(x)$ are given by a recurrence relation:

$$\begin{aligned} &Q_0(x) = \frac{1}{2} ln \left(\frac{1 + x}{1 - x}\right), \quad Q_1(x) = \frac{1}{2} x ln \left(\frac{1 + x}{1 - x}\right) - 1 \\ &Q_2(x) = \frac{(3x^2 - 1)}{4} ln \left(\frac{1 + x}{1 - x}\right) - \frac{3}{2} x \\ &(l + 1)Q_{l+1}(x) = (2l + 1)xQ_l(x) - lQ_{l-1}(x) \end{aligned} \tag{A.12}$$

It can also be written as a hypergeometric series. To note that $Q_l(x)$ is singular at $x = \pm 1$. We have $-Q_0(x) = Q_0(-x)$ and $Q_1(x) = Q_1(-x)$. Therefore, $Q_n(x)$ is even for odd l and odd for even l. The independent variable may be a complex number z. For a complex variable z, we have

$$P_l(z) = \frac{1}{2^l l!}\frac{d^l}{dz^l}\left(z^2 - 1\right)^l \tag{A.13}$$

(or we can replace x with z in Eqn.(A.11)) to obtain Legendre polynomial $P_l(z)$:

$$\begin{aligned} P_0(z) &= 1, & P_1(z) &= z, \\ P_2(z) &= \frac{1}{2}(3z^2 - 1), & P_3(z) &= \frac{1}{2}(5z^3 - 3z), \\ P_4(z) &= \frac{1}{8}(35z^4 - 30z^2 + 3), & P_5(z) &= \frac{1}{8}(63z^5 - 70z^3 + 15z) \end{aligned} \tag{A.14}$$

which holds for arbitrary z in the complex plane with a cut along $(-\infty, -1]$ $(arg(z+1) < \pi)$. $Q_l(z)$ has a slightly different form:

$$\begin{aligned} &Q_0(z) = \frac{1}{2}ln\left(\frac{z+1}{z-1}\right), \quad Q_1(z) = \frac{1}{2}zln\left(\frac{z+1}{z-1}\right) - 1 \\ &Q_2(z) = \frac{(3z^2-1)}{4}ln\left(\frac{z+1}{z-1}\right) - \frac{3}{2}z \\ &(l+1)Q_{l+1}(z) = (2l+1)zQ_l(z) - lQ_{l-1}(z) \end{aligned} \tag{A.15}$$

which holds for z in the complex plane with a cut along $(-\infty, 1]$ $(arg(z-1) < \pi)$. The derivative $Q_2'(z)$ reads:

$$Q_2'(z) = \frac{3z}{2}ln\left(\frac{z+1}{z-1}\right) - \frac{3z^2-1}{2(z^2-1)} - \frac{3}{2} \tag{A.16}$$

The associated Legendre's equation has the form [111, 122, 124]:

$$(1-z^2)u'' - 2zu' + \left[\nu(\nu+1) - \frac{m^2}{1-z^2}\right]u = 0 \tag{A.17}$$

In many applications, ν is non-negative integer l and m is integer $|m| \leq l$. The solutions are the associated Legendre functions of the first kind P_l^m (associated Legendre polynomials) and the associated Legendre functions of the second kind Q_l^m. They can also be given in different forms, one convenient way is:

$$P_l^m(x) = (-1)^{m+l}\frac{\left(1-x^2\right)^{m/2}}{2^n n!}\frac{d^{m+l}}{dx^{m+l}}\left(1-x^2\right)^l = (-1)^m\left(1-x^2\right)^{m/2}\frac{d^m}{dx^m}P_l(x) \tag{A.18}$$

$$Q_l^m(x) = (-1)^m\left(1-x^2\right)^{m/2}\frac{d^m}{dx^m}Q_l(x) \tag{A.19}$$

for a real variable x in $(-1, 1)$. m takes integer values, since in many applications the physical problem is periodic of 2π in the circumferential direction. When $m > l$, the order of the derivative is over the highest order of P_l. At $x = \pm 1$, P_l^m is regular and Q_l^m is singular. For a complex variable z, $P_l^m(z)$ and $Q_l^m(z)$ are given:

$$P_l^m(z) = \frac{\left(z^2-1\right)^{m/2}}{2^n n!} \frac{d^{m+l}}{dz^{m+l}} \left(x^2-1\right)^l = \left(z^2-1\right)^{m/2} \frac{d^m}{dz^m} P_l(z) \tag{A.20}$$

$$Q_l^m(z) = \left(z^2-1\right)^{m/2} \frac{d^m}{dz^m} Q_l(z) \tag{A.21}$$

The associated Legendre functions of the first kind P_l^m are regular in the interval $[-1, 1]$, they are mutually orthogonal in this interval:

$$\int_{-1}^{1} P_l^m(x) P_n^m(x) dx = 0, \quad if\ l \neq n. \tag{A.22}$$

and

$$\int_{-1}^{1} P_l^m(x) P_l^m(x) dx = \frac{2}{2l+1} \frac{(l+m)!}{(l-m)!} \tag{A.23}$$

When $m = 0$, it reduces to the mutual orthogonality of the Legendre functions of the first kind

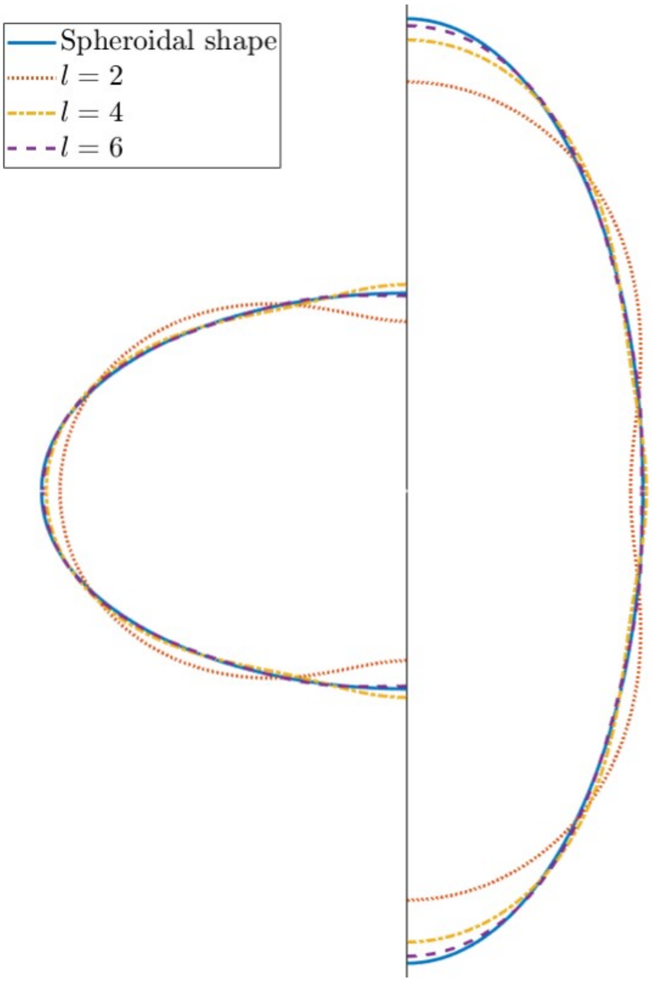

Figure 39: A spheroidal droplet shape of aspect ratio $\varepsilon = 0.54$ (left) and $\varepsilon = 2$ (right), and its approximation truncated in the modes $l = 2$, $l = 4$, and $l = 6$.

$P_l(x)$. If a droplet suffers the infinitesimal displacements, its radius can be expanded by the normal mode technique. The coefficients in each term can be obtained by using this property. Suppose that a rotational symmetric droplet ($m = 0$) of equivalent radius R has the surface $r(\theta) = R + \sum_{l=0}^{\infty} C_l P_l(cos(\theta))$. Applying the mutual orthogonality of $P_l(x)$:

$$\begin{aligned}
&\int_{-1}^{1} \sum_{l=0}^{\infty} \left(C_l P_l(cos(\theta))\right) P_n(cos(\theta)) d(cos(\theta)) \\
&= \int_{-1}^{1} C_n P_n(cos(\theta)) P_n(cos(\theta)) d(cos(\theta)) = C_n \frac{2}{2n+1} \\
&C_n = \frac{2n+1}{2} \int_{-1}^{1} (r(\theta) - R) P_n(cos(\theta)) d(cos(\theta))
\end{aligned} \tag{A.24}$$

The coefficients in each term are derived. A spheroidal droplet shape and its approximation in different modes are shown in Fig. 39. The droplet shape in a higher mode $l = 4, 6$ agrees better with the original spheroidal shape, but with more calculations.

A.3 The Scale Factors of a Generalized Spheroidal Coordinate System

The generalized spheroidal $u^j = (\psi, \eta, \varphi)$ coordinate system is defined by the Cartesian coordinates $x^j = (x, y, z)$:

$$\begin{aligned}
x &= \frac{R}{(1+S)^{1/3}} \frac{\sqrt{1+S\psi^2}}{\psi} \sqrt{1-\eta^2} cos(\varphi) \\
y &= \frac{R}{(1+S)^{1/3}} \frac{\sqrt{1+S\psi^2}}{\psi} \sqrt{1-\eta^2} sin(\varphi) \\
z &= \frac{R}{(1+S)^{1/3}} \frac{1}{\psi} \eta
\end{aligned} \tag{A.25}$$

The scale factor $h_\psi, h_\eta, h_\varphi$ can be calculated from the metric tensor components $g_{jk} = \boldsymbol{g_j} \cdot \boldsymbol{g_k}$ [99,125], in which $\boldsymbol{g_j} = \frac{\partial x^k}{\partial u^j} \boldsymbol{e_k}$ is the covariant vector basis. As the coordinate system is orthogonal, g_{jk} is nil for $j \neq k$. g_{jj} is calculated as $g_{jj} = \sum_{k=1}^{3} \frac{\partial x^k}{\partial u^j} \frac{\partial x^k}{\partial u^j}$ with:

$$\frac{\partial x^k}{\partial u^j} = \begin{bmatrix}
-\frac{R}{(1+S)^{1/3}} \frac{\sqrt{1-\eta^2}}{\psi^2 \sqrt{1+S\psi^2}} cos(\varphi) & -\frac{R}{(1+S)^{1/3}} \frac{\sqrt{1+S\psi^2}\eta}{\psi \sqrt{1-\eta^2}} cos(\varphi) & -\frac{R}{(1+S)^{1/3}} \frac{\sqrt{1+S\psi^2}}{\psi} \sqrt{1-\eta^2} sin(\varphi) \\
-\frac{R}{(1+S)^{1/3}} \frac{\sqrt{1-\eta^2}}{\psi^2 \sqrt{1+S\psi^2}} sin(\varphi) & -\frac{R}{(1+S)^{1/3}} \frac{\sqrt{1+S\psi^2}\eta}{\psi \sqrt{1-\eta^2}} sin(\varphi) & \frac{R}{(1+S)^{1/3}} \frac{\sqrt{1+S\psi^2}}{\psi} \sqrt{1-\eta^2} cos(\varphi) \\
\frac{R}{(1+S)^{1/3}} \frac{1}{\psi^2} \eta & -\frac{R}{(1+S)^{1/3}} \frac{1}{\psi} & 0
\end{bmatrix} \tag{A.26}$$

Then the scale factors are obtained by $h_j = \sqrt{g_{jj}}$:

$$h_\psi = \frac{R}{(1+S)^{1/3}} \frac{\sqrt{1+S\eta^2\psi^2}}{\psi^2 \sqrt{1+S\psi^2}}, h_\eta = \frac{R}{(1+S)^{1/3}} \frac{\sqrt{1+S\eta^2\psi^2}}{\psi \sqrt{1-\eta^2}}, h_\varphi = \frac{R}{(1+S)^{1/3}} \frac{\sqrt{1+S\psi^2}\sqrt{1-\eta^2}}{\psi} \tag{A.27}$$

Then we also have:

$$\begin{aligned}
W^{\psi} &= \frac{h_{\eta} h_{\varphi}}{h_{\psi}} = \frac{R}{(1+S)^{1/3}}(1+S\psi^2),\ W^{\eta} = \frac{h_{\psi} h_{\varphi}}{h_{\eta}} = \frac{R}{(1+S)^{1/3}} \frac{1-\eta^2}{\psi^2} \\
W^{\varphi} &= \frac{h_{\psi} h_{\eta}}{h_{\varphi}} = \frac{R}{(1+S)^{1/3}} \frac{1+S\eta^2\psi^2}{\psi^2(1+S\psi^2)(1-\eta^2)},\ g^{1/2} = h_{\psi} h_{\eta} h_{\varphi} = \frac{R^3}{1+S} \frac{1+S\eta^2\psi^2}{\psi^4}
\end{aligned} \tag{A.28}$$

If we define this generalized coordinate system $u^j = (\phi, \eta, \varphi)$ with $\phi = \frac{1}{\psi}$:

$$\begin{aligned}
x &= \frac{R}{(1+S)^{1/3}} \sqrt{\phi^2+S}\sqrt{1-\eta^2} cos(\varphi) \\
y &= \frac{R}{(1+S)^{1/3}} \sqrt{\phi^2+S}\sqrt{1-\eta^2} sin(\varphi) \\
z &= \frac{R}{(1+S)^{1/3}} \phi\eta
\end{aligned} \tag{A.29}$$

The scale factors can be obtained in the same way. g_{jj} is calculated by $\sum_{k=1}^{3} \frac{\partial x^k}{\partial u^j} \frac{\partial x^k}{\partial u^j}$:

$$\frac{\partial x^k}{\partial u^j} = \begin{bmatrix}
-\frac{R}{(1+S)^{1/3}} \frac{\phi\sqrt{1-\eta^2}}{\sqrt{\phi^2+S}} cos(\varphi) & -\frac{R}{(1+S)^{1/3}} \frac{\sqrt{\phi^2+S}\eta}{\sqrt{1-\eta^2}} cos(\varphi) & -\frac{R}{(1+S)^{1/3}} \sqrt{\phi^2+S}\sqrt{1-\eta^2} sin(\varphi) \\
-\frac{R}{(1+S)^{1/3}} \frac{\phi\sqrt{1-\eta^2}}{\sqrt{\phi^2+S}} sin(\varphi) & -\frac{R}{(1+S)^{1/3}} \frac{\sqrt{\phi^2+S}\eta}{\sqrt{1-\eta^2}} sin(\varphi) & \frac{R}{(1+S)^{1/3}} \sqrt{\phi^2+S}\sqrt{1-\eta^2} cos(\varphi) \\
\frac{R}{(1+S)^{1/3}} \eta & -\frac{R}{(1+S)^{1/3}} \phi & 0
\end{bmatrix} \tag{A.30}$$

So the scale factors $h_j = \sqrt{g_{jj}}$ are derived:

$$h_{\phi} = \frac{R}{(1+S)^{1/3}} \frac{\sqrt{\phi^2+S\eta^2}}{\sqrt{\phi^2+S}}, h_{\eta} = \frac{R}{(1+S)^{1/3}} \frac{\sqrt{\phi^2+S\eta^2}}{\sqrt{1-\eta^2}}, h_{\varphi} = \frac{R}{(1+S)^{1/3}} \sqrt{\phi^2+S}\sqrt{1-\eta^2} \tag{A.31}$$

and we obtain:

$$\begin{aligned}
W^{\phi} &= \frac{h_{\eta} h_{\varphi}}{h_{\phi}} = \frac{R}{(1+S)^{1/3}}(\phi^2+S),\ W^{\eta} = \frac{h_{\phi} h_{\varphi}}{h_{\eta}} = \frac{R}{(1+S)^{1/3}}(1-\eta^2) \\
W^{\varphi} &= \frac{h_{\phi} h_{\eta}}{h_{\varphi}} = \frac{R}{(1+S)^{1/3}} \frac{\phi^2+S\eta^2}{(\phi^2+S)(1-\eta^2)},\ g^{1/2} = h_{\phi} h_{\eta} h_{\varphi} = \frac{R^3}{1+S}(\phi^2+S\eta^2)
\end{aligned} \tag{A.32}$$

A.4 The Surface Area of a Spheroid in a Generalized Spheroidal Coordinate System

In the generalized coordinate system (ϕ, η, φ), the surface element of a spheroid at $\phi = 1$ is $dA = h_\eta h_\varphi d\eta d\varphi$. The surface area of this spheroid $A_{spheroid}$ is evaluated by the integration over the surface:

$$
\begin{aligned}
A_{spheroid} &= \int_{\partial\Omega} dA = \int_{\varphi=0}^{2\pi}\int_{\eta=-1}^{1} h_\eta h_\varphi d\eta d\varphi \\
&\overset{\phi=1}{=} 4\pi \int_{\eta=0}^{1} \frac{R^2}{(1+S)^{2/3}}\sqrt{1+S\eta^2}\sqrt{1+S}d\eta \qquad \text{(A.33)}\\
&= 2\pi\frac{R^2}{(1+S)^{1/6}}\begin{cases}\left(\sqrt{1+S}+\dfrac{arctan\left(\sqrt{\frac{-S}{1+S}}\right)}{\sqrt{-S}}\right), & S<0\\[2ex] \left(\sqrt{1+S}+\dfrac{ln(\sqrt{1+S}+\sqrt{S})}{\sqrt{S}}\right), & S>0\end{cases} \qquad \text{(A.34)}
\end{aligned}
$$

In fact, two expressions for $S < 0$ and $S > 0$ are equivalent. The surface area of an oblate spheroid ($S > 0$) can also be calculated by using the expression for $S < 0$. In reverse, the surface area of a prolate spheroid ($S < 0$) can be obtained by the expression for $S > 0$.

A.5 The Normal Interface Velocity in a Generalized Spheroidal System

From Eqn. 3.59, $\frac{r^2}{a_r^2} + \frac{z^2}{a_z^2} = 1$ is satisfied, with $a_r = \frac{R}{(1+S)^{1/3}}\frac{\sqrt{1+S\psi^2}}{\psi}$ and $a_z = \frac{R}{(1+S)^{1/3}}\frac{1}{\psi}$. Let $f = \frac{r^2}{a_r^2} + \frac{z^2}{a_z^2} - 1$, the unit normal of the interface reads:

$$
n = \frac{\nabla f}{|\nabla f|} = \frac{\left(\frac{2r}{a_r^2}, \frac{2z}{a_z^2}\right)}{\sqrt{\frac{4r^2}{a_r^4}+\frac{4z^2}{a_z^4}}} \overset{\psi=1}{=} \left(\sqrt{\frac{1-\eta^2}{1+S\eta^2}}, \frac{\eta\sqrt{1+S}}{\sqrt{1+S\eta^2}}\right) \qquad \text{(A.35)}
$$

with the positive direction towards the gaseous phase.

The interface velocity V is:

$$
\begin{aligned}
V = (V_r, V_z) &= \left(\left.\frac{dr}{dt}\right|_{\psi=1}, \left.\frac{dz}{dt}\right|_{\psi=1}\right)\\
&= \left(\sqrt{1-\eta^2}\left(\frac{R}{6(1+S)^{5/6}}S_t + (1+S)^{1/6}R_t\right), \eta\left(-\frac{R}{3(1+S)^{4/3}}S_t + \frac{1}{(1+S)^{1/3}}R_t\right)\right) \qquad \text{(A.36)}
\end{aligned}
$$

Then, the normal interface velocity V_n reads:

$$
V_n = V \cdot n = \frac{(1-3\eta^2)R}{6\sqrt{1+S\eta^2}(1+S)^{5/6}}S_t + \frac{(1+S)^{1/6}}{\sqrt{1+S\eta^2}}R_t \qquad \text{(A.37)}
$$

A.6 Gas Velocity for an Oscillating Droplet in Potential Flows

The gas velocity $(u_{G,\psi}, u_{G,\eta})$ can be obtained as the gradient of the velocity potential Φ_G (Eqn.(4.20)). For spherical shapes $S = 0$, the gas velocity $(u_{G,\psi}, u_{G,\eta})$ reads:

$$\begin{aligned} u_{G,\psi} &= -\frac{1}{h_\psi}\frac{\partial \Phi_G}{\partial \psi} = \frac{-RS_t}{3(1+S)^{4/3}}\frac{\sqrt{1+S\psi^2}}{\sqrt{1+S\eta^2\psi^2}}\psi^4 P_2(\eta) \\ u_{G,\eta} &= -\frac{1}{h_\eta}\frac{\partial \Phi_G}{\partial \eta} = \frac{RS_t}{3(1+S)^{4/3}}\frac{\sqrt{1-\eta^2}}{\sqrt{1+S\eta^2\psi^2}}\left(-\frac{\psi^4}{3}\right)P_2^{'}(\eta) \end{aligned} \tag{A.38}$$

For spheroidal shapes $(S \neq 0)$, the gas velocity $(u_{G,\psi}, u_{G,\eta})$ reads:

$$\begin{aligned} u_{G,\psi} &= -\frac{1}{h_\psi}\frac{\partial \Phi_G}{\partial \psi} = \frac{-RS_t}{3(1+S)^{4/3}}\frac{\sqrt{1+S\psi^2}}{\sqrt{1+S\eta^2\psi^2}}\frac{Q_2^{'}(\frac{1}{\psi\sqrt{-S}})}{Q_2^{'}(\frac{1}{\sqrt{-S}})}P_2(\eta) \\ u_{G,\eta} &= -\frac{1}{h_\eta}\frac{\partial \Phi_G}{\partial \eta} = \frac{RS_t}{3(1+S)^{4/3}}\frac{\sqrt{1-\eta^2}}{\sqrt{1+S\eta^2\psi^2}}\frac{Q_2(\frac{1}{\psi\sqrt{-S}})\psi\sqrt{-S}}{Q_2^{'}(\frac{1}{\sqrt{-S}})}P_2^{'}(\eta) \end{aligned} \tag{A.39}$$

with a notation:

$$J(\psi, S) = \begin{cases} \psi^4, & S = 0 \\ \dfrac{Q_2^{'}(\frac{1}{\psi\sqrt{-S}})}{Q_2^{'}(\frac{1}{\sqrt{-S}})}, & S \neq 0 \end{cases} \tag{A.40}$$

$$K(\psi, S) = \begin{cases} -\dfrac{\psi^4}{3}, & S = 0 \\ \dfrac{Q_2(\frac{1}{\psi\sqrt{-S}})}{Q_2^{'}(\frac{1}{\sqrt{-S}})}\psi\sqrt{-S}, & S \neq 0 \end{cases} \tag{A.41}$$

From Appendix A.2, we have $Q_2(\frac{1}{\psi\sqrt{-S}})$, $Q_2^{'}(\frac{1}{\psi\sqrt{-S}})$ and $Q_2^{'}(\frac{1}{\sqrt{-S}})$:

$$Q_2(\frac{1}{\psi\sqrt{-S}}) = \frac{3\left(\frac{1}{\psi\sqrt{-S}}\right)^2 - 1}{4} ln\left(\frac{\frac{1}{\psi\sqrt{-S}} + 1}{\frac{1}{\psi\sqrt{-S}} - 1}\right) - \frac{3}{2}\frac{1}{\psi\sqrt{-S}} \tag{A.42}$$

$$Q_2^{'}(\frac{1}{\psi\sqrt{-S}}) = \frac{3\frac{1}{\psi\sqrt{-S}}}{2} ln\left(\frac{\frac{1}{\psi\sqrt{-S}} + 1}{\frac{1}{\psi\sqrt{-S}} - 1}\right) - \frac{3\left(\frac{1}{\psi\sqrt{-S}}\right)^2 - 1}{2\left(\left(\frac{1}{\psi\sqrt{-S}}\right)^2 - 1\right)} - \frac{3}{2} \tag{A.43}$$

$$Q_2^{'}(\frac{1}{\sqrt{-S}}) = \frac{3\frac{1}{\sqrt{-S}}}{2} ln\left(\frac{\frac{1}{\sqrt{-S}} + 1}{\frac{1}{\sqrt{-S}} - 1}\right) - \frac{3\left(\frac{1}{\sqrt{-S}}\right)^2 - 1}{2\left(\left(\frac{1}{\sqrt{-S}}\right)^2 - 1\right)} - \frac{3}{2} \tag{A.44}$$

According to the relation:

$$ln\left(\frac{\frac{1}{\psi\sqrt{-S}}+1}{\frac{1}{\psi\sqrt{-S}}-1}\right)=ln\left(\frac{1+\psi\sqrt{-S}}{1-\psi\sqrt{-S}}\right)=\begin{cases}2atanh(\psi\sqrt{-S}), & S<0\\ i2arctan(\psi\sqrt{S}), & S>0\end{cases} \tag{A.45}$$

$$ln\left(\frac{\frac{1}{\sqrt{-S}}+1}{\frac{1}{\sqrt{-S}}-1}\right)=ln\left(\frac{1+\sqrt{-S}}{1-\sqrt{-S}}\right)=\begin{cases}2atanh(\sqrt{-S}), & S<0\\ i2arctan(\sqrt{S}), & S>0\end{cases} \tag{A.46}$$

functions $J(\psi,S)$ and $K(\psi,S)$ read:

$$J(\psi,S)=\begin{cases}\psi^4, \quad S=0\\ \\ \dfrac{Q_2'(\frac{1}{\psi\sqrt{-S}})}{Q_2'(\frac{1}{\sqrt{-S}})}=\begin{cases}\dfrac{\frac{3}{\psi\sqrt{-S}}2atanh(\psi\sqrt{-S})-\frac{3+S\psi^2}{1+S\psi^2}-3}{\frac{3}{\sqrt{-S}}2atanh(\sqrt{-S})-\frac{3+S}{1+S}-3}, & S<0\\ \dfrac{\frac{3}{\psi\sqrt{S}}2arctan(\psi\sqrt{S})-\frac{3+S\psi^2}{1+S\psi^2}-3}{\frac{3}{\sqrt{S}}2arctan(\sqrt{S})-\frac{3+S}{1+S}-3}, & S>0\end{cases}\end{cases} \tag{A.47}$$

and

$$K(\psi,S)=\begin{cases}-\dfrac{\psi^4}{3}, \quad S=0\\ \\ \dfrac{Q_2(\frac{1}{\psi\sqrt{-S}})}{Q_2'(\frac{1}{\sqrt{-S}})}\psi\sqrt{-S}=\begin{cases}\dfrac{\left(\frac{3}{2\psi\sqrt{-S}}-\frac{\psi\sqrt{-S}}{2}\right)2atanh(\psi\sqrt{-S})-3}{\frac{3}{\sqrt{-S}}2atanh(\sqrt{-S})-\frac{3+S}{1+S}-3}, & S<0\\ \dfrac{\left(\frac{3}{2\psi\sqrt{S}}+\frac{\psi\sqrt{S}}{2}\right)2arctan(\psi\sqrt{S})-3}{\frac{3}{\sqrt{S}}2arctan(\sqrt{S})-\frac{3+S}{1+S}-3}, & S>0\end{cases}\end{cases} \tag{A.48}$$

A.7 The Coordinate Transformation Matrix

The coordinate transformation matrix between the Cartesian (r,z) and generalized spheroidal (ψ,η) coordinate system can be obtained as the following:

$$\begin{aligned}d\psi &= \psi_r dr + \psi_z dz\\ d\eta &= \eta_r dr + \eta_z dz\\ \\ dr &= r_\psi d\psi + r_\eta d\eta\\ dz &= z_\psi d\psi + z_\eta d\eta\end{aligned} \tag{A.49}$$

With a notation $X=[r,z]^T$ and $Y=[\psi,\eta]^T$, the transformation matrix A and B read (refer to Section 3.6):

$$Y = AdX, \quad A = \begin{bmatrix} \psi_r & \psi_z \\ \eta_r & \eta_z \end{bmatrix} \tag{A.50}$$

$$X = BdY, \quad B = \begin{bmatrix} r_\psi & r_\eta \\ z_\psi & z_\eta \end{bmatrix} = \begin{bmatrix} -\frac{a\sqrt{1-\eta^2}}{\psi^2\sqrt{1+S\psi^2}} & -\frac{a\sqrt{1+S\eta^2}\eta}{\psi\sqrt{1-\eta^2}} \\ -\frac{a\eta}{\psi} & \frac{a}{\psi} \end{bmatrix} \tag{A.51}$$

A is the inverse matrix of B:

$$A = B^{-1} = \frac{\begin{bmatrix} z_\eta & -r_\eta \\ -z_\psi & r_\psi \end{bmatrix}}{det(B)} = \frac{\psi}{a(1+S\psi^2\eta^2)} \begin{bmatrix} -\psi\sqrt{1+S\psi^2}\sqrt{1-\eta^2} & -\psi(1+S\psi^2)\eta \\ -\sqrt{1+S\psi^2}\sqrt{1-\eta^2}\eta & 1-\eta^2 \end{bmatrix} \tag{A.52}$$

A.8 Evaporation Flux and Evaporation Rate under Quasi-steady Assumptions

From the relation $\psi^2 = \frac{1}{\zeta^2|S|}$, the steady vapour distribution $\chi(\psi)$ in the generalized spheroidal coordinate system (ψ, η, φ) by Eqn.(5.11) can be obtained from Eqn.(5.1). The evaporation flux $n_{ev.qs}$ under quasi-steady conditions can also be calculated by Eqn.(5.9) from a steady vapour distribution. The evaporation flux has a positive direction away from the droplet surface into the gaseous phase, which is in the opposite direction of ψ. So the normal gradient of the vapour mass fraction at the surface is $\nabla_n\chi = -\frac{1}{h_\psi}\frac{\partial\chi}{\partial\psi}\Big|_{\psi=1}$, h_ψ is the scale factor.

For a prolate droplet $S < 0$, from Eqn.(5.11) we have:

$$\frac{\frac{1}{\frac{1-\chi}{1-\chi_s}}\frac{-1}{1-\chi_s}d\chi}{ln\left(\frac{1-\chi_\infty}{1-\chi_s}\right)} = -\frac{\frac{1}{1-\frac{-S\psi^2}{\left(1+\sqrt{1+S\psi^2}\right)^2}}\frac{\frac{-S\psi}{\sqrt{-S\psi^2}}(1+\sqrt{1+S\psi^2})-\sqrt{-S\psi^2}\frac{S\psi}{\sqrt{1+S\psi^2}}}{\left(1+\sqrt{1+S\psi^2}\right)^2}d\psi}{atanh\left(\frac{\sqrt{-S}}{1+\sqrt{1+S}}\right)}$$

$$\frac{\partial\chi}{\partial\psi} = \frac{-S\psi}{2\sqrt{-S\psi^2}(1+S\psi^2)}\frac{(1-\chi)ln\left(\frac{1-\chi_\infty}{1-\chi_s}\right)}{atanh\left(\frac{\sqrt{-S}}{1+\sqrt{1+S}}\right)} \tag{A.53}$$

Thus, the evaporation flux $n_{ev.qs}$ under quasi-steady conditions reads:

$$\begin{aligned} n_{ev.qs} &= -\rho_G D\frac{1}{1-\chi}\nabla_n\chi = \rho_G D\frac{1}{1-\chi}\frac{1}{h_\psi}\frac{\partial\chi}{\partial\psi}\Big|_{\psi=1} \\ &= \rho_G D\frac{\psi^2(1+S)^{1/3}}{R}\frac{\sqrt{-S}}{2\sqrt{1+S\eta^2\psi^2}\sqrt{1+S\psi^2}}\frac{ln\left(\frac{1-\chi_\infty}{1-\chi_s}\right)}{atanh\left(\frac{\sqrt{-S}}{1+\sqrt{1+S}}\right)}\Bigg|_{\psi=1} \\ &= \rho_G D\frac{(1+S)^{1/3}}{R}\frac{\sqrt{-S}}{2\sqrt{1+S\eta^2}\sqrt{1+S}}\frac{ln\left(\frac{1-\chi_\infty}{1-\chi_s}\right)}{atanh\left(\frac{\sqrt{-S}}{1+\sqrt{1+S}}\right)} \end{aligned} \tag{A.54}$$

Similarly, for a spherical droplet $S = 0$, we have:

$$\frac{\partial \chi}{\partial \psi} = (1-\chi) ln\left(\frac{1-\chi_\infty}{1-\chi_s}\right)$$
$$n_{ev.qs} = \rho_G D \frac{(1+S)^{1/3}}{R} ln\left(\frac{1-\chi_\infty}{1-\chi_s}\right) \tag{A.55}$$

For an oblate droplet $S > 0$, we obtain:

$$\frac{\partial \chi}{\partial \psi} = \frac{S\psi}{2\sqrt{S\psi^2}(1+S\psi^2)} \frac{(1-\chi) ln\left(\frac{1-\chi_\infty}{1-\chi_s}\right)}{atanh\left(\frac{\sqrt{S}}{1+\sqrt{1+S}}\right)}$$
$$n_{ev.qs} = \rho_G D \frac{(1+S)^{1/3}}{R} \frac{\sqrt{S}}{2\sqrt{1+S\eta^2}\sqrt{1+S}} \frac{ln\left(\frac{1-\chi_\infty}{1-\chi_s}\right)}{atanh\left(\frac{\sqrt{S}}{1+\sqrt{1+S}}\right)} \tag{A.56}$$

The Eqn.(5.12) is derived. The evaporation rate $\dot{M}_{qs}$ under quasi-steady conditions can also be calculated by Eqn.(5.10) from the evaporation flux $n_{ev.qs}$:

$$\dot{M}_{qs} = \int_{\eta=0}^{1} 4\pi \frac{R^2}{(1+S)^{2/3}} \sqrt{1+S\eta^2}\sqrt{1+S} n_{ev.qs} d\eta \tag{A.57}$$

Substituting $n_{ev.qs}$ for varied S, the integrand is independent of η. Eqn.(5.13) is obtained.

A.9 The Apparent Velocity

The apparent velocity V^* is defined as $[h_\psi \psi_t, h_\eta \eta_t]$. Considering the transformation between cylindrical $[r, z, t]$ and the generalized $[\psi, \eta, \tau]$ spheroidal coordinate system ($t = \frac{R_0^2}{D}\tau$), and applying the total derivative, we have:

$$\begin{aligned}
d\psi &= \psi_r dr + \psi_z dz + \psi_t dt \\
d\eta &= \eta_r dr + \eta_z dz + \eta_t dt \\
d\tau &= \tau_r dr + \tau_z dz + \tau_t dt \\
\\
dr &= r_\psi d\psi + r_\eta d\eta + r_\tau d\tau \\
dz &= z_\psi d\psi + z_\eta d\eta + z_\tau d\tau \\
dt &= t_\psi d\psi + t_\eta d\eta + t_\tau d\tau
\end{aligned} \tag{A.58}$$

in a matrix notation:

$$\begin{aligned}
Y &= AdX \\
X &= BdY
\end{aligned} \tag{A.59}$$

with $X = [r, z, t]^T$, $Y = [\psi, \eta, \tau]^T$, and:

$$A = \begin{bmatrix} \psi_r & \psi_z & \psi_t \\ \eta_r & \eta_z & \eta_t \\ 0 & 0 & \tau_t \end{bmatrix} \qquad B = \begin{bmatrix} r_\psi & r_\eta & r_\tau \\ z_\psi & z_\eta & z_\tau \\ 0 & 0 & t_\tau \end{bmatrix}$$

We have $AB = I$, I is the unit matrix. ψ_t and η_t are calculated by:

$$\psi_t = \frac{r_\eta z_\tau - r_\tau z_\eta}{det(B)}, \qquad \eta_t = \frac{-(r_\psi z_\tau - r_\tau z_\psi)}{\det(B)} \tag{A.60}$$

Recalling $t = \frac{R_0^2}{D}\tau$, $r = a\frac{\sqrt{1+S\psi^2}}{\psi}\sqrt{1-\eta^2}$ and $z = a\frac{1}{\psi}\eta$, with $a = \frac{R}{(1+S)^{1/3}}$, ψ_t and η_t are obtained (note that the equivalent radius $R(t)$ and deformation parameter $S(t)$ are time-varying when considering an oscillating and evaporating droplet):

$$\begin{aligned} \psi_t &= \frac{\psi(1+S\psi^2)\left(\frac{R_\tau}{R} - \frac{S_\tau}{3(1+S)} + \frac{\psi^2(1-\eta^2)S_\tau}{2(1+S\psi^2)}\right)}{t_\tau(1+S\eta^2\psi^2)} \\ \eta_t &= \frac{\psi^2\eta(1-\eta^2)\left(\frac{SR_\tau}{R} - \frac{SS_\tau}{3(1+S)} + \frac{S_\tau}{2}\right)}{t_\tau(1+S\eta^2\psi^2)} \end{aligned} \tag{A.61}$$

Then $V^* = [h_\psi \psi_t, h_\eta \eta_t]$ is derived (refer to Appendix A.3):

$$\begin{aligned} V^* &= [V_\psi^*, V_\eta^*] = [h_\psi \psi_t, h_\eta \eta_t] \\ &= \left[\frac{DR\sqrt{1+S\psi^2}}{R_0^2\psi(1+S)^{1/3}\sqrt{1+S\eta^2\psi^2}}\left(\frac{R_\tau}{R} - \frac{S_\tau}{3(1+S)} + \frac{\psi^2(1-\eta^2)S_\tau}{2(1+S\psi^2)}\right),\right. \\ &\quad \left.\frac{DR\psi\eta\sqrt{1-\eta^2}}{R_0^2(1+S)^{1/3}\sqrt{1+S\eta^2\psi^2}}\left(\frac{SR_\tau}{R} - \frac{SS_\tau}{3(1+S)} + \frac{S_\tau}{2}\right)\right] \end{aligned} \tag{A.62}$$

The divergence of the apparent velocity ∇V^* reads:

$$\begin{aligned} \nabla \cdot V^* &= \frac{1}{g^{1/2}}\left(\frac{\partial}{\partial\psi}\left(\frac{g^{1/2}}{h_\psi}V_\psi^*\right) + \frac{\partial}{\partial\eta}\left(\frac{g^{1/2}}{h_\eta}V_\eta^*\right)\right) \\ &= -3\frac{DR_\tau}{R_0^2 R} + \frac{D(1-\eta^2\psi^2)S_\tau}{R_0^2(1+S)(1+S\eta^2\psi^2)} \end{aligned} \tag{A.63}$$

References

[1] A. H. Lefebvre, V. G. McDonell, Atomization and sprays, CRC press, 2017.

[2] N. A. Fuchs, Evaporation and droplet growth in gaseous media., Pergamon Press, London, 1959.

[3] W. A. Sirignano, Fluid dynamics and transport of droplets and sprays, Cambridge University Press, 2010.

[4] R. Holyst, M. Litniewski, D. Jakubczyk, K. Kolwas, M. Kolwas, K. Kowalski, S. Migacz, S. Palesa, M. Zientara, Evaporation of freely suspended single droplets: experimental, theoretical and computational simulations, Reports on progress in physics 76 (3) (2013) 034601.

[5] L. Rayleigh, On the capillary phenomena of jets, Proc. R. Soc. London 29 (1879) 71–97.

[6] H. Lamb, Hydrodynamics, Cambridge University Press, 1924.

[7] C. Miller, L. Scriven, The oscillations of a fluid droplet immersed in another fluid, Journal of Fluid mechanics 32 (3) (1968) 417–435.

[8] L. D. Landau, E. M. Lifshitz, Fluid Mechanics, Vol. 6, Elsevier, 1987.

[9] H. Lamb, On the oscillations of a viscous spheroid, Proceedings of the London Mathematical Society 1 (1) (1881) 51–70.

[10] S. Chandrasekhar, The oscillations of a viscous liquid globe, Proceedings of the London Mathematical Society 3 (1) (1959) 141–149.

[11] S. Chandrasekhar, Hydrodynamic and hydromagnetic stability, Cambridge University Press, 1961.

[12] W. H. Reid, The oscillations of a viscous liquid drop, Quarterly of Applied Mathematics 18 (1) (1960) 86–89.

[13] S. S. Bupara, Spontaneous movements of small round bodies in viscous fluids, Ph.D. thesis, University of Minnesota (1964).

[14] L. E. Scriven, Dynamics of a fluid interface equation of motion for newtonian surface fluids, Chemical Engineering Science 12 (2) (1960) 98–108.

[15] V. G. Levich, C. W. Tobias, Physicochemical hydrodynamics, Journal of The Electrochemical Society 110 (11) (1963) 251C.

[16] A. Prosperetti, Viscous effects on perturbed spherical flows, Quarterly of Applied mathematics 34 (4) (1977) 339–352.

[17] A. Prosperetti, Free oscillations of drops and bubbles: the initial-value problem, Journal of Fluid Mechanics 100 (2) (1980) 333–347.

[18] M. Plesset, On the stability of fluid flows with spherical symmetry, Journal of Applied Physics 25 (1) (1954) 96–98.

[19] M. S. Plesset, T. Mitchell, On the stability of the spherical shape of a vapor cavity in a liquid, Quarterly of Applied Mathematics 13 (4) (1956) 419–430.

[20] G. B. Foote, A numerical method for studying liquid drop behavior: simple oscillation, Journal of Computational Physics 11 (4) (1973) 507–530.

[21] F. H. Harlow, J. E. Welch, et al., Numerical calculation of time-dependent viscous incompressible flow of fluid with free surface, Physics of Fluids 8 (12) (1965) 2182.

[22] C. W. Hirt, Heuristic stability theory for finite-difference equations, Journal of Computational Physics 2 (4) (1968) 339–355.

[23] B. J. Daly, A technique for including surface tension effects in hydrodynamic calculations, Journal of Computational Physics 4 (1) (1969) 97–117.

[24] P. Brazier-Smith, S. Jennings, J. Latham, An investigation of the behaviour of drops and drop-pairs subjected to strong electrical forces, Proceedings of the Royal Society of London. A. Mathematical and Physical Sciences 325 (1562) (1971) 363–376.

[25] P. N. Swarztrauber, A numerical model of the unsteady free boundary of an ideal fluid, Quarterly of Applied Mathematics 31 (2) (1973) 245–251.

[26] D. N. Montgomery, Collisional phenomena of uncharged water drops in a vertical electric field, Ph.D. thesis, The University of Arizona (1968).

[27] E. Trinh, A. Zwern, T. Wang, An experimental study of small-amplitude drop oscillations in immiscible liquid systems, Journal of Fluid Mechanics 115 (1982) 453–474.

[28] P. L. Marston, R. E. Apfel, Acoustically forced shape oscillation of hydrocarbon drops levitated in water, Journal of Colloid and Interface Science 68 (2) (1979) 280–286.

[29] E. Trinh, T. Wang, Large-amplitude free and driven drop-shape oscillations: experimental observations, Journal of Fluid Mechanics 122 (1982) 315–338.

[30] J. A. Tsamopoulos, R. A. Brown, Nonlinear oscillations of inviscid drops and bubbles, Journal of Fluid Mechanics 127 (1983) 519–537.

[31] A. H. Nayfeh, D. T. Mook, Nonlinear oscillations, John Wiley & Sons, 1979.

[32] D. D. Joseph, Domain perturbations: the higher order theory of infinitesimal water waves, Archive for rational mechanics and analysis 51 (4) (1973) 295–303.

[33] T. Patzek, R. Benner Jr, O. Basaran, L. Scriven, Nonlinear oscillations of inviscid free drops, Journal of Computational Physics 97 (2) (1991) 489–515.

[34] T. Lundgren, N. Mansour, Oscillations of drops in zero gravity with weak viscous effects, Journal of Fluid Mechanics 194 (1988) 479–510.

[35] S. Kistler, L. Scriven, Coating flows, in: Computational analysis of polymer processing, Springer, 1983, pp. 243–299.

[36] O. A. Basaran, Nonlinear oscillations of viscous liquid drops, Journal of Fluid Mechanics 241 (1992) 169–198.

[37] T. Wang, A. Anilkumar, C. Lee, Oscillations of liquid drops: results from usml-1 experiments in space, Journal of Fluid Mechanics 308 (1996) 1–14.

[38] D. Zrnić, G. Brenn, Weakly nonlinear shape oscillations of inviscid drops, Journal of Fluid Mechanics 923 (2021) A9.

[39] M.-C. Yuen, Non-linear capillary instability of a liquid jet, Journal of Fluid Mechanics 33 (1) (1968) 151–163.

[40] M. Smuda, F. Kummer, M. Oberlack, D. Zrnić, G. Brenn, From weakly to strongly nonlinear viscous drop shape oscillations: An analytical and numerical study, Physical Review Fluids 9 (6) (2024) 063601.

[41] F. Kummer, Extended discontinuous galerkin methods for two-phase flows: the spatial discretization, International Journal for Numerical Methods in Engineering 109 (2) (2017) 259–289.

[42] S. Tonini, G. Cossali, Analytical model of small-and large-amplitude drop oscillation dynamics, Physics of Fluids 36 (11) (2024).

[43] B. Helenbrook, C. Edwards, Quasi-steady deformation and drag of uncontaminated liquid drops, International journal of multiphase flow 28 (10) (2002) 1631–1657.

[44] E. Loth, Quasi-steady shape and drag of deformable bubbles and drops, International Journal of Multiphase Flow 34 (6) (2008) 523–546.

[45] W. L. Haberman, R. Morton, An experimental investigation of the drag and shape of air bubbles rising in various liquids, Tech. rep. (1953).

[46] M. Tadaki, On the shape and velocity of single air bubbles rising in various liquids, Kagaku Kogaku 25 (1961) 254–264.

[47] H. Tsuge, S.-I. Hibino, The onset conditions of oscillatory motion of single gas bubbles rising in various liquids, Journal of Chemical Engineering of Japan 10 (1) (1977) 66–68.

[48] D. Bhaga, M. Weber, Bubbles in viscous liquids: shapes, wakes and velocities, Journal of Fluid Mechanics 105 (1981) 61–85.

[49] A. Blanco, J. Magnaudet, The structure of the axisymmetric high-Reynolds number flow around an ellipsoidal bubble of fixed shape, Physics of Fluids 7 (6) (1995) 1265–1274.

[50] F. Raymond, J.-M. Rosant, A numerical and experimental study of the terminal velocity and shape of bubbles in viscous liquids, Chemical Engineering Science 55 (5) (2000) 943–955.

[51] F. H. Busse, Oscillations of a rotating liquid drop, Journal of Fluid Mechanics 142 (1984) 1–8.

[52] T. Patzek, O. Basaran, R. Benner, L. Scriven, Nonlinear oscillations of two-dimensional, rotating inviscid drops, Journal of Computational Physics 116 (1) (1995) 3–25.

[53] J. C. Maxwell, Diffusion, Encyclopedia britannica 7 (214) (1878) 625–646.

[54] R. Kronig, J. Brink, On the theory of extraction from falling droplets, Applied Scientific Research 2 (1) (1951) 142–154.

[55] J. Hadamard, C.R. hebd. seances. acad. sci, Paris 152 (1911) 1735–1738.

[56] H. S. Carslaw, J. C. Jaeger, Conduction of heat in solids and heat conduction, Oxford, 1948.

[57] S. Prakash, W. Sirignano, Liquid fuel droplet heating with internal circulation, International Journal of Heat and Mass Transfer 21 (7) (1978) 885–895.

[58] G. K. Batchelor, On steady laminar flow with closed streamlines at large Reynolds number, Journal of Fluid Mechanics 1 (2) (1956) 177–190.

[59] L. M. Milne-Thomson, Theoretical Hydrodynamics, Macmillan, London, 1955.

[60] J. Harper, D. Moore, The motion of a spherical liquid drop at high Reynolds number, Journal of Fluid Mechanics 32 (2) (1968) 367–391.

[61] S. Prakash, W. Sirignano, Theory of convective droplet vaporization with unsteady heat transfer in the circulating liquid phase, International Journal of Heat and Mass Transfer 23 (3) (1980) 253–268.

[62] H. Schlichting, K. Gersten, Boundary Layer Theory McGraw Hill Book Co, McGraw-Hill, New York, 1968.

[63] W. E. Ranz, W. R. Marshall, Evaporation from drops, Chemical Engineering Progress 48 (4) (1952) 173–180.

[64] D. Spalding, Experiments on the burning and extinction of liquid fuel spheres, Fuel 32 (2) (1953) 169–185.

[65] B. Abramzon, W. A. Sirignano, Droplet vaporization model for spray combustion calculations, International journal of heat and mass transfer 32 (9) (1989) 1605–1618.

[66] D. A. Frank-Kamenetskii, Diffusion and heat transfer in chemical kinetics, Plenum Press, 1969.

[67] V. Y. Rivkind, G. Ryskin, Flow structure in motion of a spherical drop in a fluid medium at intermediate Reynolds numbers, Fluid dynamics 11 (1) (1976) 5–12.

[68] D. Oliver, J. Chung, Flow about a fluid sphere at low to moderate Reynolds numbers, Journal of Fluid Mechanics 177 (1987) 1–18.

[69] D. Talley, S. Yao, A semi-empirical approach to thermal and composition transients inside vaporizing fuel droplets, Symposium (International) on Combustion 21 (1) (1988) 609–616.

[70] J. Jin, G. L. Borman, A model for multicomponent droplet vaporization at high ambient pressures, SAE transactions (1985) 483–493.

[71] S. Tonini, G. Cossali, An exact solution of the mass transport equations for spheroidal evaporating drops, International Journal of Heat and Mass Transfer 60 (2013) 236–240.

[72] S. Tonini, G. Cossali, An evaporation model for oscillating spheroidal drops, International Communications in Heat and Mass Transfer 51 (2014) 18–24.

[73] S. Tonini, G. Cossali, One-dimensional analytical approach to modelling evaporation and heating of deformed drops, International Journal of Heat and Mass Transfer 97 (2016) 301–307.

[74] J. Schlottke, B. Weigand, Direct numerical simulation of evaporating droplets, Journal of Computational Physics 227 (10) (2008) 5215–5237.

[75] J. Schwarz, J. Smolik, Mass transfer from a drop—i. experimental study and comparison with existing correlations, International journal of heat and mass transfer 37 (14) (1994) 2139–2143.

[76] M. Kulmala, T. Vesala, J. Schwarz, J. Smolik, Mass transfer from a drop—ii. theoretical analysis of temperature dependent mass flux correlation, International journal of heat and mass transfer 38 (9) (1995) 1705–1708.

[77] B. Al Zaitone, Oblate spheroidal droplet evaporation in an acoustic levitator, International Journal of Heat and Mass Transfer 126 (2018) 164–172.

[78] J. Douglas Jr, J. E. Gunn, A general formulation of alternating direction methods: Part i. parabolic and hyperbolic problems, Numèrische mathèmatik 6 (1) (1964) 428–453.

[79] A. L. Yarin, G. Brenn, O. Kastner, D. Rensink, C. Tropea, Evaporation of acoustically levitated droplets, Journal of Fluid Mechanics 399 (1999) 151–204.

[80] M. Setiya, J. Palmore Jr, Quasi-steady evaporation of deformable liquid fuel droplets, International Journal of Multiphase Flow 164 (2023) 104455.

[81] G. Zheng, R. List, Convective heat transfer of rotating spheres and spheroids with non-uniform surface temperatures, International journal of heat and mass transfer 39 (9) (1996) 1815–1826.

[82] M. Hase, B. Weigand, Transient heat transfer of deforming droplets at high Reynolds numbers, International Journal of Numerical Methods for Heat & Fluid Flow 14 (1) (2004) 85–97.

[83] S. Tonini, G. E. Cossali, Modelling of heat and mass transfer from spheroidal drops with non-uniform surface temperature, International Journal of Heat and Mass Transfer 121 (2018) 747–758.

[84] D. V. Antonov, S. Tonini, G. Cossali, P. A. Strizhak, S. S. Sazhin, Heating and evaporation of a mono-component spheroidal droplet with non-uniform surface temperature, Applied Mathematical Modelling 125 (2024) 687–703.

[85] A. Y. Tong, W. A. Sirignano, Multicomponent transient droplet vaporization with internal circulation: integral equation formulation and approximate solution, Numerical Heat Transfer, Part A: Applications 10 (3) (1986) 253–278.

[86] C. Wagner, On the numerical solution of volterra integral equations, Journal of Mathematics and Physics 32 (1-4) (1953) 289–301.

[87] C. Maqua, G. Castanet, F. Lemoine, Bicomponent droplets evaporation: Temperature measurements and modelling, Fuel 87 (13-14) (2008) 2932–2942.

[88] C. K. Law, H. Law, A d2-law for multicomponent droplet vaporization and combustion, AIAA journal 20 (4) (1982) 522–527.

[89] P. Lage, C. Hackenberg, R. Rangel, Nonideal vaporization of dilating binary droplets with radiation absorption, Combustion and Flame 101 (1-2) (1995) 36–44.

[90] S. Tonini, G. Cossali, An analytical approach to model heating and evaporation of multicomponent ellipsoidal drops, Heat and Mass Transfer 55 (5) (2019) 1257–1269.

[91] J. Tamim, W. L. Hallett, A continuous thermodynamics model for multicomponent droplet vaporization, Chemical Engineering Science 50 (18) (1995) 2933–2942.

[92] G.-S. Zhu, R. D. Reitz, A model for high-pressure vaporization of droplets of complex liquid mixtures using continuous thermodynamics, International Journal of Heat and Mass Transfer 45 (3) (2002) 495–507.

[93] M. Burger, R. Schmehl, K. Prommersberger, O. Schäfer, R. Koch, S. Wittig, Droplet evaporation modeling by the distillation curve model: accounting for kerosene fuel and elevated pressures, International journal of heat and mass transfer 46 (23) (2003) 4403–4412.

[94] O. Reynolds, Papers on Mechanical and Physical Subjects: 1881-1900, Vol. 2, The University Press, 1901.

[95] J. C. Slattery, Advanced transport phenomena, Cambridge University Press, 1999.

[96] L. G. Leal, Advanced transport phenomena: fluid mechanics and convective transport processes, Vol. 7, Cambridge University Press, 2007.

[97] A. Fick, Ueber Diffusion, Annalen der physik 170 (1) (1855) 59–86.

[98] C. Curtiss, Symmetric gaseous diffusion coefficients, Journal of Chemical Physics 49 (7) (1968) 2917–2919.

[99] G. E. Cossali, S. Tonini, Drop Heating and Evaporation: Analytical Solutions in Curvilinear Coordinate Systems, Springer, 2021.

[100] D. T. Greenwood, Principles of dynamics, Vol. 21, Prentice-Hall Englewood Cliffs, NJ, 1988.

[101] C. Truesdell, R. Toupin, The classical field theories, Springer, 1960.

[102] F. Irgens, Continuum mechanics, Springer Science & Business Media, 2008.

[103] F. Mandl, Statistical physics, John Wiley & Sons, 1991.

[104] G. Sidebotham, G. Sidebotham, Heat transfer modes: Conduction, convection, and radiation, Heat transfer modeling: An inductive approach (2015) 61–93.

[105] S. R. De Groot, P. Mazur, Non-equilibrium thermodynamics, Courier Corporation, 2013.

[106] P. Hein, Untersuchungen über den kritischen Zustand, Zeitschrift für Physikalische Chemie 86 (1) (1914) 385–426.

[107] J. W. Gibbs, The Collected Works of J. Willard Gibbs: Thermodynamics, Vol. 1, Longmans, Green and Company, 1928.

[108] A. F. Mills, Mass transfer, Prentice Hall (2001).

[109] J. Schlottke, E. Duelger, B. Weigand, A vof-based 3d numerical investigation of evaporating, deformed droplets, Progress in Computational Fluid Dynamics, An International Journal 9 (6-7) (2009) 426–435.

[110] S. Sazhin, Droplets and sprays, Vol. 345, Springer, 2014.

[111] N. N. Lebedev, Special Functions and Their Applications, Prentice-Hall, 1965.

[112] L. L. V. Helms, et al., Potential theory, Springer, 2009.

[113] P. Moon, D. E. Spencer, Field theory handbook: including coordinate systems, differential equations and their solutions, Springer, 2012.

[114] S. Chandrasekhar, Hydrodynamic and hydromagnetic stability, Courier Corporation, 2013.

[115] M. Rieber, Numerische Modellierung der Dynamik freier Grenzflachen in Zweiphasenstromungen, Ph.D. thesis, University of Stuttgart (2004).

[116] K. Eisenschmidt, M. Ertl, H. Gomaa, C. Kieffer-Roth, C. Meister, P. Rauschenberger, M. Reitzle, K. Schlottke, B. Weigand, Direct numerical simulations for multiphase flows: An overview of the multiphase code fs3d, Applied Mathematics and Computation 272 (2016) 508–517.

[117] C. W. Hirt, B. D. Nichols, Volume of fluid (vof) method for the dynamics of free boundaries, Journal of computational physics 39 (1) (1981) 201–225.

[118] W. J. Rider, D. B. Kothe, Reconstructing volume tracking, Journal of computational physics 141 (2) (1998) 112–152.

[119] M. Rieber, A. Frohn, A numerical study on the mechanism of splashing, International Journal of Heat and Fluid Flow 20 (5) (1999) 455–461.

[120] M. Rieber, F. Graf, M. Hase, N. Roth, B. Weigand, Numerical simulation of moving spherical and strongly deformed droplets, in: Proceedings ILASS-Europe, Vol. 2000, 2000.

[121] J. Reutzsch, C. Kieffer-Roth, B. Weigand, A consistent method for direct numerical simulation of droplet evaporation, Journal of Computational Physics 413 (2020) 109455.

[122] F. W. Olver, NIST handbook of mathematical functions hardback and CD-ROM, Cambridge University Press, 2010.

[123] J. Reutzsch, Direct numerical simulations of phase change processes using a volume-of-fluid method, Ph.D. thesis, University of Stuttgart (2022).

[124] M. Abramowitz, I. A. Stegun, Handbook of mathematical functions: with formulas, graphs, and mathematical tables, Vol. 55, Courier Corporation, 1965.

[125] H. Nguyen-Schäfer, J.-P. Schmidt, Tensor analysis and elementary differential geometry for physicists and engineers, Vol. 21, Springer, 2014.